Structural health monitoring of the additively manufactured structures with embedded fiber optic sensors

Xiao, Y.

DOI
10.4233/uuid:372c1678-f3b2-4e39-8aef-3c05bf954d76

Publication date
2023

Document Version
Final published version

Citation (APA)
Xiao, Y. (2023). *Structural health monitoring of the additively manufactured structures with embedded fiber optic sensors*. [Dissertation (TU Delft), Delft University of Technology].
https://doi.org/10.4233/uuid:372c1678-f3b2-4e39-8aef-3c05bf954d76

Important note
To cite this publication, please use the final published version (if applicable).
Please check the document version above.

STRUCTURAL HEALTH MONITORING OF THE ADDITIVELY MANUFACTURED STRUCTURES WITH EMBEDDED FIBER OPTIC SENSORS

STRUCTURAL HEALTH MONITORING OF THE ADDITIVELY MANUFACTURED STRUCTURES WITH EMBEDDED FIBER OPTIC SENSORS

Dissertation

For the purpose of obtaining the degree of doctor

at Delft University of Technology,

by the authority of the Rector Magnificus Prof.dr.ir. T.H.J.J. van der Hagen,

Chair of the Board for Doctorates,

to be defended publicly on Monday 11, December 2023 at 12:30 o'clock

by

Yuzhe XIAO

Master of Science in Mechanical Engineering,
Beihang University, China,
Born in Henan, China

This dissertation has been approved by the promotors

Composition of the doctoral committee:

Rector Magnificus,	Chairperson
Prof. dr. ir. R. Benedictus	Delft University of Technology, promotor
Dr. C.D. Rans	Delft University of Technology, copromotor
Independent members:	
Prof. dr. ir. C.J. Simào Ferreira	Delft University of Technology
Dr. M. Martinez	Clarkson University, United States
Prof. Dr. -Ing M. Rutner	Hamburg University of Technology, Germany
Dr. ir. B.F. Lopes dos Santos	Delft University of Technology
Prof. dr. ir. L.L.M. Veldhuis	Delft University of Technology, Reserve member

Keywords: Structural health monitoring, fiber optic sensor, additive manufacturing, crack detection, machine learning

Printed by: Ipskamp Printing

Front & Back: Beautiful cover art that captures the entire content of this thesis in a single illustration.

ISBN 978-94-6384-500-7

An electronic version of this dissertation is available at
http://repository.tudelft.nl/.

CONTENTS

SUMMARY

Additively manufacturing can bring opportunities and risk factors to the aerospace industry. On one hand, additive manufacturing allows the manufacturing of structures with geometries that are difficult or impossible to fabricate with conventional machining procedures. This geometry flexibility may lead to components with a greater strength-to-weight ratio, which can enhance the aircraft's fuel efficiency. On the other hand, possible defects in the additively manufactured parts can lead to reduced strength and increased fatigue susceptibility. In addition, it is very difficult to apply traditional non-destructive testing techniques to additively manufactured specimens with complex geometry due to limited accessibility.

Structural health monitoring can be a good alternative or addition to the traditional non-destructive testing for additively manufactured structures due to its ability to continue continuously and detect hidden defects. This thesis investigates the feasibility of embedding fiber optic sensors via pre-defined capillaries in the additively manufactured structure and proposes novel approaches to perform crack detection based on the strain data measured with the embedded fiber.

Fiber embedding within the additively manufactured parts in previous research mainly involves creating a U-shape groove in the additively manufactured substrate, pausing the additive manufacturing process and inserting the fiber into the groove, and resuming the process for encapsulation. There is also another research on creating a vacuum sensor in additively manufactured structures with a capillary. However, there are clear limitations to the previous research. This study combines the methodology of the two preceding research and proposed a novel approach to embedding fiber sensors via a pre-defined capillary in the selective laser melted (SLM) structure. The main research question is how to use the fiber embedded via a pre-defined capillary to perform crack detection in SLM structures. The aim of this research is to develop a more effective strategy for crack detection in additively manufactured parts and help improve their reliability in the aerospace industry.

There are some sub-research questions. The first research question is how the possible fiber positions and orientations variations influence strain measurement accuracy. Both analytical and numerical models are utilized to predict strain distributions along embedded fibers at different positions and with different orientations within the specimen. Four-point bending static test is performed to verify the model. It is found that variation of fiber orientations has negligible influence on strain measurement accuracy compared with fiber position variations.

The second research question is how effective the strain exceedance method is for detecting cracks in the SLM specimens. The analytical model is used to establish a strain

window. Four-point bending fatigue tests were performed with embedded fiber optic sensors measuring in situ strain. The measured strain was compared with the strain window to determine if there was any crack in the specimen and the length of the crack when it was first detected can be observed with the camera. Strain exceedance can be observed which indicates the existence of the crack in the SLM specimen.

Using the strain exceedance method, the strain distribution pattern has already changed before the crack is detected with the strain exceedance method. The last research question is how to use machine learning to detect small cracks based on the strain distribution pattern and detect cracks that can not be detected with the simple strain exceedance method. In order to answer the question, a carefully-designed deep neural network (DNN) model is established and trained with the data acquired from fatigue tests and simulation. The results of the DNN model show that the model can detect cracks before the strain exceedance method can detect any crack. In addition, it is shown that the crack detection method based on machine learning and fiber embedding via capillary can detect cracks much earlier than the vacuum sensor based method proposed in Strantza's study previously.

SAMENVATTING

Additief produceren kan kansen en risico's met zich meebrengen voor de lucht- en ruimtevaartindustrie. Aan de ene kant maakt additief produceren het mogelijk om structuren te maken met geometrieën die moeilijk of onmogelijk te maken zijn met conventionele bewerkingsprocedures. Deze geometrische flexibiliteit kan leiden tot componenten met een grotere sterkte-gewichtsverhouding, wat de brandstofefficiëntie van het vliegtuig kan verbeteren. Aan de andere kant kunnen mogelijke defecten in de additief vervaardigde onderdelen leiden tot verminderde sterkte en verhoogde gevoeligheid voor vermoeiing. Bovendien is het erg moeilijk om traditionele niet-destructieve testtechnieken toe te passen op op additief vervaardigde proefstukken met een complexe geometrie vanwege de beperkte toegankelijkheid.

Structurele gezondheidsmonitoring kan een goed alternatief of aanvulling zijn op het traditionele niet-destructieve onderzoek voor additief vervaardigde constructies vanwege de mogelijkheid om continu door te gaan en verborgen defecten te detecteren. Dit proefschrift onderzoekt de haalbaarheid van het inbedden van glasvezelsensoren via vooraf gedefinieerde haarvaten in de additief vervaardigde constructie en stelt nieuwe benaderingen voor om scheurdetectie uit te voeren op basis van de rekgegevens gemeten met de ingebedde vezel.

Het inbedden van vezels in de additief vervaardigde onderdelen in eerder onderzoek omvat voornamelijk het maken van een U-vormige groef in het additief vervaardigde substraat, het pauzeren van het additief vervaardigingsproces en het inbrengen van de vezel in de groef, en het hervatten van het proces voor inkapseling. Er is ook onderzoek gedaan naar het creëren van een vacuümsensor in additief vervaardigde structuren met een capillair. Er zijn echter duidelijke beperkingen aan het eerdere onderzoek. Dit onderzoek combineert de methodologie van de twee voorgaande onderzoeken en stelt een nieuwe aanpak voor om vezelsensoren in te kapselen via een vooraf gedefinieerd capillair in de selectieve lasersmeltstructuur (SLM). De belangrijkste onderzoeksvraag is hoe de vezel ingebed via een vooraf gedefinieerd capillair kan worden gebruikt om scheurdetectie uit te voeren in SLM-structuren. Het doel van dit onderzoek is het ontwikkelen van een effectievere strategie voor scheurdetectie in additief vervaardigde onderdelen en het verbeteren van hun betrouwbaarheid in de lucht- en ruimtevaartindustrie.

Er zijn een aantal subonderzoeksvragen. De eerste onderzoeksvraag is hoe de mogelijke vezelposities en -oriëntaties de nauwkeurigheid van de rekmeting beïnvloeden. Zowel analytische als numerieke modellen worden gebruikt om de rekverdeling te voorspellen langs ingebedde vezels op verschillende posities en met verschillende oriëntaties binnen het proefstuk. Statische vierpuntsbuigproef wordt uitgevoerd om het model te verifiëren. Het blijkt dat variatie van vezeloriëntaties een verwaarloosbare invloed heeft op de rekmeting in vergelijking met vezelpositievariaties.

De tweede onderzoeksvraag is hoe effectief de rekgrensoverschrijdingsmethode is voor het detecteren van scheuren in de SLM proefstukken. Het analytische model wordt gebruikt om een rekvenster vast te stellen. Er werd een vierpunts buigvermoeiingstest uitgevoerd met ingebedde glasvezelsensoren die in situ rek meten. De gemeten spanning werd vergeleken met het rekvenster om te bepalen of er een scheur in het proefstuk zat en wat de lengte van de scheur was toen deze voor het eerst werd gedetecteerd. Er werden overschrijdingen van de rek waargenomen die duiden op het bestaan van een scheur in het SLM proefstuk.

Bij gebruik van de rekgrensoverschrijdingsmethode is het rekverdelingspatroon al veranderd voordat de scheur gedetecteerd wordt met de rekgrensoverschrijdingsmethode. De laatste onderzoeksvraag is hoe machine learning gebruikt kan worden om kleine scheuren te detecteren op basis van het rekverdelingspatroon en scheuren te detecteren die niet gedetecteerd kunnen worden met de eenvoudige rekoverspanningsmethode. Om deze vraag te beantwoorden wordt een zorgvuldig ontworpen diep neuraal netwerk (DNN) model opgesteld en getraind met de gegevens verkregen uit vermoeiingstesten en simulatie. De resultaten van het DNN-model tonen aan dat het model scheuren kan detecteren voordat de rekoverschrijdingsmethode een scheur kan detecteren. Daarnaast wordt aangetoond dat de scheurdetectiemethode gebaseerd op machine learning en vezelinbedding via capillair scheuren veel eerder kan detecteren dan de vacuümsensorgebaseerde methode die eerder werd voorgesteld in het onderzoek van Strantza.

1

INTRODUCTION

1

1.1. BACKGROUND AND MOTIVATION

DEVELOPMENT of the aviation sector is posing challenges to the environment of our society. The issue of Greenhouse gas emissions is one of the key impacts from the aviation sector. The International Civil Aviation Organization (ICAO) estimates that around 915 million tons of carbon dioxide (CO2) were released into the atmosphere in the aviation industry worldwide in 2019, and that made for about 2% of all CO2 emissions worldwide [1].

However, there is an increasingly growing demand for the aviation industry, the passenger traffic was predicted to increase with an average rate of 4.55% annually in the future [2], due to factors including rising tourism, better economic prospects, and increased globalization. The demand is increasing especially fast in some of the fast-growing emerging markets. For example, air travel has expanded due to rising economic affluence in nations like China, India, Brazil etc. The aviation sector in emerging markets is anticipated to continue expanding quickly due to the increase of low-cost carriers and the infrastructure for air travel. Because of the steadily increasing demand for aviation demand worldwide, it is worth noting that greenhouse emissions especially CO2 emissions are a concern because they can cause global warming and climate change.

The aviation industry is making an active effort to lessen its effect on the environment and address how it contributes to climate change. The measures that the industry is taking to mitigate its negative impact on climate change include improving fuel efficiency, participating in carbon offsetting programs, adopting alternative technologies, etc [3]. Among them, increasing fuel efficiency is regarded as one of the most effective ways to lessen the aviation sector's environmental impact. The fuel efficiency is monitored by the International Air Transport Association (IATA), which gives information on how this has changed over time. For instance, the average fuel economy of international flights rose by 1.8% in 2020 compared to 2019 according to IATA [4].

Weight reduction of aircraft is one of the most effective ways of improving aircraft fuel efficiency. It is estimated that the aircraft fuel consumption can drop by 0.25% to 0.75% when its weight can be reduced by 1% [5]. There are several techniques that are more and more adopted to reduce aircraft weight, which include using lightweight structures, design optimization, streamlining, systems integration, etc [6]. Among all the different methods to reduce aircraft weight, additively manufactured lightweight structures are increasingly used in the construction of aircraft. The engine bearings in the Rolls-Royce Trent-XWB powering Airbus A350 XWB are made with the electron beam melting technologies [7].

Additive manufacturing, also known as 3D printing, is a process of building 3D solid objects from a digital model layer by layer. Instead of removing material from a block to make a finished product as is the case with traditional subtractive manufacturing techniques like machining or molding, additive manufacturing builds the object up layer by layer. This makes it feasible to create detailed, complex patterns and geometries that would be very difficult or impossible to make using traditional manufacturing process. Different types of additive manufacturing processes include Fused Deposition Modeling (FDM), Stereolithography (SLA), Electron Beam Melting (EBM), SLM, and Laminated

Object Manufacturing (LOM) [8].

Additive manufacturing has the potential to transform the manufacturing industry by facilitating the production of parts with more design flexibility, reduced lead times, less waste, and enhanced product performance. The aerospace engineering industry has extensively investigated the use of additive manufacturing for several decades, with a primary emphasis on the creation of lightweight components that exhibit exceptional performance characteristics. The present lightweight components have been strategically designed to enhance both strength and stiffness, so effectively minimizing the overall weight of the aircraft while maintaining optimal performance levels.

By enabling the creation of parts with higher design freedom, shorter lead times, less waste, and better product performance, additive manufacturing has the potential to revolutionize the manufacturing sector. In aerospace engineering, additive manufacturing has been explored for several decades, and its main focus is on manufacturing lightweight, high-performance parts. These lightweight parts are optimized for strength and stiffness, reducing the weight of the aircraft without sacrificing performance [7].

Despite all the advantages of using additive manufacturing to manufacture lightweight structures in aircraft, there are also limitations in the use of additive manufacturing. One of the most significant limitations is the repair and maintenance of these additively manufactured structures. Compared to conventional parts, repair, and maintenance of additively manufactured parts can be more challenging. The first reason is the complex design. Parts made by additive manufacturing sometimes have complicated and complex geometries, which can make it hard to access the internal structure manually. Therefore it can be more challenging to repair or change with traditional methods. Traditional parts frequently have easier-to-work-with, simpler shapes, and patterns [9]. The second reason is the surface finish of the additively manufactured specimens. The rough surface finishes of as-built additively manufactured parts can make them harder to repair compared with traditional parts [10]. Finally, the repairability of parts made by additive manufacturing may be impacted by the differences in their characteristics from standard parts. The variability of the material properties occurs in the additively manufactured parts, which include microstructure, residual stress, and composition variability. Because of this variability, it may be more challenging to forecast how the part will behave during maintenance and repair. All these limitations make it hard to perform inspection and evaluation of the additively manufactured parts with traditional nondestructive testing (NDT) [11].

Structural health monitoring can complement traditional Non-Destructive Testing (NDT) methods, and has the potential to overcome the limitation of NDT on additively manufactured parts. The term "Structural health monitoring" which is often abbreviated as "SHM", describes the process of using sensors and other measuring tools to continuously evaluate the structural health and operation of some parts of an airplane, building, or bridge, etc [12]. The primary aim of structural health monitoring is to identify potential anomalies or early warning signals of damage before the occurrence of catastrophic failure, hence augmenting the safety and reliability of these critical components.

In the aerospace industry, structural health monitoring is often achieved by the integra-

tion of various sensors, including strain gauges, accelerometers, and optical fiber sensors, within the aircraft's structure [13]. The sensors continually collect several types of data, such as strain, stress, temperature, vibration, and others. These data are consistently analyzed and processed to detect any signs of degradation or damage inside the structure. structural health monitoring offers many advantages, including enhanced operational efficiency, reduced maintenance cost, and heightened safety measures. With aircraft equipped with the structural health monitoring system, airlines have the ability to detect early damages and take preventative action to solve the problem, such as replacing or repairing parts before they break down [14]. That can lower the likelihood of any catastrophe. This thesis investigates the possibility of applying structural health monitoring on additively manufactured parts in order to utilize the ability of additive manufacturing to create lightweight structures as well as guarantee their structural integrity.

The possibility to perform structural health monitoring on the additively manufactured parts is investigated in a previous study [15], where a vacuum sensor is manufactured by integrating a capillary within a part using Selective Laser Melting (SLM). As this sensor type relies on cracks growing up to the embedded capillary in order to disrupt its vacuum condition, the capillary needs to be placed in close proximity to fatigue hot spots in order to be effective. This thesis builds on the concept of capillary, combines it with fiber optic sensor used for structural health monitoring, and propose to embed fiber optic sensors within pre-manufactured capillary for crack detection in the additively manufactured parts. The act of embedding a sensor is highly compatible with the layer-by-layer manufacturing approach of AM, making embedded structural health monitoring a potentially good fit with AM processes for damage detection. Compare to directly bonding the fiber optic sensors on the specimen surface, embedding fiber optic sensors has some advantages. The embedded fiber has improved durability compared with the surface-bonded fiber. They are better protected and less susceptible to harm when they are integrated into the structure [16]. In contrast to sensors that are merely glued to the surface, embedding fibers can boost their toughness and dependability.

In summary, this thesis aims to investigate the feasibility of embedding fiber optic sensors via pre-defined capillaries in the additively manufactured structure and proposes novel approaches to perform crack detection based on the strain data measured with the embedded fiber. By analyzing the new opportunities and challenges brought by different crack detection approaches using embedded fibers, this study seeks to develop more effective strategies for crack detection in additively manufactured parts and improve their reliability and safety in the aerospace industry.

BIBLIOGRAPHY

[1] N. Marszałek and T. Lis, "The future of sustainable aviation fuels", *Combustion Engines*, vol. 61, 2022.

[2] A-ICE, *Passenger traffic growth: How airports can meet rising demand*, 2018. [Online]. Available: https://www.airport-operations.com/news/8/passenger-traffic-growth-how-airports-can-meet-rising-demand.

[3] M. A. Hasan, A. A. Mamun, S. M. Rahman, *et al.*, "Climate change mitigation pathways for the aviation sector", *Sustainability*, vol. 13, no. 7, p. 3656, 2021.

[4] M. Janić, "An assessment of the potential of alternative fuels for "greening" commercial air transportation", *Journal of Air Transport Management*, vol. 69, pp. 235–247, 2018.

[5] D. L. Greene, "Commercial air transport energy use and emissions: Is technology enough?.", 1995.

[6] K. Kearney, *4 ways changes in aircraft design and components reduce fuel consumption*, 2020. [Online]. Available: https://aerospace.honeywell.com/us/en/about-us/blogs/4-ways-changes-in-aircraft-design-and-components-reduce-fuel-con.

[7] L. J. Kumar and C. Krishnadas Nair, "Current trends of additive manufacturing in the aerospace industry", *Advances in 3D printing & additive manufacturing technologies*, pp. 39–54, 2017.

[8] J. Gardan, "Additive manufacturing technologies: State of the art and trends", *Additive Manufacturing Handbook*, pp. 149–168, 2017.

[9] X. Zhang and E. Liang, "Metal additive manufacturing in aircraft: Current application, opportunities and challenges", in *IOP Conference Series: Materials Science and Engineering*, IOP Publishing, vol. 493, 2019, p. 012 032.

[10] A. Du Plessis, E. MacDonald, J. M. Waller, and F. Berto, "Non-destructive testing of parts produced by laser powder bed fusion", in *Fundamentals of Laser Powder Bed Fusion of Metals*, Elsevier, 2021, pp. 277–300.

[11] B. Blakey-Milner, P. Gradl, G. Snedden, *et al.*, "Metal additive manufacturing in aerospace: A review", *Materials & Design*, vol. 209, p. 110 008, 2021.

[12] C. R. Farrar and K. Worden, "An introduction to structural health monitoring", *Philosophical Transactions of the Royal Society A: Mathematical, Physical and Engineering Sciences*, vol. 365, no. 1851, pp. 303–315, 2007.

[13] K. Diamanti and C. Soutis, "Structural health monitoring techniques for aircraft composite structures", *Progress in Aerospace Sciences*, vol. 46, no. 8, pp. 342–352, 2010.

[14] T. Dong and N. H. Kim, "Cost-effectiveness of structural health monitoring in fuselage maintenance of the civil aviation industry", *Aerospace*, vol. 5, no. 3, p. 87, 2018.

[15] M. Strantza, "Additive manufacturing as a tool for structural health monitoring of metallic structures", Ph.D. dissertation, Vrije Universiteit Brussel Brussels, Belgium, 2016.

[16] K. Kesavan, K. Ravisankar, S. Parivallal, P. Sreeshylam, and S. Sridhar, "Experimental studies on fiber optic sensors embedded in concrete", *Measurement*, vol. 43, no. 2, pp. 157–163, 2010.

2

LITERATURE REVIEW

2.1. INTRODUCTION

This literature review aims to provide a comprehensive overview of the research on performing structural health monitoring on selectively laser melted (SLM) aluminum alloy parts. I will mainly focus on the research on the opportunities and risk factors brought by SLM and investigate the various structural health monitoring approaches and data processing techniques applied to the SLM structures. Research of the SLM processes and the influence of various SLM parameters on the quality of the parts are not the focus of the review. In addition, the review of different structural health monitoring approaches will only focus on the first two stages of structural health monitoring, damage detection, and localization. Synthesizing and critically assessing the existing literature, the aim of this review is to identify gaps in the research and provide directions for this thesis.

2.2. INTRODUCTION TO THE APPLICATION OF ADDITIVE MANUFACTURING IN AEROSPACE ENGINEERING

2.2.1. DEVELOPMENT OF ADDITIVE MANUFACTURING

Additive manufacturing, also called 3D printing, is a technology that allows for the creation of three-dimensional objects by stacking layers of material on top of one another. At the beginning of the 1980s, Dr. Hideo Kodama developed the prototyping machine using the information from 3D scanning and the layering structure from 3D topographical maps. Later in the year of 1984, Chuck Hull invented a process called stereolithography, which used a laser to cure a liquid photopolymer into a solid object layer by layer, and that is called SLA technology [1]. Carl Deckard and Joseph Beaman developed the selective Laser sintering (SLS) process at the University of Texas at Austin in the mid-1980s, and the process uses a laser to selectively fuse powdered materials, such as plastics or metals, layer by layer to create a solid object, and the technology was initially used for rapid prototyping [2]. After that, other additive manufacturing technologies and methods were also developed. S. Scott Crump developed the fused deposition modeling (FDM) process in the end of 1980s, with the process of melting a thermoplastic filament and extruding it layer by layer to create a 3D object [3]. Building on the foundation laid by SLS technology, the selective laser melting technology (SLM) was developed in the late 1990s [4]. Both SLM and SLS selectively fuse powdered materials layer by layer to produce 3D objects. However, they vary in how much the powdered substance is melted. While SLS technology only partly melts the material, producing a more porous part, SLM technology completely melts the material, producing a denser, stronger part. Because the material is fully melted for SLM, it is also possible to use SLM with a wider range of materials than SLS [5]. The Powder Bed Fusion (PBF) technology was similar to the SLM technology in the aspect that it also fused powdered materials layer by layer. However, they are also different. PBF can use different heat sources such as laser and electron beam, and PBG also sinter or partially melt powdered materials [6]. Due to the advantages of SLM mentioned above, it will be selected for manufacturing the specimens in this study.

2.2.2. APPLICATION OF ADDITIVE MANUFACTURING IN THE AEROSPACE INDUSTRY

Additive manufacturing has been increasingly used in the field of aerospace engineering. GE Aviation uses direct metal laser melting to manufacture intricate gas nozzles for its LEAP engine with the nickel-based alloy 718 [7]. The material is chosen because it is resistant to high temperatures, corrosion, and oxidation. These properties make the material ideal to be used in the harsh environment of the aero-engine [8]. Ti6Al4V has been widely used in the creation of aircraft engine and aircraft frame components due to its good balance of strength, fracture toughness, and corrosion resistance [9]. AlSi10Mg is the most commonly used aluminum alloy in aerospace structures which include aircraft engine parts such as engine blocks, pistons, and cylinder heads due to its property of high strength-to-weight ratio, excellent thermal conductivity, and being corrosion-resistance [10]. Both titanium and aluminum alloys are commonly used because they have good mechanical properties. However, they all have their advantages and disadvantages. Compared with aluminum alloys, titanium alloys have higher strength and fatigue properties, however, they are more expensive and more difficult to process since they generally have a higher melting point and lower thermal conductivity [11]. Aluminum alloys on the other hand have lower strength-to-weight ratios compared with titanium alloys, however, they are more cost-effective and easier to process because they have better thermal conductivity and weldability [12]. In this study, the AlSi10Mg is selected for the specimen in this study for its excellent combination of properties.

2.3. THE ADVANTAGES AND RISK FACTORS BROUGHT BY ADDITIVE MANUFACTURING TO THE AEROSPACE INDUSTRY

2.3.1. ADVANTAGE OF APPLYING ADDITIVE MANUFACTURING IN THE AEROSPACE INDUSTRY

Additive manufacturing has been increasingly used in aerospace engineering. One of the biggest advantages of additive manufacturing over conventional machining techniques is design flexibility. With additive manufacturing, designers can create complicated geometries that are difficult or impossible to fabricate with conventional machining procedures [13]. This design flexibility may lead to components with a greater strength-to-weight ratio, which will enhance the aircraft's fuel efficiency [14]. The MTU Aero Engines used additive manufacturing for a variety of aero-engine components as shown in figure 2.1 to help Airbus achieve its 15% fuel consumption reduction for the A320neo [15]. In addition, additive manufacturing technology had been utilized to manufacture various components including brackets and hinges, seat buckles as well as flight deck monitor arms [16] [17]. The Concept Laser company designed and manufactured cabin brackets with additive manufacturing for Airbus A350 jets as shown in figure 2.2. The bionic design is inspired by nature and can significantly reduce the bracket' mass [18].

2.3.2. LIMITATION OF ADDITIVELY MANUFACTURED METAL PARTS

There are some limitations of additively manufactured parts compared to traditional parts, which include porosity, residual stress, anisotropy, and poor surface finishing [21].

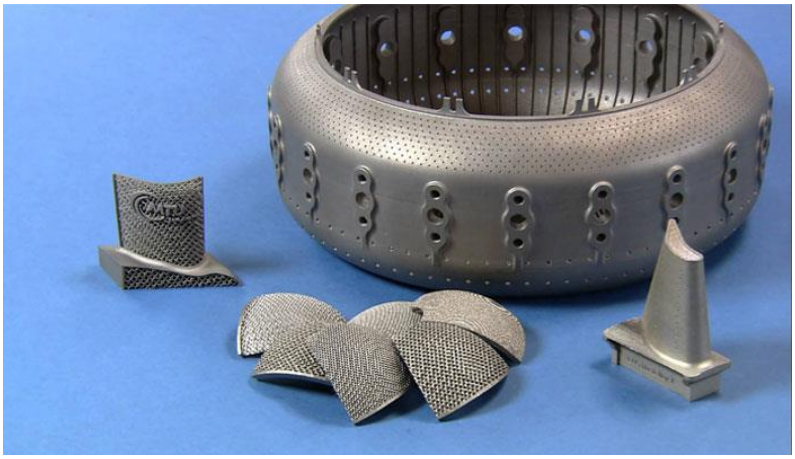

Figure 2.1: Additively manufactured parts made by MTU Aero Engines company [19]

Figure 2.2: Traditional aircraft brackets versus a novel aircraft bracket with topology optimized design [20]

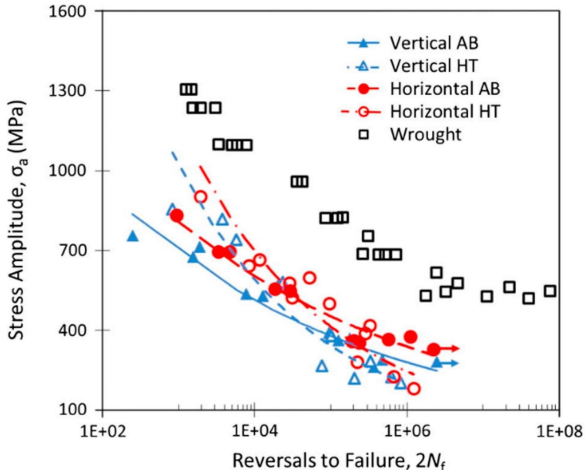

Figure 2.3: Comparison of fatigue performance of SLM steel 630 regardless of the building direction with respect to the wrought counterparts

Porosity refers to the existence of cavities or pores in a material, which can be introduced in additively manufactured parts by the presence of trapped gas or incomplete fusion of the metal particle. Porosity can lead to reduced strength, increased fatigue susceptibility, and reduced resistance to corrosion or other environmental factors. The increasing existence of porosity can negatively impact the yield strength and ultimate strength [22].

Due to thermal gradients and non-uniform cooling during the printing process, residual stress is an additional issue that may occur in additively manufactured parts [23]. Residual stress can lead to distortion, fracture, and even premature failure of service parts in an operating environment [24]. Techniques such as heat treatment, shot peening and mechanical working can be used to relieve the residual stresses in additively manufactured parts [25].

Defects in additively manufactured parts may have a harmful impact on their fatigue lives. Figure 2.3 shows the comparison of fatigue performance of SLM steel 630 regardless of the building direction with respect to the wrought counterparts. It can be seen that the fatigue performance of SLM steel 630 regardless of the building direction is worse than their wrought counterparts.

There are challenges to applying traditional non-destructive testing (NDT) techniques to the SLM specimens. One of the biggest challenges is limited accessibility. Internal structures, voids, or other concealed features can often be found in SLM specimens of complex geometries, and one example can be seen in figure 2.4. It may be very difficult to access these features with inspection probes.

Figure 2.4: Spider bracket to support architectural glass facade [26]

2.4. INTRODUCTION TO STRUCTURAL HEALTH MONITORING

2.4.1. THE CONCEPT OF STRUCTURAL HEALTH MONITORING

SHM is a process of integrating sensors and actuators within a structure to gather data continuously and monitor the health of the structure [27]. The goal of structural health monitoring is to continuously monitor structural integrity to ensure safety. Due to its ability to monitor continuously and detect hidden defects, structural health monitoring can be a good alternative or addition to the traditional non-destructive testing for additively manufactured structures. Figure 2.5 depicts a schematic structure of the structural health monitoring systems. As can be seen in the figure, a structural health monitoring system can be used to monitor the health state of the structure and its usage. Monitoring of its health state is performed on 4 levels hierarchically [28]. It should be noticed that the third and fourth level of structural health monitoring is still topic of ongoing discussion both in the industry and academia, which are therefore not determined yet. However, most of the study in this thesis only involves the first level of damage detection in additively manufactured structures. Therefore, only one selected definition of the four-level structural health monitoring is given here. According to Balageas etc. [27], the first level is damage detection which is to determine the existence of damage, the second level is damage localization to locate the damages in the structure, the third level is damage assessment for estimating the extent of the damage, and the fourth level is remaining life prediction for predicting the remaining life of the structure. Damage refers to the changes or alterations that occur in a material or component that result in a reduction in its ability to perform its intended function [29]. Damage can occur due to a variety of factors, including excessive stress, fatigue, corrosion, wear, and other types

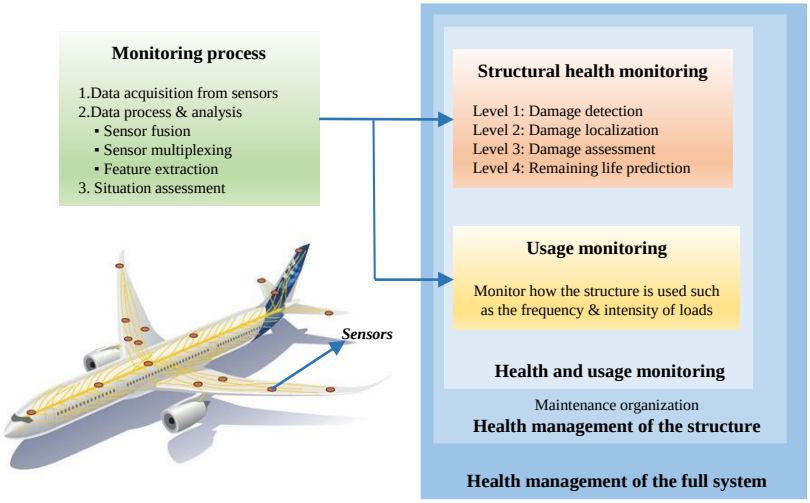

Figure 2.5: Principle and structure of a structural health monitoring system (adapted from the book [27])

of material degradation. There are different types of damage in engineering structures, which include cracks or fractures in a structure, Wear of bearings, delamination of composite materials, Corrosion of pipelines and other metal components due to exposure to corrosive chemicals or environments, etc.

2.4.2. DIFFERENT TYPES OF STRUCTURAL HEALTH MONITORING TECHNOLOGIES

There are several commonly used structural health monitoring techniques, which include fiber optic sensing [30], vibration-based techniques [31], guided wave-based structures [32], etc. The different types of structural health monitoring technologies can be seen in figure 2.6. Fiber optic sensing employs optical fibers to detect strain, temperature, and other physical parameters of a structure. Fiber can be bonded on the surface of the monitored structure or embedded inside the structure [33]. In the process of piezoelectric sensing, the piezoelectric transducer is placed on the surface of the structure being monitored, and it is then subjected to an electrical stimulus which can cause it to vibrate and create a mechanical wave. The wave can travel through the monitored structure, and when there are any defects such as cracks or voids, the wave can be reflected back and detected by the piezoelectric transducer. By analyzing the detected wave, it is possible to detect defects and determine its location [34]. For vibration-based structural health monitoring, the working principle is to monitor dynamic response of the monitored structure and compare them to a baseline or reference state when there are no defects [35]. Vibration-based structural health monitoring methods can generally be classified into three categories based on the vibration parameters: modal analysis, time domain analysis, and time-frequency domain approaches [36].

There has been a lot of research on applying different structural health monitoring tech-

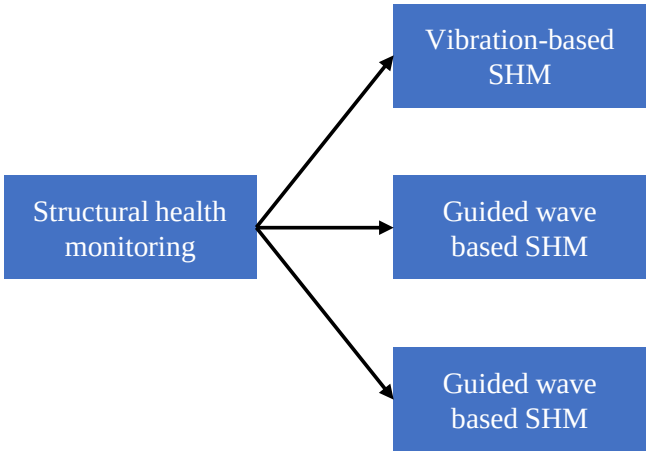

Figure 2.6: Three types of structural health monitoring technologies

niques to various structures. Sanders combined the frequency-sensitive method and internal-state-variable theory to develop a method for detecting and locating damages in CFRP beams [37]. Grouve et al. developed a method based on natural frequency change to detect delaminations in composite beam structures [38]. Ooijevaar et al. employ the modal strain energy damage index algorithm to determine the delamination in a composite T-beam structure [36]. Masserey and Fromme employ the coupled Rayleigh-like wave to detect defects remotely in stiffened plates specimen which is similar to the structural component in the airplane [39]. Achenbach et al. investigated the interaction between guided waves and surface cracks [40]. A crack detection method is developed to detect fatigue cracks on the wing panel with the multisine ultrasonic waves. Guemes et al. measured the strain distribution of CFRP structure with fiber optic sensors and used principal component analysis to process the strain data for damage detection [30]. A hybrid structural health monitoring system was established by combining the fiber optic sensor and piezoelectric transducer, and it was proven to succeed in detecting a through-thickness hole with a 2mm diameter and a surface hole. Based on previous research, a comparison between these different structural health monitoring techniques are conducted, which can be seen in Table 2.1

2.4.3. STRUCTURAL HEALTH MONITORING ON ADDITIVELY MANUFACTURED PARTS

While there are a lot of studies on applying structural health monitoring on composites, there are only a few studies on performing structural health monitoring on additively manufactured parts. It is very difficult to apply most of the current structural

Table 2.1: Comparison of different structural health monitoring techniques

SHM techniques	Pros	Cons
Vibration-based SHM	Provide information on the dynamic behavior;	Require a large number of sensors;
	Be used for very large structures;	Difficult to install in small and complex components;
Guided wave based SHM	High sensitivity and resolution for detecting small changes in the structure;	Require a relatively large number of sensors;
	Be cost-effective;	Limited spatial resolution;
Fiber optic sensor based SHM	Easy to integrate (surface bonding or embedding);	Requires specialized equipment and expertise
	High spatial resolution and accuracy;	

health monitoring techniques due to various reasons. The guided wave based structural health monitoring, for example, is often used on a thin plate, with relatively long widths and/or lengths compared with the wavelength of the propagating wave [41]. The vibration-based structural health monitoring technique requires a relatively large number of sensors distributed throughout the structure, and it may not be practical to install and maintain these sensors in a small and complex part [38].

There are some studies on embedding fiber optic sensors within additively manufactured parts for structural health monitoring. Most existing examples chose to embed the sensor concurrently within the manufacturing process [42]–[44]. More precisely, the AM process is typically interrupted, fiber is placed within the build plane, and subsequent layer-by-layer manufacturing is continued. However, this introduces an issue that high temperature during the embedding process can induce coating degradation or even thermal damage to the fiber. When embedding fiber within the Ti6Al4V part, the melting point of Ti6Al4V (around 1604 °C) is much larger than the maximum working temperature of the fiber optic sensor, which risks permanently damaging the fiber [45]. The general approach to solving this problem is to protect the fiber with metal jackets before embedding; however, this makes the embedding process complex and carries the risk of bonding defects between fiber and host. An example of the difficulty is highlighted by the work of Havermann [45], which can be seen in figure 2.7. In the study, the building process SLM is interrupted, a fiber optic sensor is inserted into the groove, and encapsulation of the fiber is performed by continuing the SLM. Havermann found that bonding imperfections remain between fibers and host material due to lack-of-fusion. Specifically looking at the fiber coating process, Li investigated the application of metal coating through electro-plating and magnetron sputtering. However, the metal coating adds

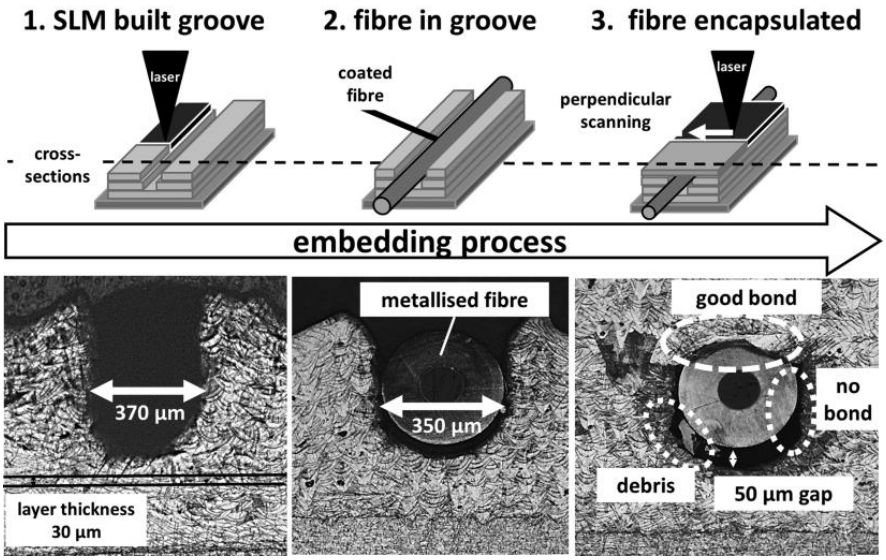

Figure 2.7: The fiber embedding process which is concurrent with the additive manufacturing process from a previous study [45]

more complexity and cost to the fabrication process [46]. A number of other coating and embedding methodologies have been studied, including an electrodeless-electro nickel plating of an optical fiber [42], vacuum brazing of nickel-coated fiber by Sandlin [43], and ultrasonically welding metal coated FBG sensor into aluminum 6061 part by Schomer [47]. In the end, however, the cost and complexity, combined with limited placement freedom to a single-build plane, make the approach of embedding concurrently with manufacturing, quite limiting for this research.

Although not technically embedding a fiber, Strantza [48] fabricated an embedded sensor by integrating a capillary within a part using SLM, as can be seen in figure 2.9. Af-

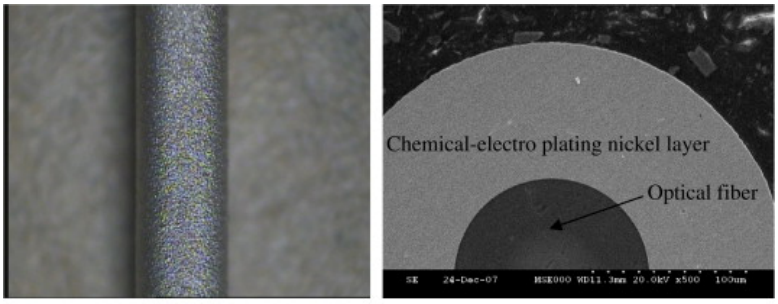

Figure 2.8: (**a**) Overview of the fiber with metal coating; (**a**) cross-section of the coated fiber from [42]

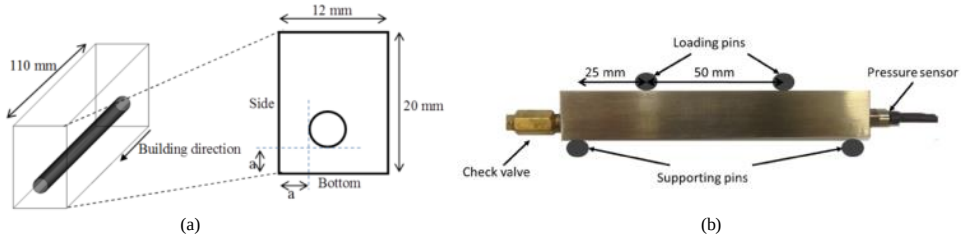

Figure 2.9: (**a**) Schematic representation of an additively manufactured specimen with an integrated capillary, which is also called vacuum sensor; (**B**) The four-point bending test setup to verify the effectiveness of the vacuum sensor, which include the specimen, pressure sensor and check valve

ter fabrication, the capillary could be sealed, a vacuum drawn within the capillary, and a pressure sensor attached, creating an embedded vacuum sensor as presented. The working principle is that if a crack grows up to breach the integrated capillary, it will result in a loss of vacuum, thus indicating the crack.

Although the integrated vacuum sensor concept is subject to limitations the crack needs to be big enough to breach the capillary and the capillary needs to have close proximity to the hot spot, however, it can be further explored as an inspiring concept. One possibility is to combine the printed capillary concept with traditionally employed fiber optic sensors for structural health monitoring. To be more specific, functional parts are printed with pre-defined capillaries in which fibers can be inserted and bonded within the capillary using adhesive resin afterward. The embedding process is easier and doesn't require complex procedures, and provides the most freedom with respect to the path a fiber can take and thus the largest design space for embedding a fiber. Therefore, the approach will be taken in this thesis. However, due to the fact that the capillary size is much larger than the diameter of the fiber, the fiber positions and orientations within the capillary are unknown. That introduces the first sub-research question of this PHD work:

'How does the uncertainty of fiber locations and orientations within the capillary influence the measurement accuracy of the fiber optic sensor? '

2.5. FIBER OPTIC SENSORS

2.5.1. INTRODUCTION TO THE FIBER OPTIC SENSOR

Fiber optic sensors represent a type of sensing technology that employs optical fibers to detect changes in diverse physical properties, such as temperature [49], pressure[50], strain[51], or chemical composition[52]. Fiber optic sensors typically consist of a central core and a surronding cladding, with the cladding possessing a refractive index that is lower than that of the core. The light is confined within the fiber core when injected into the core of the fiber optic cable and then reflected off the interface between the core and the cladding at an angle exceeding the critical angle. When any external stimulus such as strain, temperature, or pressure is exercised on the fiber, the wavelength or intensity from the end of the fiber changes. The change can be further analyzed to determine the

level of the stimulus [53].

Fiber optic sensors can be classified based on different criteria. Based on the physical or optical phenomenon they exploit, optical sensors can be categorized as intensity-based sensors, wavelength-based sensors, polarization-based sensors, Raman scatter-based sensors, Brillouin-based sensors, and interferometric sensors [54]. For the intensity-based fiber optic sensor, light is launched into an optical cable at one end and monitored. A photodetector detects the light at the output end and measures the light's intensity. The photodetector can produce an electrical signal that is proportional to the intensity of the light. Temperature, strain, and pressure can cause changes in the intensity of the light that is transmitted through the fiber, and therefore the electrical signal. This signal can then be processed to obtain information about the temperature, strain or pressure, etc [55]. For instance, changes in temperatures may have an impact on the refractive index of an optical fiber in a temperature-sensitive intensity-based fiber optic sensor. Consequently, this alteration in refractive index directly influences the amount of light that is transmitted through the fiber. The temperature can be calculated by observing these variations in light intensity [56]. The working principle of Raman scatter-based fiber optic sensors is based on the measurement of the Raman shift, which is a measure of the change in wavelength of the scattered light that results from the interaction of light with a material [57]. These variations in the Raman shift can be utilized to learn more about the physical quantity being measured because they are proportional to these physical parameters, such as temperature, pressure, chemical composition or strain [58]. Stress or strain causes a fiber's refractive index to change, and as a result, The induced phases are different between various polarization directions. This is called the photoelastic effect. The external parameters can be sensed by tracking the change in the output polarization states. That is the working principle of polarization-based sensors [59].

2.5.2. COMPARSION BETWEEN FIBER BRAGG GRATING SENSOR AND DISTRIBUTED FIBER OPTIC SENSOR

Based on their configuration, which is how the optical fiber is arranged or configured in the sensing system, fiber optic sensors can also be classified into fiber bragg grating sensors, distributed sensors, etc [60]. Fiber bragg grating sensors use a small section of fiber optic cable that contains a grating structure known as a "Bragg grating.". The grating can reflect light back toward the light source, and the changes between the original light and reflected light can be analyzed to determine the magnitude of the external parameter being measured. Fiber bragg grating sensors are point sensors, which indicate that they can only be used to measure parameters at a specific location [59]. Distributed fiber optic sensor can be used to measure the strain or temperature along its entire length. Instruments such as an optical time-domain reflectometer (OTDR) or optical frequency-domain reflectometer (OFDR) are used to accomplish this. It sends brief light pulses into the fiber and detects the light that is backscattered to ascertain changes in the fiber's properties throughout its length [56]. Compared with distributed fiber optic sensors, FBG has a faster response time, and this is because FBG sensors can be made to react to changes in the physical parameters being measured very rapidly,

with reaction times sometimes falling into the range of microseconds or even nanoseconds [33]. The distributed fiber optic sensor, on the other hand, operates at a lower speed. This is because OFDR or OTDR used in distributed fiber optic sensors detects changes in the backscattered light signal along the length of the fiber, which can be impacted by many factors such as fiber attenuation, reflections, and backscatter [61]. In addition to that, fiber Bragg grating sensors can offer higher sensitivity and accuracy in some applications. However, there are also some advantages of distributed fiber optic sensors over fiber Bragg grating (FBG) sensors. Distributed fiber optic sensors can offer spatial resolutions as small as millimeters or even micrometers by utilizing optical OTDR and OFDR methods, and that makes them ideal for monitoring massive structures like large aerospace structures, bridges, and tunnels because it can deliver measurements with high spatial precision over long distances [62]. In addition, distributed fiber optic sensors can provide measurements without the need for determining the location of individual sensing points, and that is because distributed fiber optic sensors can measure parameters along the whole length of the fiber, allowing for a distributed measurement of the parameter [63]. In comparison, fiber bragg grating sensors require the time-consuming and money-consuming installation of individual sensors at predetermined locations along the fiber. Multiple sensors might be needed in applications where measurements are needed at several points, further adding to the installation's complexity and expense. After comparing the distributed fiber optic sensor and fiber bragg grating sensors, the distributed fiber optic sensor is selected for this study because it can be used to measure strain distribution along its full length.

2.5.3. DISTRIBUTED FIBER OPTIC SENSING

Distributed fiber optic sensing involves several common technologies: Brillouin Scattering, Rayleigh scattering and Raman Scattering. Rayleigh scattering [64] represents the scattering of light as a result of variations in the refractive index of the fiber. By analyzing the backscattered light, the strain or temperature variation can be acquired because the strain or temperature variation can change the fiber's refractive index. The spectral response of Rayleigh scattering includes both the strain component and temperature component, as can be seen in equation 2.1.

$$\frac{\Delta\lambda}{\lambda_B} = K_T \Delta T + K_\epsilon \Delta\epsilon \tag{2.1}$$

In the equation, $\Delta\lambda$ is the change of wavelength influenced by both the strain and temperature, ΔT and $\Delta\epsilon$ represent the change of temperature and strain. K_ϵ and K_T are the intrinsic properties of the optical fiber, and they indicate the strain coefficient and a sum of the thermos-optic coefficient and thermal expansion coefficient [65].

Brillouin scattering happens when light interacts with acoustic waves traveling along the fiber [63]. The distributed fiber can measure the frequency shift of the scattered light in order to determine the strain or temperature. Equation 2.2 represents the relationship between frequency shift, strain, and temperature change [63].

$$\Delta \upsilon_B = C_T \Delta T + C_\epsilon \Delta \epsilon \tag{2.2}$$

In the equation above, C_ϵ and C_T denote the strain and temperature coefficient respectively. $\Delta \upsilon_B$ represents the frequency change induced by the strain or temperature.

Raman scattering occurs when a pulsed light interacted with the vibrational modes of molecules, and the frequency of light shifts [66]. Raman scattering used the Stokes-to-anti-Stokes ratio to sense the distributed temperature, as shown in 2.3 [63].

$$\frac{I_{AS}}{I_S} = (\frac{\lambda_S}{\lambda_{AS}})^4 exp(-\frac{\hbar \omega_m}{k_B T}) \tag{2.3}$$

Where λ_{AS} and λ_S denote the wavelength of anti-stokes Raman peaks and stokes Raman peaks respectively, I_{AS} and I_S represent the intensity of anti-stokes Raman peaks and stokes Raman peaks respectively. k_B, ω_m, and $\hbar$ denote the Boltzmann constant, the angular frequency for a harmonic oscillator, and the reduced Planck constant respectively.

Both the Rayleigh scattering and Brillouin scattering technologies are often used for both strain and temperature sensing, and therefore they are often utilized in structural health monitoring. However, the Raman scattering is often applied for temperature sensing [63].

2.6. STRUCTURAL HEALTH MONITORING BASED ON STRAIN DATA MEASURED FROM FIBER OPTIC SENSOR

2.6.1. THE STRAIN THEORY

Mechanical strain refers to the deformation of a structure when subjected to an external force or load. Normal strain and shear strain are two different forms of strain. Depending on the type and magnitude of the load, as well as the properties of the materials used in the structure [67]. The deformation of an engineering structure often occurs in different phases. In engineering structures with sufficient ductility, there are typically three major phases of deformation. The first phase is the elastic deformation phase, which occurs when the structure's deformation is reversible and the material returns to its original shape when the external force is withdrawn. Elastic deformation is proportional to the applied stress and is determined by the material's elastic modulus. The subsequent phase is plastic deformation, which occurs when the structure undergoes plastic deformation because the applied stress surpasses the yield strength of the material [68]. If the applied stress exceeds the ultimate strength of the material, the structure may fail, which may take the form of fracture, buckling, or collapse.

There are different theories to define and explain the strain. The theory of infinitesimal strain assumes that a structure's deformation is substantially smaller than its body dimension. In other words, it presupposes that the structural deformation is small enough to be deemed elastic and that the shape change is minimal. Typically, for modern engineering structures, the structures are designed to work within their elastic range, meaning that deformation is reversible and the material returns to its original shape when the

external force is removed. Therefore, the theory of infinitesimal strain [69] is widely used in many different engineering applications.

2.6.2. INFLUENCE OF DAMAGE ON THE STRAIN FIELD

Stress and strain are distributed throughout a structure when it is exposed to an external load. However, if there is a change in geometry or material properties, such as a crack, notch, or tiny hole, the stress, and strain may become more concentrated, resulting in increased levels of stress and strain in those areas [68]. That is called the strain concentration. Due to the existence of the constitutive law correlating stress and strain, the strain concentration can be considered equivalent to the stress concentration. The stress concentration can be denoted by the stress concentration factor K_t. It is a dimensionless factor that relates the maximum stress at a stress concentration point to the nominal stress at the same location in the absence of the stress concentration [70]. Therefore, a greater value of K_t implies a greater stress concentration. The importance of the stress concentration factor (K_t) depends on the material and loading conditions. Some materials are more susceptible than others to stress concentration. For instance, brittle materials such as ceramics and glass are more prone to stress concentrations because they are less capable of deforming and absorbing stresses than ductile materials such as aluminum alloys. Moreover, the significance of stress concentration depends on the nature of the load [71]. Under fatigue loads, stress concentration can act as the stress raiser, promoting the initiation and propagation of cracks, which can lead to fatigue failure. Therefore, one should consider the influence of stress concentration when designing a structure for fatigue loading.

According to Saint-Venant's principle [68], as the distance away from a localized stress concentration increases, the stress distribution also becomes less dependent on the stress concentration. In other words, as the distance from the stress concentration increases, the stress distribution gets more uniform and finally approaches the stress distribution that would occur if the stress concentration did not exist. Therefore, the magnitude of the stress concentration drops as the distance from the stress concentration increases. This principle applies to linear elastic materials and assumes homogeneous material behavior and that the stresses remain within the elastic limit. Figure 2.10 shows an example [72] of how the stress distribution becomes less impacted by the stress concentration as the distance from the stress concentration grows.

2.6.3. STATE-OF-ART OF STRAIN-BASED CRACK DETECTION METHOD

BASELINE STRAIN REFERENCE METHOD FOR CRACK DETECTION

The strain-based damage detection method relies on the redistribution of strain caused by damage. For example, the existence of cracks can cause strain distortions due to stress/strain concentration as mentioned before. Some researchers use the baseline strain reference method to detect cracks. Martin [73] used distributed fiber optic sensors to measure strain changes in a concrete beam subjected to different loading conditions. They compared the strain values measured during normal operation of the beam with measured strain distribution corresponding to different crack lengths. The cracks can be identified when clear strain peaks were observed. Menendez and Guemes [74] bonded

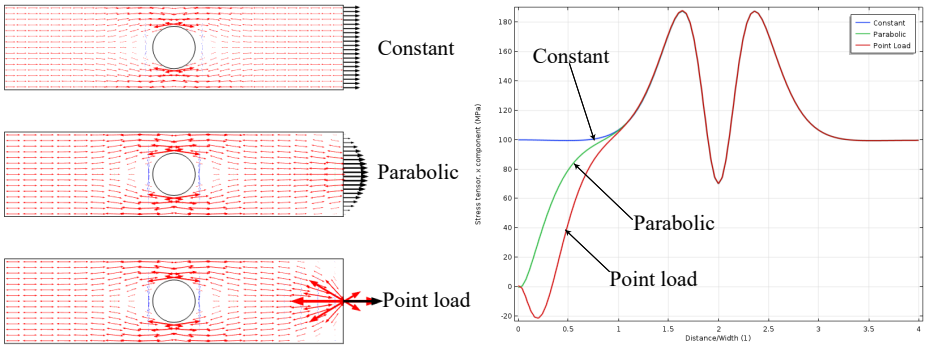

Figure 2.10: (**a**) Principal stress plot for the three load cases; (**b**) Stress along the upper edge as a function of the distance from the loaded boundary. The distance is normalized by the width of the plate. [72]

the fiber optic sensors on the surface of composites and observed the strain disturbations around the gratings as the composite skin and stiffeners debonded. Feng et al. used the strain discontinuities along the strain distribution from theoretical analysis to determine the location of cracks. In the study, the distortion effect due to the strain averaging of the BOTDR-Distributed fiber optic sensors is also studied [75]. Even though the damaged detection method based on comparing the strain when the monitored structure is at different states is proven effective in the studies mentioned above, measurement noise of the strain can affect the accuracy and reliability of the method. To be more specific, measurement noise in the fiber optic sensor can mask the strain distribution changes associated with damage or cracks in the structure. As a result, the damage distribution may not be easily distinguishable, leading to false negatives in the damage detection process. Xu et al. employed the stationary wavelet transform to first denoise the strain signal measured by fiber optic sensors, and extract damage-related features, and the method is verified with a 15m-long beam structure with simulated damages [76].

In this study, the fiber optic sensor is embedded in a capillary inside the additively manufactured part, the fiber locations and orientations are unknown, and therefore the strain distribution measured by the fiber optic sensor has as a complex pattern. It may be very difficult to distinguish the strain distributions measured at different states of the monitored structure. Instead of setting the measured strain distribution when the monitored structure is in a healthy state as the baseline strain distribution, the strain distributions along the capillary boundaries are set as baselines. The new baselines make up a strain window, and the measured strain distributions will be compared against the new baselines. Whenever the measured strain exceeds the strain window, the damage can be detected. Here the second sub-research question of the PHD work is introduced:

'How effective is the strain-exceeding based method for detecting cracks in additively manufactured parts with embedded fiber optic sensors? '

MACHINE LEARNING BASED CRACK DETECTION METHOD

There are some limitations of the strain comparison based damage detection method. The first limitation is the inability to detect early-stage damage. Sierra[77] used the principal component analysis on strain distribution measured by fiber optic sensors to perform damage detection and localization on wind turbines. In addition, the second limitation is that the method only uses very limited information such as the damaged-induced strain peaks for damage detection. This requires the crack to be big enough for strain-induced disturbances to be visible with human eyes. Some researchers used more advanced methods such as machine learning based methods for damage detection [78], [79]. The machine learning approach can be used to learn patterns from the strain distribution measured by distributed fiber optic sensors. Song employs the artificial neural network to extract features from the full-scale strain distributed measured by Brillouin optical time-domain analysis (BOTDA)-based distributed fiber optic sensor [80]. Katsikeros and Labeas used simulated strain data to train an artificial neural network (ANN) model and the capabilities and limitations of this technique were investigated by applying it on an aircraft cracked lap-joint structure [81]. However, in the previous studies using machine learning for damage detection, the fiber optics sensors were bonded to the structure surface, and the location and orientation of the fiber are known. In this study, due to the fact that the locations and orientations of the embedded fiber are unknown, the fiber can be at any locations within the capillary and any orientations can also be possible as long as it is within the fiber bending limit. That makes it very hard to get enough strain distribution data so that all locations and orientations of the embedded fibers are considered for training a machine learning model. Therefore, the third sub-research question is introduced:

'How can we use the deep neural network based method to detect any crack within the monitored structure using the measured strain distribution with the embedded fiber optic sensors? '

MACHINE LEARNING AND DEEP NEURAL NETWORKS FOUNDATION

Machine learning, as a part of artificial intelligence (AI), is focused on the development of models and algorithms that enable computers to acquire information autonomously and make predictions or choices. The process encompasses the acquisition of information from data, the detection of regularities, and the formulation of informed judgments or predictions. The main idea underlying machine learning is the development of mathematical models that can learn from and make decisions based on data. Instead of being explicitly encoded with different rules and instructions, machine learning algorithms are intended to learn and develop automatically from experience or examples.

Machine learning can be used for both classification and regression. In regression, the prediction result is a continuous number, and for classification, the result is discrete. In this study, the machine learning model is used for classification because the prediction result is binary (There is a crack in the monitored structure/There is no crack in the monitored structure).

There are traditional machine learning and deep learning algorithms. the traditional machine learning algorithm requires substantial domain knowledge to extract damage-

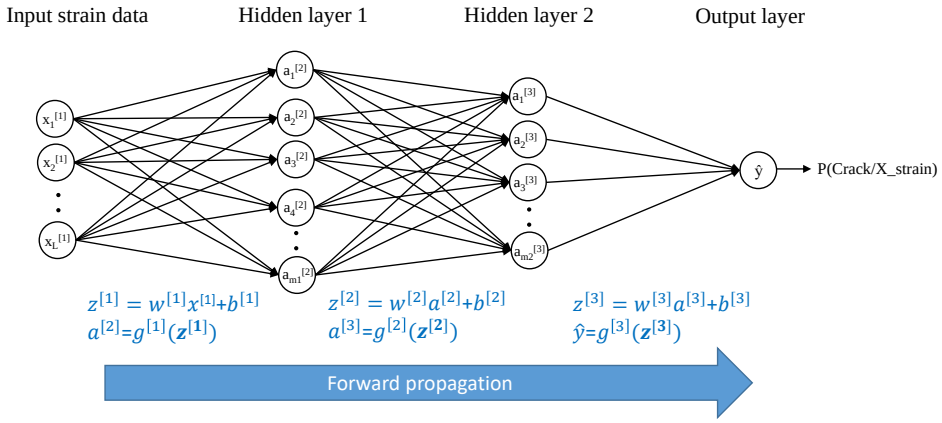

Figure 2.11: The forward propagation of the DNN model, which can map the input strain distributions to the target probability

sensitive features from the raw data. Deep learning approaches such as deep neural networks can use the raw data as the input, and automatically extract damage-sensitive features during the training process. Due to the advantage of the deep neural networks (DNN) model, it will be used in this study for classification.

Deep neural networks consist of three primary constituents: the input layer, hidden layers, and output layer. The input layer is responsible for receiving raw data, which is then subjected to transformation and processing via one or more hidden levels. The output layer produces a prediction or classification outcome by using the input data. As shown in figure 2.11, the proposed DNN includes one input layer, two hidden layers, and one output layer. The input layer, first hidden layer, and second hidden layer have L, $m1$, and $m2$ neurons respectively.

The DNN generates its output from input data through forward propagation. Calculating the weighted sum and using an activation function are the two main components of forward propagation. Specifically, for each layer, the first step is to compute the weighted sum of the input values and the weights associated with each neuron in the network. The process entails the multiplication of the input vector with its matching weight vector w, followed by the addition of the bias vector b. The weighted sum is then fed into an activation function, introducing nonlinearity into the neuron's output. The relu function is used as the activation for the input layer and hidden layers. The sigmoid function $g(z)$ shown in equation 2.4 is chosen as the activation in output layer. The sigmoid function can be used as an activation function because it is differentiable. Therefore in the back-propagation algorithm, the weights can be updated easily in a neural network during training. Additionally, the output of the sigmoid function can be interpreted as a probability, which is useful in binary classification.

$$s(x) = \frac{1}{1+e^{-x}} \tag{2.4}$$

During forward propagation, each neuron in the network receives input from the preceding layer and generates output, which is then transmitted to the next layer. This procedure is repeated until the final output, which represents the predicted probability that there is a crack in the monitored structure for the given strain distribution, is produced.

In order to let the DNN learn an accurate mapping or function from the input strain data to a probability, it is necessary to train the neural network. Through training, the weights and biases are updated so the DNN can produce accurate outputs for inputs it has not seen before. In this study, The free weights parameters w and bias parameters b are updated based on the data set $(x_1, y_1), (x_2, y_2), (x_3, y_3), ..., (x_m, y_m)$ by minimizing the cost function $L(\hat{y}, y)$.

$$L(\hat{y}, y) = -\frac{1}{m}(\sum_{i=1}^{m}(-y_i \log(\hat{y}_i) - (1-y_i)\log(1-\hat{y}_i)) + \frac{\lambda}{2m}\sum_{l=1}^{L-1}\sum_{i=1}^{s_l}\sum_{j=1}^{s_{l+l}}(w_{ji}^{l})^2 \tag{2.5}$$

x_i is the i^{th} strain sample, which is the extracted strain value sequence, y_i is the true target value 1 or 0 for the i^{th} strain sample and both of them are prepared in section 5.2.1. $\hat{y}_i$ is the output the of DNN model, which is the predicted target value for the ith strain sample. L is the total number of layers, s_l is the total number of neurons in the l layer, and w is the weight coefficient. The optimal value of the weight w and bias b can be estimated by minimizing the cost function $L(\hat{y}, y)$. The optimization process is implemented by the mini-batch gradient descent algorithm when taking the dataset size into consideration.

2.7. SPECIMENS GEOMETRY AND TEST

In order to facilitate a comparison of the performance with the vacuum sensor methodology proposed by this study with Strantza's study, the same beam structure and the four-point bending test for initiating the crack are adopted. The specimen geometry and test setup for Strantza's study can be seen in figure 2.9. The specimen geometry for this study can be seen in figure 2.12, where b, h, L and d denote the specimen width, height, length, and diameter of the capillary respectively. The spacing a of the load introduction points results in a constant internal bending moment, $M = Fa$, along the central part of the beam denoted by w. In this study, L = 110mm, b = 12 mm, h = 20 mm. The specimen geometry and size to be used for analytical, numerical, and experimental analysis in this study.

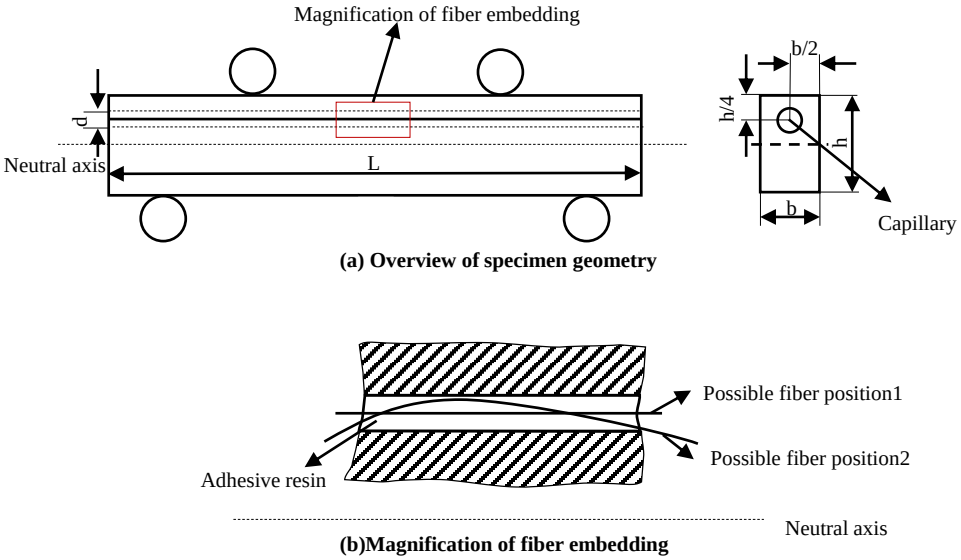

Figure 2.12: Schematic illustration of a beam structure with embedded fiber optic sensor under four-point bending

BIBLIOGRAPHY

[1] I. Gibson, D. Rosen, B. Stucker, *et al.*, "Development of additive manufacturing technology", *Additive manufacturing technologies*, pp. 23–51, 2021.

[2] M. Schmid, A. Amado, and K. Wegener, "Polymer powders for selective laser sintering (sls)", in *AIP Conference proceedings*, AIP Publishing LLC, vol. 1664, 2015, p. 160 009.

[3] A. D. Mazurchevici, D. Nedelcu, and R. Popa, "Additive manufacturing of composite materials by fdm technology: A review", 2020.

[4] T. G. Spears and S. A. Gold, "In-process sensing in selective laser melting (slm) additive manufacturing", *Integrating Materials and Manufacturing Innovation*, vol. 5, no. 1, pp. 16–40, 2016.

[5] N. Balc, P. Berce, and R. Pacurar, "Comparison between slm and sls in producing complex metal parts.", *Annals of DAAAM & Proceedings*, 2010.

[6] N. Sanaei, A. Fatemi, and N. Phan, "Defect characteristics and analysis of their variability in metal l-pbf additive manufacturing", *Materials & Design*, vol. 182, p. 108 091, 2019.

[7] J. C. Najmon, S. Raeisi, and A. Tovar, "Review of additive manufacturing technologies and applications in the aerospace industry", *Additive manufacturing for the aerospace industry*, pp. 7–31, 2019.

[8] H. E. Helmer, C. Körner, and R. F. Singer, "Additive manufacturing of nickel-based superalloy inconel 718 by selective electron beam melting: Processing window and microstructure", *Journal of Materials Research*, vol. 29, no. 17, pp. 1987–1996, 2014.

[9] S. Liu and Y. C. Shin, "Additive manufacturing of ti6al4v alloy: A review", *Materials & Design*, vol. 164, p. 107 552, 2019.

[10] I. Rosenthal, A. Stern, and N. Frage, "Microstructure and mechanical properties of alsi10mg parts produced by the laser beam additive manufacturing (am) technology", *Metallography, Microstructure, and Analysis*, vol. 3, pp. 448–453, 2014.

[11] B. Dutta and F. S. Froes, "The additive manufacturing (am) of titanium alloys", *Metal powder report*, vol. 72, no. 2, pp. 96–106, 2017.

[12] N. T. Aboulkhair, M. Simonelli, L. Parry, I. Ashcroft, C. Tuck, and R. Hague, "3d printing of aluminium alloys: Additive manufacturing of aluminium alloys using selective laser melting", *Progress in materials science*, vol. 106, p. 100 578, 2019.

[13] J. Plocher and A. Panesar, "Review on design and structural optimisation in additive manufacturing: Towards next-generation lightweight structures", *Materials & Design*, vol. 183, p. 108 164, 2019.

[14] J. Kranz, D. Herzog, and C. Emmelmann, "Design guidelines for laser additive manufacturing of lightweight structures in tial6v4", *Journal of Laser Applications*, vol. 27, no. S1, S14001, 2015.

[15] J. Bamberg, K.-H. Dusel, and W. Satzger, "Overview of additive manufacturing activities at mtu aero engines", in *AIP Conference Proceedings*, American Institute of Physics, vol. 1650, 2015, pp. 156–163.

[16] J. Immarigeon, R. Holt, A. Koul, L. Zhao, W. Wallace, and J. Beddoes, "Lightweight materials for aircraft applications", *Materials characterization*, vol. 35, no. 1, pp. 41–67, 1995.

[17] M. Munsch, E. Wycisk, J. Kranz, V. Seyda, and E. Claus, "Functional products through laser additive manufacturing of tial6v4", in *Workshop LAM Laser Additive Manufacturing*, 2012.

[18] L. J. Kumar and C. Krishnadas Nair, "Current trends of additive manufacturing in the aerospace industry", *Advances in 3D printing & additive manufacturing technologies*, pp. 39–54, 2017.

[19] R. I. Ratul and A. D. Rudra, "New aerospace surface treatments and their prospects",

[20] D. Dimitrov, E. Uheida, G. Oosthuizen, *et al.*, "Manufacturing of high added value titanium components. a south african perspective", in *IOP Conference Series: Materials Science and Engineering*, IOP Publishing, vol. 430, 2018, p. 012 009.

[21] N. Sanaei and A. Fatemi, "Defects in additive manufactured metals and their effect on fatigue performance: A state-of-the-art review", *Progress in Materials Science*, vol. 117, p. 100 724, 2021.

[22] A. Y. Al-Maharma, S. P. Patil, and B. Markert, "Effects of porosity on the mechanical properties of additively manufactured components: A critical review", *Materials Research Express*, vol. 7, no. 12, p. 122 001, 2020.

[23] A. S. Wu, D. W. Brown, M. Kumar, G. F. Gallegos, and W. E. King, "An experimental investigation into additive manufacturing-induced residual stresses in 316l stainless steel", *Metallurgical and Materials Transactions A*, vol. 45, pp. 6260–6270, 2014.

[24] M. De Giorgi, A. Scialpi, F. Panella, and L. De Filippis, "Effect of shoulder geometry on residual stress and fatigue properties of aa6082 fsw joints", *Journal of Mechanical Science and Technology*, vol. 23, pp. 26–35, 2009.

[25] K. Shiyas and R. Ramanujam, "A review on post-processing techniques of additively manufactured metal parts for improving the material properties", *Materials Today: Proceedings*, vol. 46, pp. 1429–1436, 2021.

[26] *Spider bracket topology optimization project by materialise*. [Online]. Available: https://www.materialise.com/en/inspiration/cases/spider-bracket-topology-optimization.

[27] D. Balageas, C.-P. Fritzen, and A. Güemes, *Structural health monitoring*. John Wiley & Sons, 2010, vol. 90.

[28] K. Worden and G. Manson, "The application of machine learning to structural health monitoring", *Philosophical Transactions of the Royal Society A: Mathematical, Physical and Engineering Sciences*, vol. 365, no. 1851, pp. 515–537, 2007.

[29] J. Mazars and G. Pijaudier-Cabot, "From damage to fracture mechanics and conversely: A combined approach", *International journal of solids and structures*, vol. 33, no. 20-22, pp. 3327–3342, 1996.

[30] A. Güemes, A. Fernández-López, P. F. Dıéaz-Maroto, A. Lozano, and J. Sierra-Perez, "Structural health monitoring in composite structures by fiber-optic sensors", *Sensors*, vol. 18, no. 4, p. 1094, 2018.

[31] D. Montalvao, N. M. M. Maia, and A. M. R. Ribeiro, "A review of vibration-based structural health monitoring with special emphasis on composite materials", *Shock and vibration digest*, vol. 38, no. 4, pp. 295–324, 2006.

[32] M. Mitra and S. Gopalakrishnan, "Guided wave based structural health monitoring: A review", *Smart Materials and Structures*, vol. 25, no. 5, p. 053 001, 2016.

[33] R. Di Sante, "Fibre optic sensors for structural health monitoring of aircraft composite structures: Recent advances and applications", *Sensors*, vol. 15, no. 8, pp. 18 666–18 713, 2015.

[34] A. Raghavan, "Guided-wave structural health monitoring", Ph.D. dissertation, 2007.

[35] Y. Yang, Y. Zhang, and X. Tan, "Review on vibration-based structural health monitoring techniques and technical codes", *Symmetry*, vol. 13, no. 11, p. 1998, 2021.

[36] T. Ooijevaar, R. Loendersloot, L. Warnet, A. de Boer, and R. Akkerman, "Vibration based structural health monitoring of a composite t-beam", *Composite Structures*, vol. 92, no. 9, pp. 2007–2015, 2010.

[37] D. Sanders, Y. Kim, and N. Stubbs, "Nondestructive evaluation of damage in composite structures using modal parameters", *Experimental mechanics*, vol. 32, pp. 240–251, 1992.

[38] W. J. B. Grouve, L. Warnet, A. de Boer, R. Akkerman, and J. Vlekken, "Delamination detection with fibre bragg gratings based on dynamic behaviour", *Composites Science and Technology*, vol. 68, no. 12, pp. 2418–2424, 2008.

[39] B. Masserey and P. Fromme, "Surface defect detection in stiffened plate structures using rayleigh-like waves", *Ndt & E International*, vol. 42, no. 6, pp. 564–572, 2009.

[40] J. D. Achenbach, A. K. Gautesen, and D. A. Mendelsohn, "Ray analysis of surface-wave interaction with an edge crack", 2016.

[41] A. Modir and I. Tansel, "Structural health monitoring of additively manufactured parts by combining infill design, multiple pulse width excitation (mpwe), and deep learning", *Journal of Vibration Engineering & Technologies*, vol. 10, no. 8, pp. 3227–3238, 2022.

[42] Y. Li, Z. Hua, F. Yan, and P. Gang, "Metal coating of fiber bragg grating and the temperature sensing character after metallization", *Optical Fiber Technology*, vol. 15, no. 4, pp. 391–397, 2009.

[43] S. Sandlin, T. Kosonen, A. Hokkanen, and L. Heikinheimo, "Use of brazing technique for manufacturing of high temperature fibre optical temperature and displacement transducer", *Materials Science and Technology*, vol. 23, no. 10, pp. 1249–1255, 2007.

[44] A. Hehr, M. Norfolk, J. Wenning, *et al.*, "Integrating fiber optic strain sensors into metal using ultrasonic additive manufacturing", *Jom*, vol. 70, pp. 315–320, 2018.

[45] D. Havermann, J. Mathew, W. N. MacPherson, R. R. Maier, and D. P. Hand, "Temperature and strain measurements with fiber bragg gratings embedded in stainless steel 316", *Journal of lightwave technology*, vol. 33, no. 12, pp. 2474–2479, 2014.

[46] X. Li, *Embedded sensors in layered manufacturing*. Stanford University, 2001.

[47] J. J. Schomer, A. J. Hehr, and M. J. Dapino, "Characterization of embedded fiber optic strain sensors into metallic structures via ultrasonic additive manufacturing", in *Sensors and Smart Structures Technologies for Civil, Mechanical, and Aerospace Systems 2016*, SPIE, vol. 9803, 2016, pp. 587–596.

[48] D. De Baere, M. Strantza, M. Hinderdael, W. Devesse, and P. Guillaume, "Effective structural health monitoring with additive manufacturing", in *EWSHM-7th European workshop on structural health monitoring*, 2014.

[49] K. Kyuma, S. Tai, T. Sawada, and M. Nunoshita, "Fiber-optic instrument for temperature measurement", *IEEE Transactions on Microwave Theory and Techniques*, vol. 30, no. 4, pp. 522–525, 1982.

[50] É. Pinet, "Pressure measurement with fiber-optic sensors: Commercial technologies and applications", in *21st International Conference on Optical Fiber Sensors*, SPIE, vol. 7753, 2011, pp. 51–54.

[51] M. Ramakrishnan, G. Rajan, Y. Semenova, and G. Farrell, "Overview of fiber optic sensor technologies for strain/temperature sensing applications in composite materials", *Sensors*, vol. 16, no. 1, p. 99, 2016.

[52] K. Wood, T. Brown, R. Rogowski, and B. Jensen, "Fiber optic sensors for health monitoring of morphing airframes: Ii. chemical sensing using optical fibers with bragg gratings", *Smart materials and structures*, vol. 9, no. 2, p. 170, 2000.

[53] K. Grattan and T. Sun, "Fiber optic sensor technology: An overview", *Sensors and Actuators A: Physical*, vol. 82, no. 1-3, pp. 40–61, 2000.

[54] E. Udd, "An overview of fiber-optic sensors", *review of scientific instruments*, vol. 66, no. 8, pp. 4015–4030, 1995.

[55] S.-J. Choi, Y.-C. Kim, M. Song, and J.-K. Pan, "A self-referencing intensity-based fiber optic sensor with multipoint sensing characteristics", *Sensors*, vol. 14, no. 7, pp. 12 803–12 815, 2014.

[56] E. Udd and W. B. Spillman Jr, *Fiber optic sensors: an introduction for engineers and scientists*. John Wiley & Sons, 2011.

[57] G. Bolognini and A. Hartog, "Raman-based fibre sensors: Trends and applications", *Optical Fiber Technology*, vol. 19, no. 6, pp. 678–688, 2013.

[58] D. K. Gifford, S. T. Kreger, A. K. Sang, *et al.*, "Swept-wavelength interferometric interrogation of fiber rayleigh scatter for distributed sensing applications", in *Fiber Optic Sensors and Applications V*, SPIE, vol. 6770, 2007, pp. 106–114.

[59] K. Fidanboylu and H. Efendioglu, "Fiber optic sensors and their applications", in *5th International Advanced Technologies Symposium (IATS'09)*, vol. 6, 2009, pp. 2–3.

[60] S. Yin, P. B. Ruffin, and T. Francis, *Fiber optic sensors*. CRC press, 2017.

[61] X. Liu, B. Jin, Q. Bai, Y. Wang, D. Wang, and Y. Wang, "Distributed fiber-optic sensors for vibration detection", *Sensors*, vol. 16, no. 8, p. 1164, 2016.

[62] D. Inaudi and B. Glisic, "Distributed fiber optic strain and temperature sensing for structural health monitoring", in *Proceedings of the Third International Conference on Bridge Maintenance, Safety and Management, Porto, Portugal*, 2006, pp. 16–19.

[63] X. Bao and L. Chen, "Recent progress in distributed fiber optic sensors", *sensors*, vol. 12, no. 7, pp. 8601–8639, 2012.

[64] M. Froggatt and J. Moore, "High-spatial-resolution distributed strain measurement in optical fiber with rayleigh scatter", *Applied optics*, vol. 37, no. 10, pp. 1735–1740, 1998.

[65] S. T. Kreger, A. K. Sang, D. K. Gifford, and M. E. Froggatt, "Distributed strain and temperature sensing in plastic optical fiber using rayleigh scatter", in *Fiber Optic Sensors and Applications VI*, SPIE, vol. 7316, 2009, pp. 85–92.

[66] J. Dakin, D. Pratt, G. Bibby, and J. Ross, "Distributed optical fibre raman temperature sensor using a semiconductor light source and detector", *Electronics letters*, vol. 13, no. 21, pp. 569–570, 1985.

[67] R. R. Craig Jr and E. M. Taleff, *Mechanics of materials*. John Wiley & Sons, 2020.

[68] J. T. Oden, E. A. Ripperger, and H. Saunders, "Mechanics of elastic structures", 1982.

[69] J. Sierra Pérez, "Smart aeronautical structures: Development and experimental validation of a structural health monitoring system for damage detection", Ph.D. dissertation, Aeronauticos, 2014.

[70] A. C. Eringen and B. S. Kim, "Stress concentration at the tip of crack", *Mechanics Research Communications*, vol. 1, no. 4, pp. 233–237, 1974.

[71] D. Arola and C. Williams, "Estimating the fatigue stress concentration factor of machined surfaces", *International Journal of fatigue*, vol. 24, no. 9, pp. 923–930, 2002.

[72] H. Sönnerlind, *Applying and interpreting saint-venant's principle*. [Online]. Available: https://www.comsol.com/blogs/applying-and-interpreting-saint-venants-principle/.

[73] X. Chapeleau, J. Blanc, P. Hornych, J.-L. Gautier, and J. Carroget, "Use of distributed fiber optic sensors to detect damage in a pavement", *Asph. Pavements*, pp. 449–457, 2014.

[74] J. Menéndez and A. Güemes, "Shm using fiber sensors in aerospace applications", *18th international conference of optical fibre sensors*, p. 38, 2006.

[75] X. Feng, J. Zhou, C. Sun, X. Zhang, and F. Ansari, "Theoretical and experimental investigations into crack detection with botdr-distributed fiber optic sensors", *Journal of Engineering Mechanics*, vol. 139, no. 12, pp. 1797–1807, 2013.

[76] H.-z. Xu and D. Zhang, "Wavelet-based data processing for distributed fiber optic sensors", in *2006 International Conference on Machine Learning and Cybernetics*, IEEE, 2006, pp. 4040–4045.

[77] J. Sierra-Pérez, M. A. Torres-Arredondo, and A. Güemes, "Damage and nonlinearities detection in wind turbine blades based on strain field pattern recognition. fbgs, obr and strain gauges comparison", *Composite Structures*, vol. 135, pp. 156–166, 2016.

[78] P. Iannelli, F. Angeletti, P. Gasbarri, M. Panella, and A. Rosato, "Deep learning-based structural health monitoring for damage detection on a large space antenna", *Acta Astronautica*, vol. 193, pp. 635–643, 2022.

[79] M. Azimi, A. D. Eslamlou, and G. Pekcan, "Data-driven structural health monitoring and damage detection through deep learning: State-of-the-art review", *Sensors*, vol. 20, no. 10, p. 2778, 2020.

[80] Q. Song, Y. Chen, E. Abdoli Oskoui, *et al.*, "Micro-crack detection method of steel beam surface using stacked autoencoders on massive full-scale sensing strains", *Structural Health Monitoring*, vol. 19, no. 4, pp. 1175–1187, 2020.

[81] C. E. Katsikeros and G. Labeas, "Development and validation of a strain-based structural health monitoring system", *Mechanical systems and signal processing*, vol. 23, no. 2, pp. 372–383, 2009.

3

INVESTIGATING THE MEASUREMENT ACCURACY OF AN EMBEDDED FIBER IN SELECTIVELY LASER MELTED BEAM STRUCTURES

3.1. INTRODUCTION

WHEN a fiber is embedded into a specimen using capillaries, due to the fact that the diameter of a capillary is normally larger than that of a fiber for ease of embedding, the fiber could not be placed at an exact position. Ideally, the fiber is placed along the capillary center and the strain is measured along the axis of the fiber at the capillary center, however, it could be anywhere within the capillary in reality, as shown in figure 3.1. The fiber positions and orientations uncertainty could also lead to strain measurement uncertainty. The measured strain distributions will be different from the strain distributions along the capillary center in an ideal situation. The differences bring up an issue of strain measurement accuracy. This chapter aims to study the positions and orientations variations of the fiber embedded into specimens using capillaries, how fiber positions and orientations variations influence strain measurement accuracy for specimens, and the range of the measured strain distribution.

As this study focuses on fiber position and orientation variations within capillaries, the geometries of used specimens are simplified, and four-point tests are performed, as shown in figure 3.1. There are two reasons for adopting the specimen geometry and four-point bending tests. The first one is that the specimen geometry is the same as that in a previous study [1] on crack detection with vacuum sensors in SLM specimens, so the performance of the proposed crack detection approach can be easily compared with the previous study. Secondly, the four-point bending can create a region with a constant bending moment between the two loading pins. In the region, the influence of fiber locations and orientations can be highlighted and the influence of bending moment does not need to be considered. Traditionally machined specimens will be used for testing, as potential defects in additively manufactured specimens will affect strain measurement accuracy otherwise.

More specifically, an analytical model based on Euler-Bernoulli beam theory was developed to predict strain distribution along the embedded fiber, which is assumed to be along the capillary center shown as the ideal position of fiber in figure 3.1. The Euler-Bernoulli beam theory assumes the beam under bending is sufficiently slender (i.e.: has a slenderness ratio (length to thickness) greater than 10), however, the specimen in this study has a slenderness ratio slightly less than 10. Therefore, a finite element model was created to predict the strain distribution at the same location as in the analytical model. In order to verify the predictive models, static four-point bending tests are performed on the three Aluminum 6082 parts with embedded fiber optic sensors under 8kN. After the four-point bending test, the specimen was cut to observe the real location of an embedded fiber in a capillary, and the predicted strain distribution along the embedded fiber was updated with the real location of the embedded fiber. For verifying the predictive model, the measured strain distribution from the embedded fiber optic sensor was compared with the predicted strain distribution at the real fiber location. An overview of the process can be seen in figure 3.2.

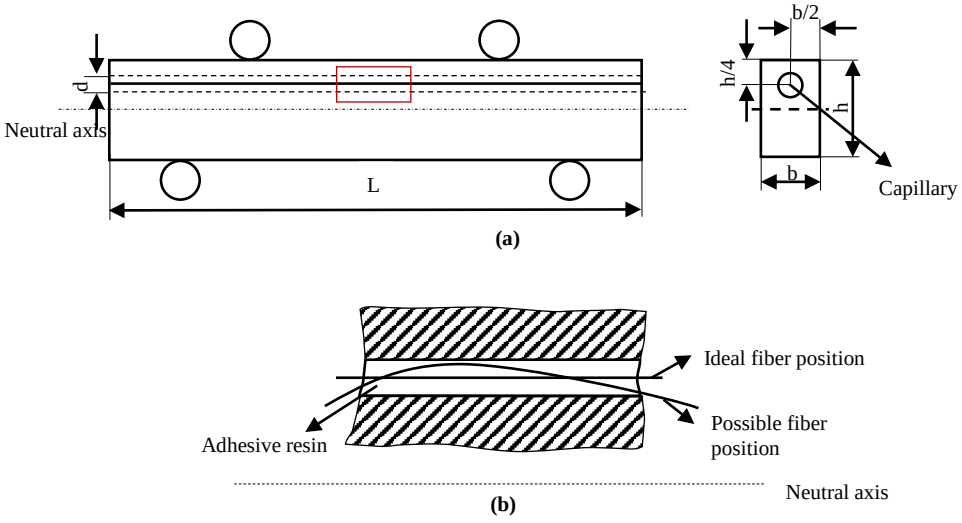

Figure 3.1: (**a**) The schematic representation of the specimen under four-point bending; (**b**) Magnification of the embedded fiber at the ideal position and other possible position

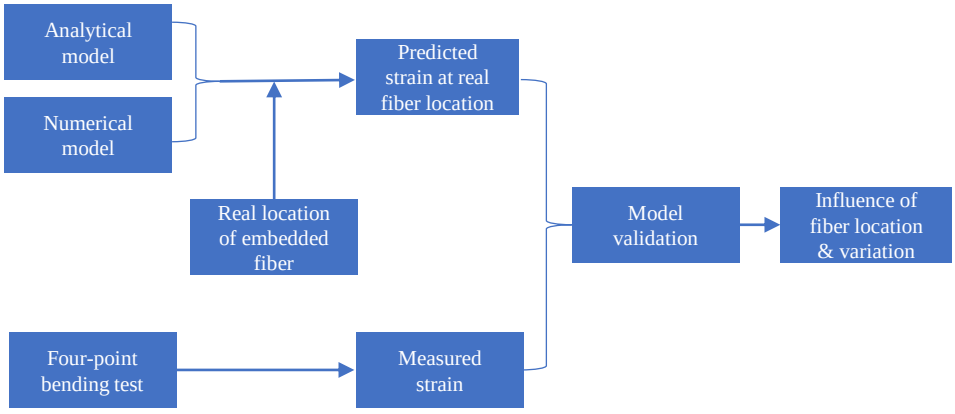

Figure 3.2: Overview of the methodology

3.2. STRAIN DISTRIBUTION PREDICTION WITH A SIMPLIFIED ANALYTICAL MODEL

In order to investigate the influence of fiber position and orientation on the expected strain fiber optic sensors would observe, a simple analytical model was made. The model focuses on the central portion of the specimen (denoted by width w in) where the bending moment is constant. Along this section, the normal stress due to bending σ_z can be described using Euler-Bernoulli beam theory which can be seen in [2]:

$$\sigma_z = \frac{My}{I} \tag{3.1}$$

Where M is the bending moment and is given by $M = Fa$, y is the distance from the neutral axis, and I_{xx} is the moment of inertia around the neutral axis. As this section of the specimen is under pure bending loading, there are no other stress components, allowing the normal strain ε_z, to be calculated simply by dividing the stress by Young's Modulus E.

$$\varepsilon_x = \frac{\sigma_x}{E} = \frac{My}{EI} \tag{3.2}$$

The Euler-Bernoulli bending theory in the form given in equation 3.1 is only applicable for symmetric beams that are sufficiently slender (i.e.: have a slenderness ratio greater than 10). For the reference specimen geometry, the symmetric section requirement is met; however, depending on the precise dimensions of the beam, the slenderness ratio may not be met. This will be revisited later when discussing the numerical portion of the study.

In order to apply an equation 3.2 to a fiber of arbitrary position and orientation within a capillary, a correction for orientation must be applied. Considering a rotated coordinate frame, $y' - x'$(as illustrated in figure 3.3), the normal stresses along the y' and x' directions can be given by the plane-stress transformation equation:

$$\sigma_{x'} = \frac{\sigma_x + \sigma_y}{2} + \frac{\sigma_x - \sigma_y}{2} cos(2\theta) + \tau_{xy} sin(2\theta) \tag{3.3}$$

$$\sigma_{y'} = \frac{\sigma_x + \sigma_y}{2} - \frac{\sigma_x - \sigma_y}{2} cos(2\theta) - \tau_{xy} sin(2\theta) \tag{3.4}$$

For the four-point bending specimen, the normal stress in the y direction σ_y was zero. The loading is directly applied on the substrate structure, which is the specimen. The substrate structure and adhesive resins have different stiffness. Therefore, the shear stress exists in the adhesive resins within the capillary. Thus, the stress transformation of 3.3 and 3.4 can be simplified to the following equation:

$$\sigma_{x'} = \frac{\sigma_x}{2}(1 + cos(2\theta)) = \frac{\sigma_x}{1 + tan(\theta)^2} + \tau_{yx} sin(2\theta) \tag{3.5}$$

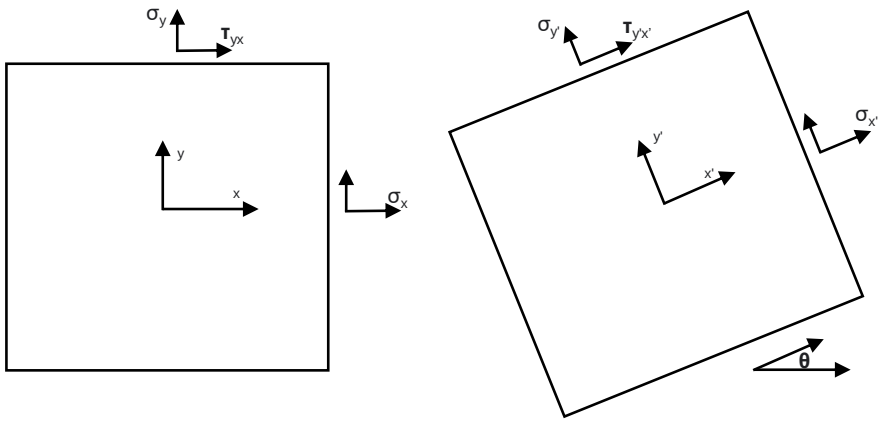

Figure 3.3: stress transformation for a plane inclined at an angle

$$\sigma_{y'} = \frac{\sigma_x}{2}(1 - cos(2\theta)) = \frac{\sigma_x tan(\theta)^2}{1 + tan(\theta)^2} + \tau_{yx} sin(2\theta) \tag{3.6}$$

Using Hooke's law and equations above, the normal strain in the x' direction can be obtained by:

$$\epsilon_{x'} = \frac{\sigma_{x'} - \upsilon\sigma_{y'}}{E} \tag{3.7}$$

$$\frac{\sigma_{x'} - \upsilon\sigma_{y'}}{E} = \frac{\sigma_x(1 - \upsilon tan(\theta)^2)}{E(1 + tan(\theta)^2)} + \frac{\tau_{yx} sin(2\theta)(1 - \upsilon)}{E} \tag{3.8}$$

$$\epsilon_{x'} = \frac{\sigma_x(1 - \upsilon tan(\theta)^2)}{E(1 + tan(\theta)^2)} = \frac{My(1 - \upsilon tan(\theta)^2)}{EI(1 + tan(\theta)^2)} + \frac{\tau_{yx} sin(2\theta)(1 - \upsilon)}{E} \tag{3.9}$$

Using this 3.9, the normal strain at an arbitrary position y and arbitrary orientation θ can be calculated for a symmetric beam subjected to pure bending.

Since the capillary size is much larger than that of the fiber, the embedded fiber can be at any location within the capillary and any orientations can also be possible as long as it is within the fiber bending limit (bending limit of the fiber used in this study is 6mm [3]). In addition, the curved fiber will take on an arc-like shape, depending on the degree of bending [4]. Figure 5.4 gives an example of the arc-like shape of a bending fiber used in this study. Therefore, the shape of the embedded fiber with curvature radius R within the capillary can be seen in figure 3.5. To investigate the influence of fiber position and orientation within the capillary, the fiber will be modeled in an arc-like shape with different curvature radius. The variable y in this figure represents the distance from the Neutral Axis of the beam to the nominal position of the fiber optic sensor (at the centerline of the capillary).

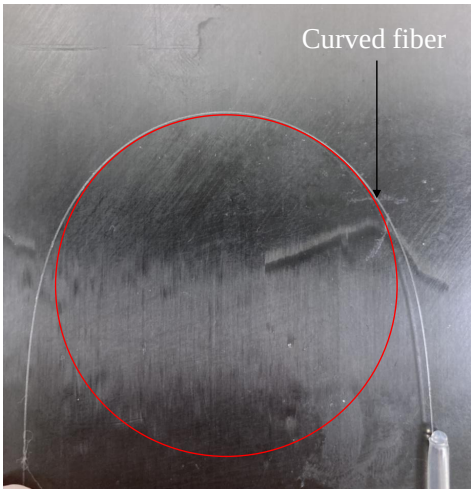

Figure 3.4: Arc-like shape of a curved fiber

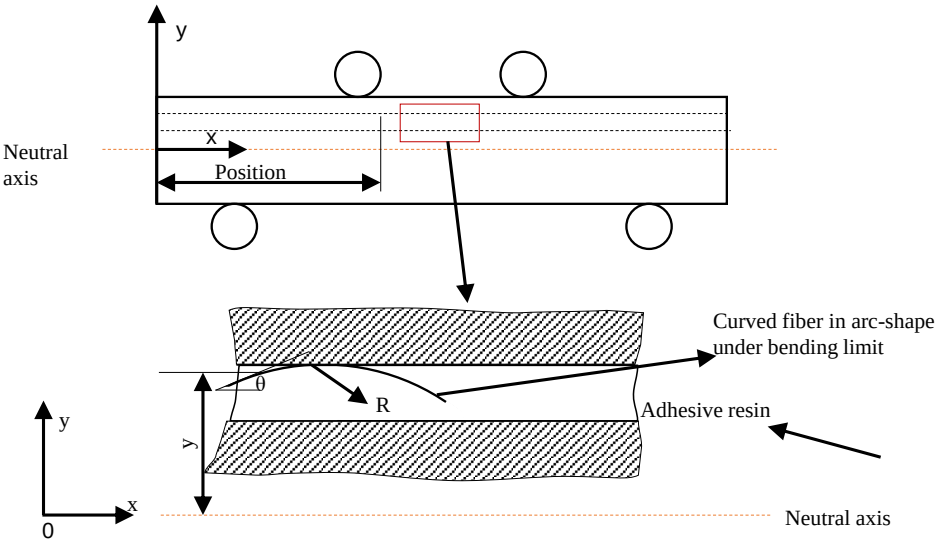

Figure 3.5: Arc-like shape of a curved fiber within the capillary

Table 3.1: Mechanical properties of the specimen and adhesive resin

Material	Elastic modulus(GPa)	Yield strength(MPa)	Poisson's ratio
Aluminum 6082-T651	70	270	0.33
AW106/HV953U epoxy adhesives	1.9 [5]	-	-

Using this model of the fiber location, y-position (y_{FOS}) and tangent of fiber orientation (θ_{FOS}) at any position x along the capillary can be calculated by

$$y = \sqrt{R^2 - (x - \sqrt{2R-1})^2} - R + 6 \tag{3.10}$$

$$tan\theta(x) = \frac{\sqrt{2R-1} - x}{\sqrt{R^2 - (x - \sqrt{2R-1})^2}} \tag{3.11}$$

$$sin(2\theta(x)) = \frac{2tan(\theta(x))}{1 + tan^2(\theta(x))} \tag{3.12}$$

Using equations 3.9–3.12, the expected strain can be calculated along the axis of the embedded fiber with different shapes. When using equation 3.9, one must be diligent in defining a suitable flexural rigidity term, EI_{xx}. As the capillary will be filled with adhesive in practice, the cross-section of the beam will be a bi-material system, the location of the neutral axis requires a stiffness-weighted centroidal position to be determined. As the aluminum alloy is significantly stiffer than the adhesive in the capillary, the contribution of the adhesive to the flexural rigidity can be ignored and it can be calculated for the rectangular beam section with a hole in the location of the capillary.

3.3. STRAIN DISTRIBUTION PREDICTION WITH A FINITE ELEMENT MODEL(FEM)

The specimens tested in this study have a slenderness ratio of less than 10 (defined by the gauge section of the beam), which violates the assumption in Euler–Bernoulli bending theory used in the analytical prediction model. Therefore, a numerical model was established using ABAQUS to investigate how much this violation may influence strain prediction accuracy.

3.3.1. MATERIAL MODEL

The established model includes the specimens made of Aluminium 6082-T651 alloy and adhesive resins within its capillary. The material model is linearly elastic, and the material properties can be seen in table 3.1. There are support pins defined with discrete rigid type, which is assembled with the part to simulate four-point bending.

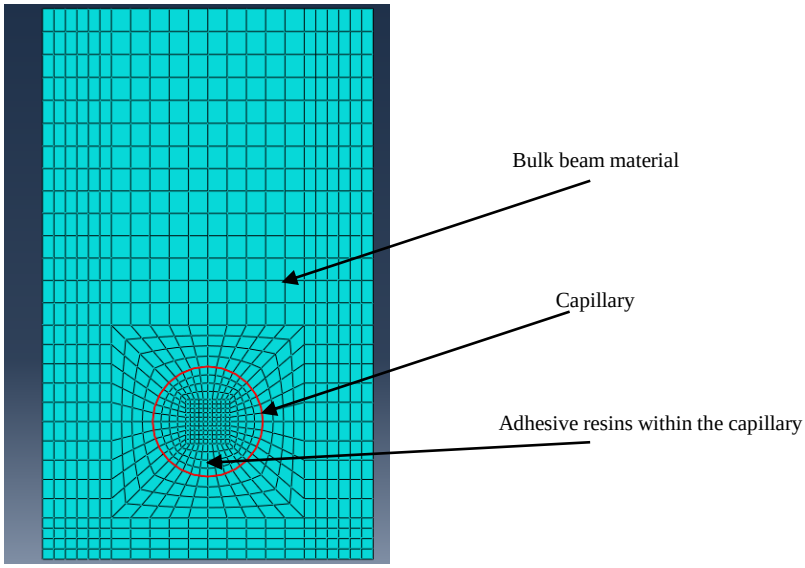

Figure 3.6: Illustration of mesh density around the interface between the adhesive resin filled capillary and bulk beam material in the FEM model

3.3.2. FINITE ELEMENT MODEL

In order to model the bonding of adhesive resin within the capillary of the specimen, a single part is divided into two pieces each of which is assigned a separate section and material mentioned above. The two pieces represent the Aluminium specimen with a capillary and the adhesive resin separately. Figure 3.6 presents mesh both inside and outside a capillary. The mesh was designed with an increasing level of refinement from the center of the capillary to the outer aluminium alloy. It can be seen that there is finer mesh around the adhesive resin and Aluminium 6082-T651 alloy interface, where strain concentration may exist due to material discontinuity. The element type is C3D8R. The smallest element is near the interface, which has a size of 0.15mm. The biggest element size is at the region far from the interface, which has a size of 0.5mm. The total number of elements in the model is 78624. The element size near the interface is determined with a convergence study and additional mesh refinement hardly affects the simulation results.

3.3.3. LOADING AND BOUNDARY CONDITIONS

The concentrated force was exercised on the upper pin supports. For boundary conditions, the lower two supports were constrained for all degrees of freedom. The upper pin supports were under displacement/rotation constraint to limit their lateral movement along X and Z directions. In addition, the movement of the central plan of the specimen along the X direction was confined. The boundary conditions can be seen in 3.7. Surface-to-surface contact in the ABAQUS is exercised between support pins and the model.

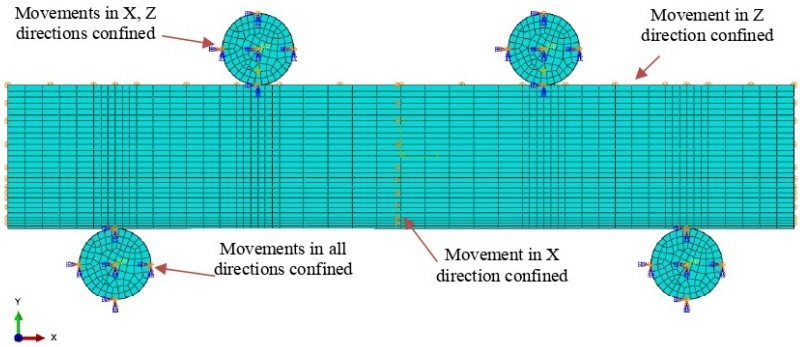

Figure 3.7: Boundary conditions for the four-point bending model

Table 3.2: Number and dimensions of all the specimens

Specimen ID	Specimen material	Capillary diameter d [mm]	Specimen length L [mm]	Specimen width b [mm]	Specimen hight h [mm]
01	Aluminum 6082-T651	2	110	12	20
02	Aluminum 6082-T651	2	110	12	20
03	Aluminum 6082-T651	4	110	12	20
04	Aluminum 6082-T651	4	110	12	20
05	Aluminum 6082-T651	6	110	12	20
06	Aluminum 6082-T651	6	110	12	20

3.4. VERIFICATION OF THE PREDICTIVE MODELS

In order to verify the predictive model, fiber optic sensors were embedded within specimens containing capillaries to measure strain and the specimens are subjected to four-point bending loading. Strain measurements from the fiber optic sensors were captured during loading and post-mortem sectioning of the specimens was performed in order to accurately characterize the location of the fiber optic sensor within the capillary at various points along the beam length. Details of the manufacturing, testing, and post-mortem sectioning of the specimens are described in the remainder of this section.

3.4.1. SPECIMEN FABRICATION

The Aluminium 6082-T651 specimens were fabricated using traditional subtractive machining processes. The use of subtractive manufacturing processes over additive manufacturing processes was chosen to avoid potential variations in the capillary and overall specimen geometry that are known to occur in metal additive manufacturing processes. Examples of each specimen type are provided in figure 3.8, details of all specimen configurations are provided in table 3.2, and the meaning of different symbols can be seen in figure 3.1.

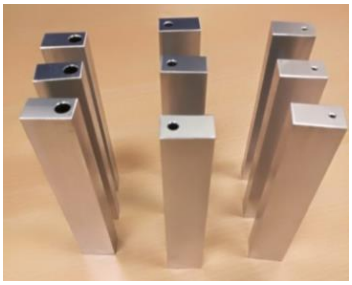

Figure 3.8: Aluminium 6082-T651 specimens with different sizes of capillaries

Table 3.3: Different test cases for the static four-point bending test.

Test case no.	Specimen ID	Specimen capillary diameter(mm)
1	01	2
2	02	2
3	03	4
4	04	4
5	05	6
6	06	6

After specimen fabrication, the following procedures were conducted to embed a fiber within the capillary of each specimen. First, a commercially-available optical fiber (LBL-1550-125, FBGS, Belgium) was placed within the specimen capillary. Second, a two-component epoxy adhesive was prepared by mixing resin of AW 106 and hardener of HV 953U by weight ratio of 5:4. Third, the fiber optic sensor was inserted into the capillary. This insertion process will be elaborated on later in this section. Finally, the prepared adhesive was injected into the capillaries slowly using a syringe. All the specimens with embedded fiber were placed into an oven for resin curing, and for Araldite 2011 this process normally takes 16 hours under the temperature of $40°C$.

3.4.2. FOUR-POINT BENDING TEST

In order to evaluate the strain measurement accuracy of the embedded fiber optic sensors, all specimens were subjected to static loading in a four-point bending setup, which can be seen from figure 3.9. The machine used is Zwick-10kN tensile/compression machine. A static loading level of 8kN was exercised on the Aluminium 6082 specimen quasi-statically. Different test cases can be seen in the table 3.3. During the four-point bending test, the fiber optic sensors are interrogated by the LUNA ODISI-B system to measure the strain distribution which will be compared with both analytical and numerical results.

3.4.3. SPECIMEN SECTIONING

The fiber embedding process used in this study could not ensure an accurate fiber location within the capillary. As a result, after testing of the specimens was completed, they were sectioned at various positions along the length of the specimen in order to assess the precise location of the fiber optic sensor within the capillary. Sections of the

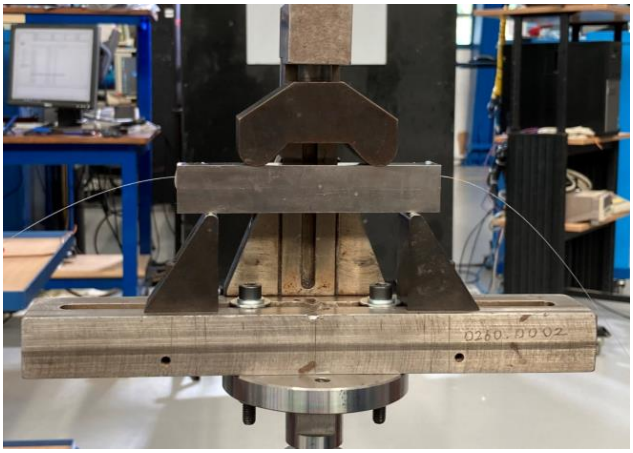

Figure 3.9: Experimental setup of a four-point bending test on Aluminium 6082-T651 specimens

specimens were observed with the laser microscope, which contained built-in software that could be used to precisely measure the location of the fiber optic sensor within the capillary.

3.5. RESULTS

3.5.1. ANALYTICAL MODEL RESULTS

Figure 3.10 and figure 3.11present strain distributions along a straight fiber within a capillary when capillary diameters, fiber positions, and orientations are different, which are predicted with the analytical model described in section 3.2. The predicted strain distributions are negative due to the fact that the strain is the compressive strain. Figure 3.10 illustrates the strain distribution prediction along a straight fiber at the capillary center when the capillary diameter varies from 2mm to 6mm. Figure 3.11 shows the strain along the capillary upper and lower boundary which make up a strain window when the capillary diameters are 2mm and 4mm. The size of the strain window depends on the capillary diameters, and the strain window size increases as the capillary diameter increases from 2mm to 4mm.

3.5.2. NUMERICAL RESULTS

Figure 3.12 presents the prediction of strain distribution over the specimen under four-point bending from the numerical model and figure 3.13 represents strain distributions along the capillary centers when capillary diameters are 2mm, 4mm, and 6mm respectively.

3.5.3. CROSS SECTIONS OF THE CAPILLARY WITH EMBEDDED FIBER

Cross section of a 2mm-diameter capillary with straight fibers in the Aluminium 6082 specimen can be observed using Keyence Laser Scanning Confocal Microscope (DASML,

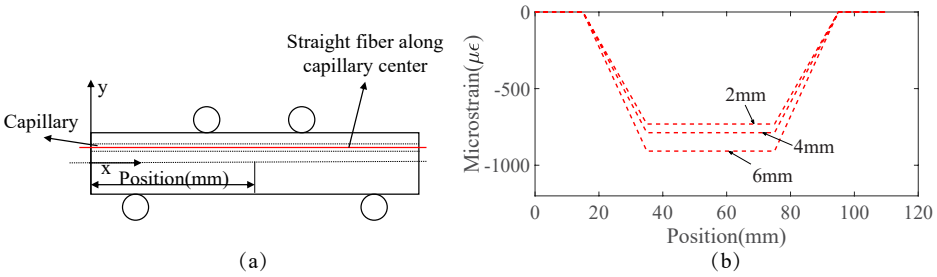

Figure 3.10: (**a**) Schematic representation of an embedded fiber which is straight and at the capillary center (**b**) Analytically predicted strain distribution along the capillary center when the capillary diameters are 2mm, 4mm, and 6mm respectively for Aluminium6082 under a loading of 8kN

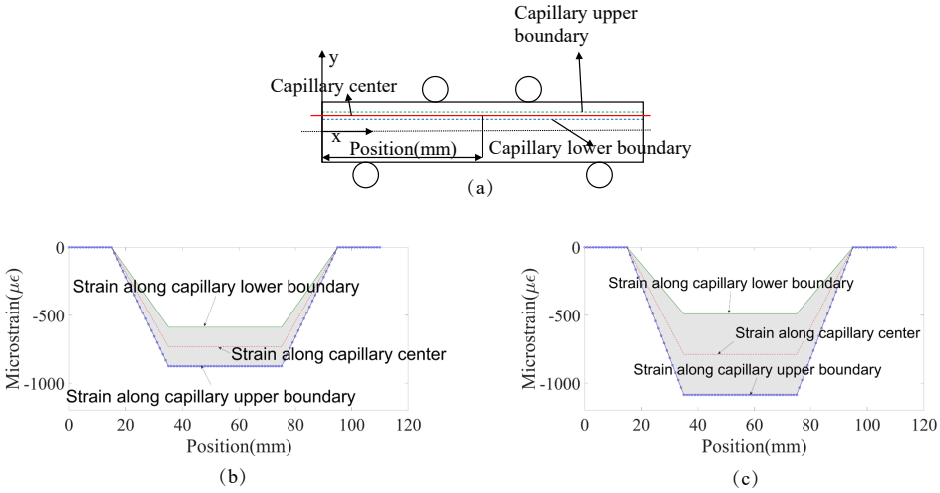

Figure 3.11: (**a**) Capillary upper boundary, capillary center, and capillary lower boundary in the specimen under four-point bending; Analytically predicted strain distribution, which is along the straight fiber at the capillary center, upper boundary, and lower boundary when capillary diameters are (**b**) 2 mm and (**c**) 4mm in Aluminium 6082 specimens under a loading of 8KN.

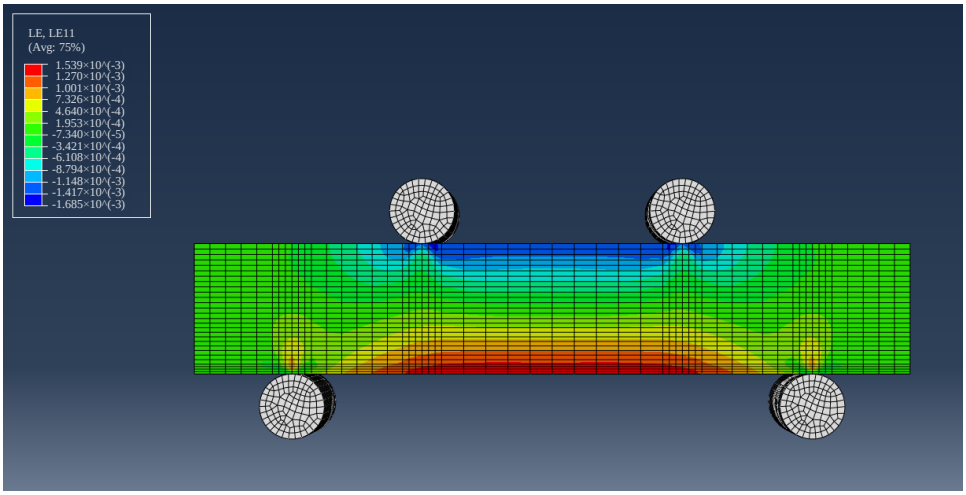

Figure 3.12: Numerically predicted strain distribution over the specimen under four-point bending

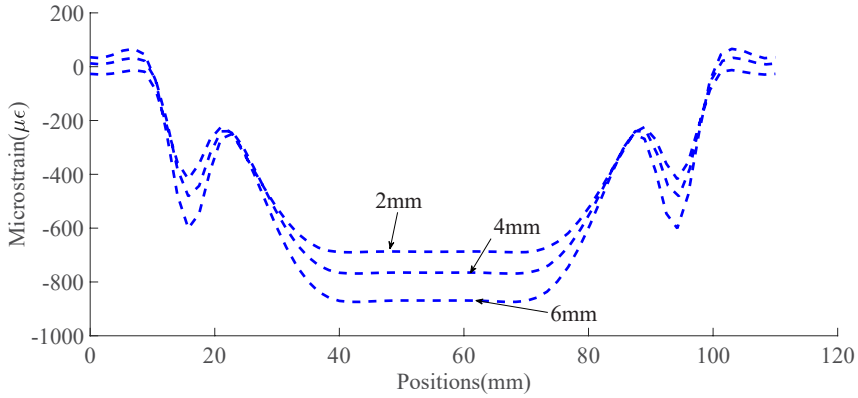

Figure 3.13: Simulated strain distribution along capillary centers when capillary diameters are 2mm, 4mm, and 6mm respectively under the 8kN loading

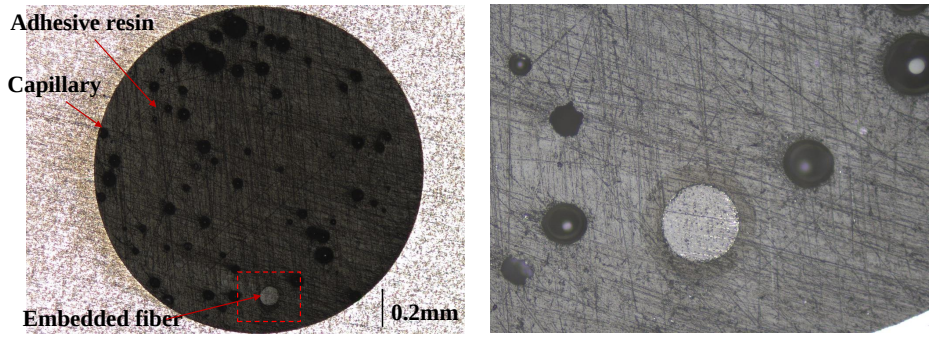

Figure 3.14: (**a**) Cross section of specimen 01 with the embedded fiber; (**b**) Magnification of the region with embedded fiber

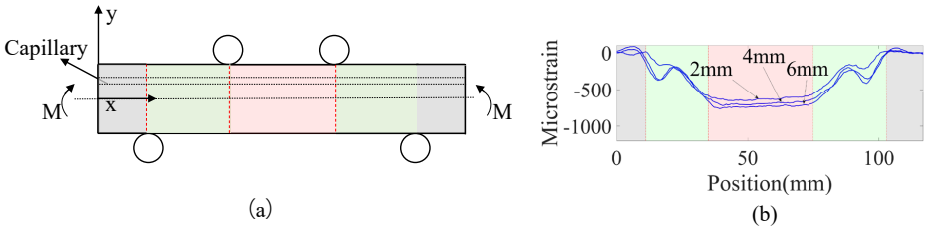

Figure 3.15: Strain distribution measured by fiber optic sensors embedded within Specimen 01, 03, and 05 with capillaries of diameters 2mm, 4mm, and 6mm respectively, under the 8KN loading under four-point bending static test

Tudelft, Netherlands) , which is presented in figure 3.14. The fiber was placed along the capillary center before injecting adhesives as described in 3.4.1, and however, it can be seen that the embedded fiber deviates from center of the capillary after the fiber embedding. The deviation of the fiber from the capillary center can be used to predict the strain at the fiber's real location.

3.5.4. FOUR-POINT BENDING TEST RESULTS OF AL6082-T651

Figure 3.15 presents the strain distribution measured by fiber optic sensors embedded within Specimen 01, 03, and 05 with capillaries of diameters 2mm, 4mm, and 6mm respectively, under the 8kN loading under four-point bending static test. It can be seen the red region has a constant bending moment, which is of interest because the influence of fiber locations and orientations can be highlighted and the influence of bending moment does not need to be considered in this region. The strain peaks in the green region are induced by the concentrated load from the loading pins in the four-point bending test.

3.6. DISCUSSION

3.6.1. COMPARISON OF THE ANALYTICALLY PREDICTED STRAIN, NUMERICALLY PREDICTED STRAIN AND MEASURED STRAIN

Figure 3.16 show the comparison of the analytically predicted and numerically predicted strain distribution along the capillary center in the region with a constant bending moment for specimens under the loading of 8kN. Figure 3.17 compares strain measurement along with fiber embedded in the region marked red, and analytical strain predictions at the real fiber location when capillary diameters of Al6082 specimens are 2mm, 4mm, and 6mm. It can be seen that the updated strain prediction with the real location of the fiber is very close to the measured strain. The difference between them is similar to the intrinsic measurement noise. The measurement noise is determined by analyzing the measured strain distribution when there is not any load on the specimen, and the measurement noise is between $\pm 10\mu\epsilon$ in the ambient environment of DASML at Tudelft. In the analytical model, the capillary with embedded fiber is directly modeled as an empty hole with zero stiffness, and the capillary in the numerical model is modeled as a capillary with adhesive resins. Due to the stiffness of the adhesive resins being much smaller than the substrate alloy and close to 0, therefore two models are very similar in terms of modeling the capillary. In addition to that the three basic assumptions of the euler-bernoulli beam theory are met. All of that can explain the small differences between the results from the analytical model and the numerical model.

Comparison of the analytical, numerical, and test results show that violation of the analytical model assumption doesn't have an influence on the prediction accuracy of the analytical model. Therefore its results will be further utilized to investigate the influence of fiber orientation and positions on strain distributions. Since it is much easier to plot the axial strain along fiber length when the fiber is wavy with the analytical model compared with the numerical model, the analytical model is necessary for investigating the influence of fiber orientations on measured strain distributions. In addition, the results of the numerical model will also be used in establishing the analytical model as shown in the subsequent section.

3.6.2. INFLUENCE OF FIBER POSITION AND ORIENTATION VARIATIONS ON STRAIN MEASURE ACCURACY

When an optical fiber is embedded within a specimen using capillaries, fiber positions with respect to the specimen centroid and fiber orientations may vary along the fiber. It is interesting to know whether both factors influence strain measurement, and how much their influences are. Analytical strain distribution along the fiber can be predicted using equation 3.9. The right side of the equation indicates the influence of fiber orientation on strain measurement. When an optical fiber is embedded in curved fiber with different arc-like shapes, the strain distributions as the function of fiber positions alone, and both fiber positions and orientations are compared in 3.18. It can be seen when the fiber is curved to its limit of 6mm radius, the fiber orientations have an impact on the strain distribution. The maximum difference of strain distribution when considering the fiber position relative neutral axis y and fiber orientation θ due to fiber bending is $90\mu\epsilon$ under 4KN and $140\mu\epsilon$ under 6KN. That is much greater than the measurement noise of

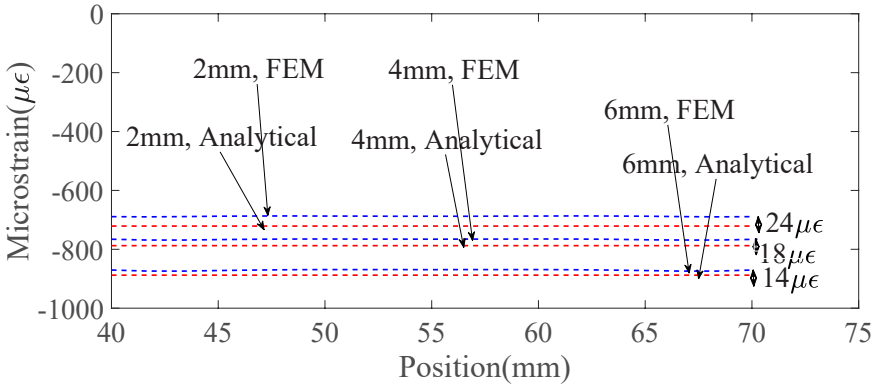

Figure 3.16: Comparison of the analytically predicted and numerically predicted strain distribution along the capillary center in the region with a constant bending moment under the loading of 8KN

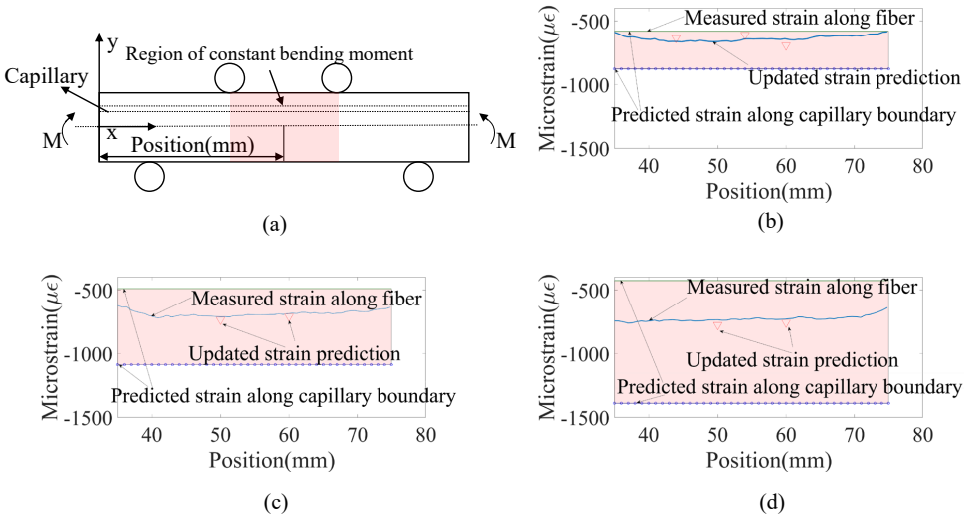

Figure 3.17: (**a**) Part of the capillary where bending moment is constant and is marked in red; Comparison of strain measurement along with fiber embedded in the region marked red, and analytical strain predictions at the real fiber location when capillary diameters of Al6082 specimens are (**b**) 2mm, (**c**) 4mm and (**d**) 6mm

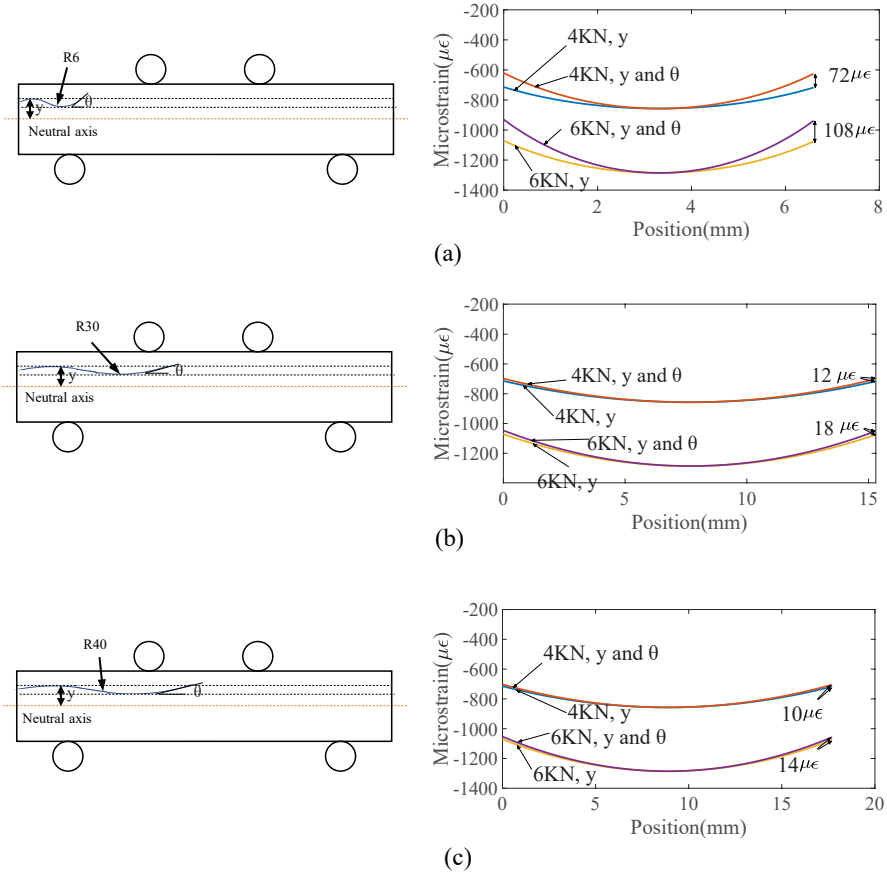

Figure 3.18: Comparison of analytically predicted strain along curved fiber when only fiber orientation θ and fiber position relative to neutral axis y are considered and θ alone are considered for curved fibers with a curvature radius of (**a**) 6mm, (**b**) 30mm, and (**c**) 40mm respectively as shown in the left

around $20\mu\epsilon$. However, it is very rare to achieve this kind of waviness when embedding a fiber. As the fiber gets less wavy, the difference decreases significantly. For example, when the fiber is in the arc-like shape with 30mm, the maximum difference drops to $17\mu\epsilon$, which is very close to the measurement noise. Therefore, when embedding a fiber, in general, the fiber position relative to the neutral axis y has a much larger influence than the fiber orientation. The fiber orientation's influence will not be considered when using the measured strain for crack detection.

3.6.3. RELATIVE MEASUREMENT ERROR ASSOCIATED WITH CAPILLARY

When assuming the nominal strain distribution is the strain along the capillary center, variations of fiber positions within the capillary lead to deviations of the measured strain from the nominal strain. The deviation can be quantified by relative measurement errors

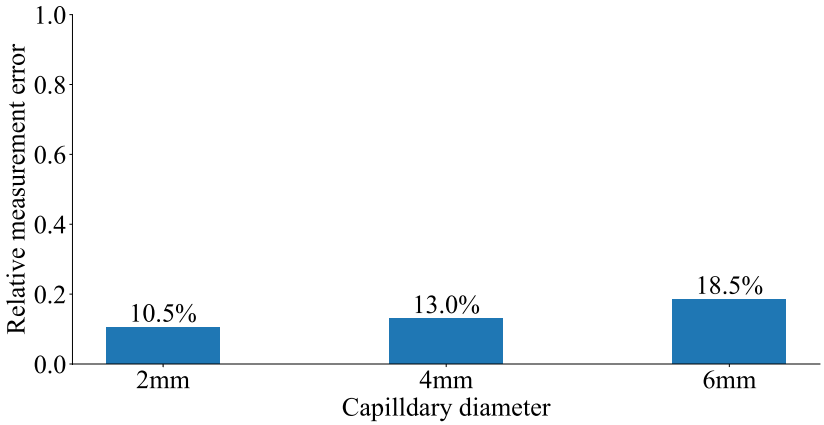

Figure 3.19: Measurement error of fibers embedded in capillaries of different diameters

(RME) which can is defined by the following equation.

$$RME = \frac{|\epsilon_{upper} - \epsilon_{lower}|}{2\epsilon_{center}}, \tag{3.13}$$

Where the ϵ_{upper}, ϵ_{lower}, and ϵ_{center} represent the strain value along the capillary upper boundary, lower boundary, and center. The strain measurements of a straight fiber deviate most from nominal strain when the fibers are at capillary boundaries, and corresponding RME are the highest. Therefore, the capillary diameter has an influence on the relative measurement error of the embedded fiber. Figure 3.19 represents the relative measurement error for specimen capillaries, and it can be seen that as the capillary diameter increases, the fiber measurement error increases. That indicates that fiber measurement accuracy decreases as capillary diameter grows. Theoretically, the capillary diameter should be as small as possible in order to reduce relative measurement error. However, reducing capillary diameter also increases the difficulty of embedding fiber into the capillary because the adhesive resin should be injected into the capillary. Therefore, one should be careful when choosing the capillary size and balance the ease of embedding with measurement accuracy. In this study, the specimen with a capillary of 2mm will be used for experiments in the next chapter.

3.7. CONCLUSION

When an optical fiber is embedded within a specimen using capillaries, both fiber positions and orientations may vary along the fiber. An analytical model is established to investigate the influence of fiber positions and variation change on strain distribution. The model is also verified by the four-point bending static test. Based on the results of the analytical model and static four-point bending test, the following conclusions can be made.

1. When an optical fiber is embedded within a specimen using capillaries, both fiber positions and orientations may vary along the fiber. Variation of fiber orientations has negligible influence on strain measurement compared with fiber position variations. Therefore, fiber position uncertainty is the main factor influencing strain measurement accuracy.

2. The positional uncertainties of the embedded fiber within capillaries can cause strain measurement uncertainties, and the measured strain distributions lie within the strain windows defined by the strain distribution along the capillary boundary when there is no crack in the specimen. Therefore it is possible to perform crack detection using the strain window.

BIBLIOGRAPHY

[1] M. Strantza, "Additive manufacturing as a tool for structural health monitoring of metallic structures", Ph.D. dissertation, Vrije Universiteit Brussel Brussels, Belgium, 2016.

[2] O. A. Bauchau and J. I. Craig, "Euler-bernoulli beam theory", *Structural analysis*, pp. 173–221, 2009.

[3] *What is the minimum bend radius of the fiber?*, Apr. 2020. [Online]. Available: https://fbgs.com/faq/what-is-the-minimum-bend-radius-of-the-fiber/.

[4] A. J. Y. Tan, S. M. Ng, P. R. Stoddart, and H. S. Chua, "Theoretical model and design considerations of u-shaped fiber optic sensors: A review", *IEEE Sensors Journal*, vol. 20, no. 24, pp. 14 578–14 589, 2020.

[5] HUNTSMAN, *Araldite aw 106 / hardener hv 953 u*, Accessed: 5-3-2020.

4

INVESTIGATING THE STRAIN EXCEEDANCE METHOD FOR CRACK DETECTION WITH EMBEDDED FIBER OPTIC SENSOR

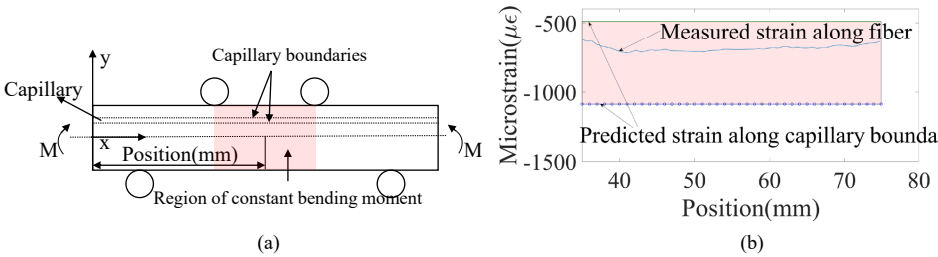

Figure 4.1: (**a**) The constant bending moment region of the specimen; (**b**) The strain window consists of strain distribution prediction along capillary boundaries under 8KN, with the measured strain lying within the strain window

4.1. INTRODUCTION

THE previous chapter details the fiber embedding process and studies the positional accuracy of embedded fiber optic sensors and the influence on strain measurement accuracies. When a fiber optic sensor embedded within a specimen capillary is under constant loading, there is uncertainty of fiber positions within the capillary due to the fact that the diameter of the capillary (2mm) is much larger than that of an optical fiber (195 µm [1]). A strain window can be defined with the strain distribution along the capillary boundary, as shown in figure 4.1. When there is no crack in the specimen as shown in the figure, the strain distribution measured with the fiber optic sensor could lie anywhere within the strain window, due to the uncertainty of fiber position within the capillary. The strain distribution uncertainty leads to a challenge in crack detection with the measured strain distribution under constant loading. However, when there is a crack initiating and propagating within the specimen, measured strain distribution could grow and possibly exceed the strain window. As a result, the crack could be detected by monitoring any strain exceedance. The crack detection method is named the strain exceedance method in this study. This chapter aims to answer the following question: how effective is the strain exceedance method for detecting cracks in the selectively laser melted (SLM) specimens? In order to answer the question, this chapter has been organized in the following way. First, the analytical model established in section 3.2 was modified to predict the strain distributions along the capillary edges using the Euler-Bernoulli beam theory. Second, four-point bending fatigue tests were performed on the SLM specimens, with embedded fiber optic sensors measuring in situ strain. The measured strain was compared with the strain window to determine if there was any crack in the specimen. Length of the crack when there is any strain exceedance can be determined with a camera.

4.2. STRUCTURAL CASE STUDY: FOUR-POINT BENDING FATIGUE TEST

When using the strain exceedance method to perform crack detection, even though the strain distribution may change due to crack propagation, there is a risk that the mea-

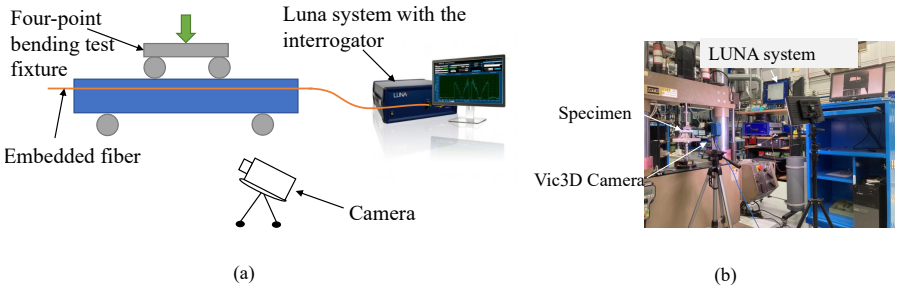

Figure 4.2: (**a**) Schematic test setup of a four-point bending fatigue test on specimens; (**b**) Real test setup of a four-point bending fatigue test on specimens

sured strain distribution fails to exceed the pre-set strain window before the final failure of the specimens. In order to evaluate the effectiveness of the strain exceedance criteria for crack detection, four-point bending fatigue tests were performed on the specimens containing embedded fiber optic sensors. The initiation and growth of a fatigue crack from a predefined notch were monitored with an optical camera to provide a visual indication of the presence and length of the fatigue crack. The strain distributions corresponding to different observed crack lengths could be measured with the embedded fiber optic sensor and then be compared with the strain window along the capillary boundaries to determine when the measured strain distributions exceed the strain window.

4.2.1. TEST SETUP

Figure 4.2 represents schematic representations of the four-point bending fatigue test setup and the real test setup. As can be seen in the figure, the four-point bending fatigue test setup includes an MTS servo-hydraulic test frame, Luna ODISI-B interrogator (LUNAINC, VA 24011), and VIC3D camara.

4.2.2. NOMINAL SPECIMEN GEOMETRY

The nominal geometry of the SLM specimen can be seen in 4.3. To ensure a reliable and fair comparison of the proposed method with the vacuum sensor based method for crack detection in SLM specimen prposed by Strantza [2], the specimen in this study has the same nominal geometry as Strantza's study. However, there may be geometry and size inaccuracy due to reasons such as imperfect scanning strategy and thermal gradients in the SLM specimens [3]. The designed length, width, and height of SLM specimens are bigger than nominal geometries, then the SLM specimens are machined to the nominal geometries. One exception is the capillary. The capillary in the SLM specimen is kept in its as-built state to take advantage of the most freedom with respect to the path a capillary can take by means of additive manufacturing. In addition, leaving the capillary in its as-built state in this study help to understand how the additively manufactured capillary would influence performance of the strain exceedance based crack detection method.

Figure 4.3: Norminal geometry of specimens used in four-point bending fatigue test

Besides the SLM specimens, the four-point bending fatigue test will also be performed on traditional specimens.

4.2.3. SPECIMEN MANUFACTURING

TRADITIONALLY MACHINED SPECIMEN

The traditionally machined specimens are specimens made of Aluminium 6082-T651 material. They were fabricated using the same traditional subtractive machining processes as in chapter 3 to the nominal geometries shown in figure 4.3. A v-shape notch is created on the bottom of every specimen with electric discharge machining with a Funac wire EDM machine for crack initiation. There are totally 4 traditionally machined specimens, which are named tm1, tm2, tm3, and tm4

ADDITIVELY MANUFACTURED SPECIMEN

In addition to the traditionally machined specimen, there are also SLM AlSi10Mg specimens. The SLM specimens were made by K3D B.V. (Eindhoven, Netherlands) with a layer thickness of 0.33mm and laser spot size of 0.11mm. The SLM specimens later went through surface treatment to reduce residual stress and pores. As mentioned before the SLM specimens have design geometries larger than nominal geometries in 4.2.2, and then they were machined to the nominal geometries except for the capillary. There are 4 additively manufactured specimens named am1, am2, am3, and am4.

As mentioned above, the capillaries of SLM specimens are in their as-built state. However, the capillary size may not be exactly the same as the nominal geometry. In order to observe the real shape of the capillary in specimens, both the additively manufactured and traditionally machined specimens are cut after the fatigue test. The cross-sections of the specimens are observed with the Keyence Laser Scanning Confocal Microscope. which can be seen in 4.5.

4.2.4. EXPERIMENT PROCESS

There are 4 specimens manufactured from the additive manufacturing process and 4 specimens made from the traditional machining process. For both the traditionally machined and additively manufactured parts, fiber optic sensors were be embedded within the specimens after manufacturing with the method described in section 3.4.1.

In order to measure the strain distribution as the crack propagates within a specimen, four-point bending fatigue tests were performed on MTS servo-hydraulic test frame in

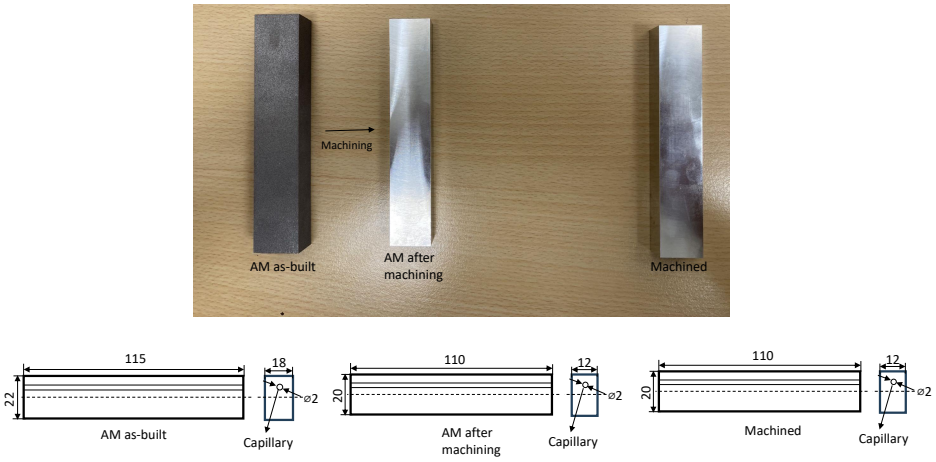

Figure 4.4: The traditionally machined Aluminium 6082-T651 specimens and additively manufactures AlSi10Mg specimens

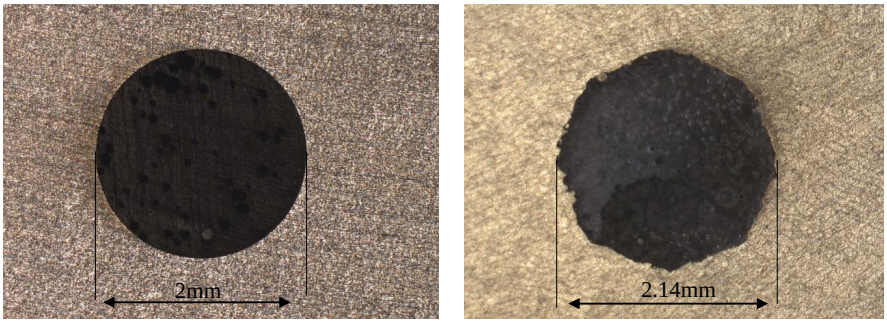

(a) (b)

Figure 4.5: (**a**) Cross section of a traditional specimen tm1; (**b**) Cross section of a SLM specimen am1

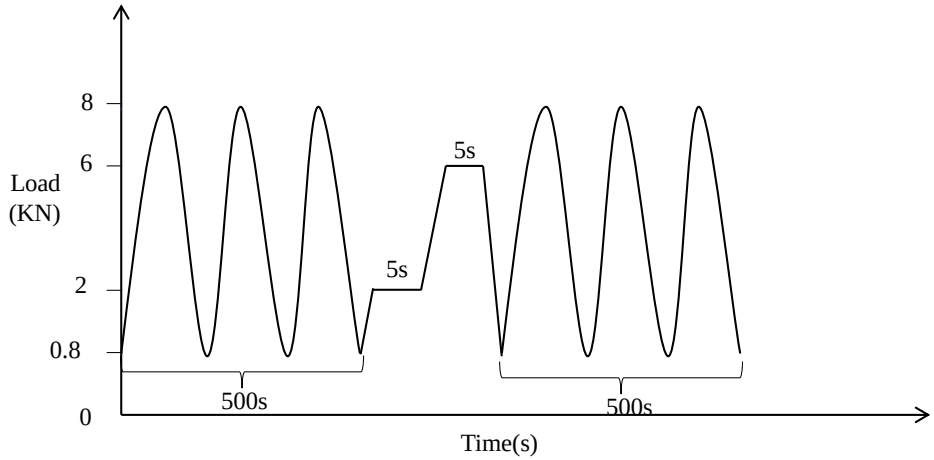

Figure 4.6: Change of loading with time during the four-point bending test

DASML (Delft, Netherlands) equipped with a 10KN load cell, as shown in figure 4.2. A camera car was set up near the fatigue machine to capture the initiation and propagation of the crack. The camera car received signals from the MTS fatigue machine and took an image every 500s. As the crack growed, strain distribution was also measured with the LUNA system every 500s. Before determining loading levels, crack growth curves were established to predict the estimated cycles needed for the crack to grow to a certain crack length under different loading levels. The prediction can provide a reference of the employed load for the fatigue test and kept the fatigue test from lasting too much time.

Based on the predicted fatigue growth curve under different loading levels, a maximum force of 8KN and a stress ratio of 0.1 is used for the fatigue test with a loading frequency of 8HZ. Two loading levels of 6kN and 2kN are used for measuring the strain distributions. The two loading levels are used to highlight differences of measured strain distributions measured under high and low loading levels. A schematic representation of the loading profile change can be seen in 4.6, which includes repeated sinusoidal loading block, loading and unloading ramps, and constant loading. During the constant loading, the strain will be measured with the distributed fiber optic sensors.

As shown in figure 4.7, there is the pre-manufactured notch on the specimen bottom to accelerate crack initiation and crack length is regarded as the total length of the notch and crack initiating around the notch tip. Therefore the initial crack length is 2mm.

4.3. STRAIN EXCEEDANCE METHOD FOR CRACK DETECTION WITH ANALYTICAL MODEL

The strain exceedance method for crack detection requires comparing the strain distribution measured by the embedded fiber optic sensors with the strain window, which are predicted strain distributions along the capillary edges. The model created in section

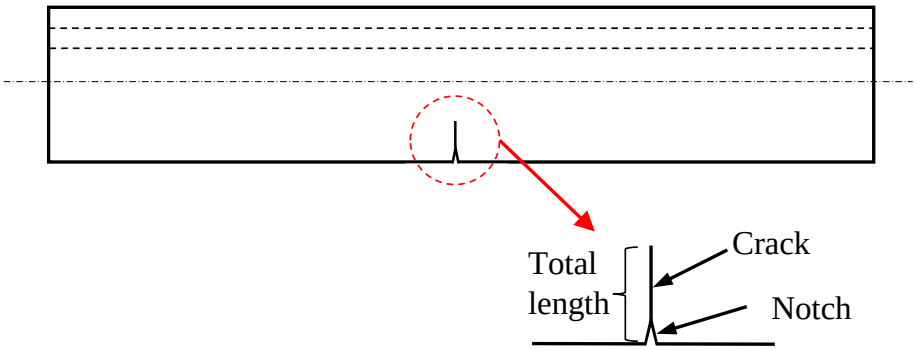

Figure 4.7: The pre-manufactured notched before fatigue test, the crack initiated from the notch during the test, and the total length of both crack and notch

Table 4.1: 8 test case for the four-point bending fatigue test

Specimen ID	Specimen manufacturing process	Test case no.	Load(KN) when measuring strain
tm1	subtractive manufacturing	01	2 & 6
tm2	subtractive manufacturing	02	2 & 6
tm3	subtractive manufacturing	03	2 & 6
tm4	subtractive manufacturing	04	2 & 6
am1	selective laser melting	05	2 & 6
am2	selective laser melting	06	2 & 6
am3	selective laser melting	07	2 & 6
am4	selective laser melting	08	2 & 6

3.2 can be used to predict the strain window. The normal stress due to bending can be described using the Euler-Bernoulli beam theory.

$$\sigma_z = \frac{My}{I_{xx}} \tag{4.1}$$

Where M is the bending moment, y is the distance from the neutral axis, and I_{xx} is the moment of inertia around the neutral axis. As this section of the specimen is under pure bending loading, there are no other stress components, allowing the normal strain, to be calculated simply by dividing the stress by the Young's Modulus, E:

$$\varepsilon_z = \frac{\sigma_z}{E} = \frac{My}{EI_{xx}} \tag{4.2}$$

The main deviation is the change of capillary shape in additive manufactured parts. As can be seen in the figure 4.5, the cross-section of capillary in the SLM specimen am1 was different from its original design due to its rough surface finish. The change in capillary cross-section can influence the moment of inertia needed for the analytical model. In the ideal case when the capillary has a circular cross-section of diameter d, the moment of inertia around the neutral axis I_{xx} can be shown in the equation 4.3

$$I = \frac{bh^3}{12} - \frac{\pi d^4}{64} \tag{4.3}$$

In considering the application of this model to an SLM specimen, it could be important to take into account the real geometry of the capillary. The real capillary diameter d may not be the same as the nominal capillary diameter.

When an optical fiber is embedded within a specimen using capillaries, both fiber positions and orientations may vary along the fiber. Based on the investigations completed in chapter 3, it was found that the orientation of the fiber within a capillary had a negligible influence on the strain measurement relative to its absolute position. Therefore, only the fiber position's influence on strain distribution is considered.

4.4. FINITE ELEMENT MODELLING

To address the issues identified in chapter 3 regarding the suitability of Euler-Bernoulli equation to the beam specimen which has a slenderness ratio of less than 10 in this study, several crack lengths were simulated with the same FEM model as in the one established section 3.3. The only exceptions are the inclusion of a crack in the FEM model. An initial crack is simulated by introducing a discontinuity in the geometry. The mesh density is an important issue that can influence the accuracy of an FEM model, and at the same time, it also determines the FEM model's complexity level. As can be seen in 4.8, the model uses dense mesh in the area around the crack, and relatively sparse mesh around the crack, and therefore the accuracy of the model can be improved without significantly increasing model complexity. The mesh size is determined with a mesh sensitivity study.

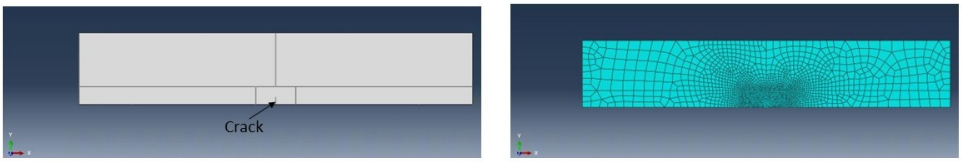

Figure 4.8: The dense mesh close to the crack and relatively sparse mesh in the other area of the FEM model

4.5. RESULTS

4.5.1. STRAIN READING FROM FATIGUE TESTS

With a strain measurement frequency of 10HZ, 100 measured strain distributions are performed in the duration of 10s under a load of 2KN and 6KN, which can be seen in figure 4.6, and there are 100 measured strain distributions every 500s. Therefore for every observed crack length, there are 50 independent strain distribution measurements under the load of both 2KN and 6KN.

There is intrinsic measurement noise of the fiber optic sensor. In order to remove the measurement noise, all the strain measurements are averaged. Figure 4.9 represents a single strain distribution measurement with the embedded fiber optic sensor in a specimen tm1 when the crack length is 5mm and loading is 2KN in the left, and 50 strain distribution measurements within a period of 5s and the average of all the strain distribution measurements in the left figure.

It can be seen that calculating the average of 50 independent strain measurements can effectively remove the measurement noise. Therefore, the strain distribution corresponding to every combination of crack length and load will be denoised in the same way.

Figure 4.10 represent the strain distributions measured by embedded fiber optic sensor as the crack propagates in a traditionally machined specimen tm1 and SLM specimen am1 under 2kN and 6kN. When the loading is 2kN for specimen am1, the maximum strain near the crack increases as the crack length grows from 2mm to 5mm and increases to -207$\mu\varepsilon$ as the crack length grows to 7mm. As the crack length grows to 10mm, the strain increases significantly to around -310$\mu\varepsilon$. Then the specimen breaks. When the loading is 6kN, a similar strain increase can be observed as the crack grows from 2mm and 10mm, and the maximum strain near the crack is about -750$\mu\varepsilon$. After that the specimen breaks.

When the loading is 2kN for specimen am1, it can be seen that the maximum strain grows as the crack length increases from 2mm to 9mm, and the maximum strain near the crack is around -265$\mu\varepsilon$. After that, the specimen breaks. As the crack grows from 9mm to 12mm, the maximum strain decreases from -314$\mu\varepsilon$ to -260$\mu\varepsilon$. When the loading is 6KN, it can be seen that the maximum strain increases as crack length increases from 2mm to 9mm, after that the maximum strain decreases from around -714$\mu\varepsilon$ to around -690$\mu\varepsilon$ as the crack grows from 9mm to 12mm, and after that the specimen breaks. The

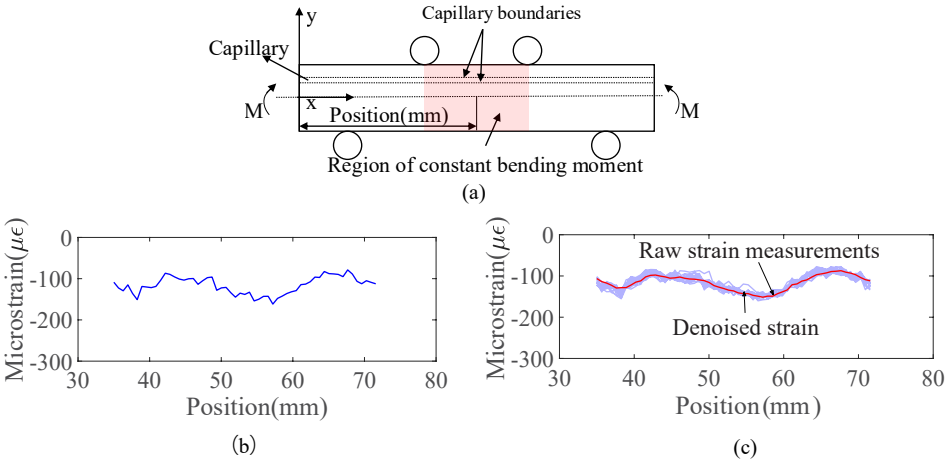

Figure 4.9: (**a**) The constant bending moment region where the measured strain distribution is plotted; (**b**) A single strain distribution measured with the embedded fiber optic sensor, when the crack length is 5mm and loading is 2KN from experiment case 01 in table 4.1; (**c**) 50 raw strain distribution measurements within a period of 5s when the crack length is 5mm and loading is 2KN from experiment case 01 and the denoised strain distribution after averaging all the strain distribution measurements

reason for the strain decrease is that as the crack grows, the neutral axis is also shifting toward the embedded fiber and the strain decrease due to the smaller distance between the neutral axis and embedded fiber is more significant than the strain increase induced by the crack growth.

4.5.2. STRAIN WINDOW

Figure 4.11 represents the strain window consisting of analytical strain prediction along capillary boundaries in the traditional specimen tm1 and SLM specimen am1 under 2KN and 6KN. Because the capillary size of the SLM specimen am1 is slightly larger than that of the traditional specimen am1 as shown in figure 4.5, the strain window for the SLM specimen am1 is also larger than that of the traditional specimen tm1. Under 2KN, the strain window for traditional specimen tm1 includes an upper boundary of -116$\mu\varepsilon$ and a lower boundary of -218.9$\mu\varepsilon$. The strain window for SLM specimen am1 consists of an upper boundary of -110$\mu\varepsilon$ and a lower boundary of -243$\mu\varepsilon$. Under 6KN, the strain window for traditional specimen tm1 includes an upper boundary of -410$\mu\varepsilon$ and a lower boundary of -656$\mu\varepsilon$. The strain window for SLM specimen am1 consists of an upper boundary of -393$\mu\varepsilon$ and a lower boundary of -684$\mu\varepsilon$.

4.6. DISCUSSION

This study aims to study the feasibility of detecting fatigue cracks using the strain exceedance method. The rationale behind the method is that the measured strain lies within a strain window defined by nominal strain distributions along capillary edges

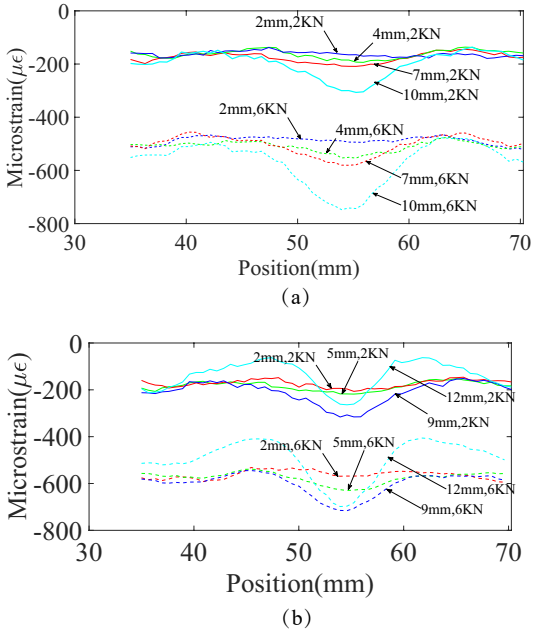

Figure 4.10: (**a**) Measured strain distribution under four-point bending fatigue test as crack length increases under 2KN and 6KN for the traditionally machined specimen in test case 01; (**b**) Measured strain distribution under four-point bending fatigue test as crack length increases under 2KN and 6KN for the selected laser melted specimen in test case 05

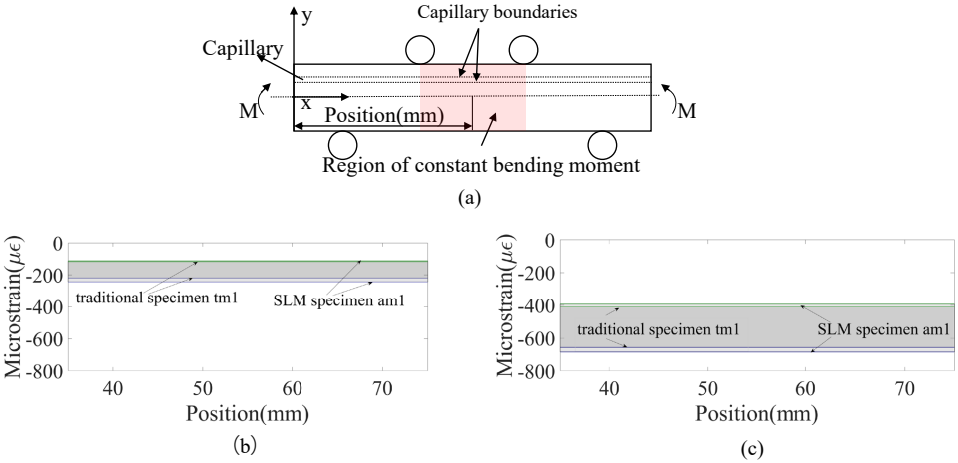

Figure 4.11: (**a**) the capillary boundaries in the constant bending moment region (**b**) the strain window consisting of analytical strain prediction along capillary boundaries in the specimen tm1 and am1 under 2KN; (**c**) the strain window consisting of analytical strain prediction along capillary boundaries in the specimen tm1 and am1 under 2KN

when there are not any cracks, and any strain exceedance of the strain window otherwise indicates the existence of cracks.

4.6.1. EFFECTIVENESS OF THE STRAIN EXCEEDANCE BASED METHOD FOR CRACK DETECTION

DATA PROCESSING

As mentioned in the section 4.5.1, there is noise in the measured strain distribution with embedded fiber optic sensors. The measurement noise can be misleading when comparing the measurement with the strain window. Therefore, the strain measurement is denoised by averaging the 50 independent strain measurements for every observed crack length.

CONFIDENCE INTERVALS (CI)

In order to get rid of the influence of measurement noise, the 50 measured strain distributions are averaged, and a 95% confidence interval (CI) of the real strain is created using Bootstrap [4]. A CI estimates a range within which the true strain value is likely to fall based on a sample of strain data. The CI can represent the level of inherent measurement noise of the embedded fiber optic sensors.

As the crack grows, the strain distribution changes. In figure 4.12, the average strain measurement corresponding to different crack length are compared with the strain windows when the traditional specimen tm1 is under 2KN loading. The 95% CI is established for the strain near the crack tip as shown in part (a) of the figure. 95% CI fall within the two boundaries when crack lengths are 2mm and 4mm, and the CI is very close to the strain window when the crack length is 7mm. When the crack length is 10mm, the CI totally lies out of the boundaries. Figure 4.13 represents the comparison of strain measurements with the strain window under 6KN load in traditional specimen tm1. Similar to figure 4.12, the CI near the maximum strain is very close to the strain window when the crack length is 7mm, and it lies out of the strain window when the crack length grows to 10mm.

In figure 4.14, the average measured strain distribution for the SLM specimen am1 under 2KN is compared with the strain window. A 95% CI of the strain is also created where there is a crack. Similar to the traditional specimen tm1, the CI lie within the boundaries when the crack length is relatively small and it lies out of the boundary when the crack length is around 9mm.

In figure 4.15, the averaged measured strain distribution for an additively manufactured specimen under 6KN is compared with the strain window. A 95% CI of the strain is also created in the position closest to the crack tip. As the crack grows from 2mm to 9mm, the maximum strain also increases to around -730$\mu\varepsilon$. The average strain and 95% CI lie within the strain window when the crack length is 9mm. However, as the crack grows to 12mm, the strain distribution decreases

DECREASE OF STRAIN VALUE AS CRACK GROWS

As the crack grows, it can be seen that there are crack-induced strain peaks in the strain distribution measured by the embedded fiber optic sensor. It is easy to understand the

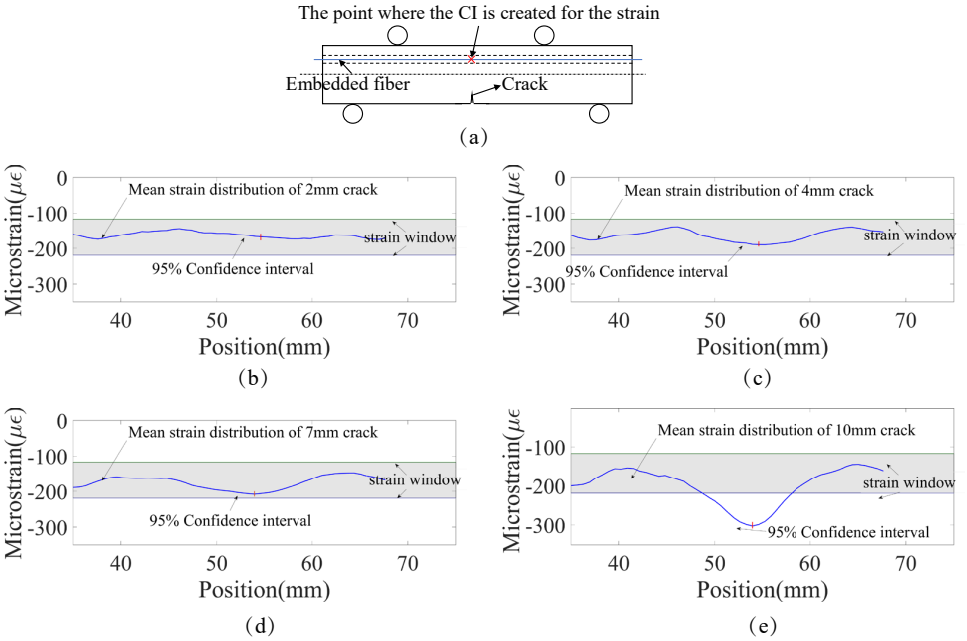

Figure 4.12: (**a**) The point where the confidence interval for the measured strain is measured; Comparison of average strain measurement, 95% confidence interval of the strain near the crack tip, strain window in the traditional specimen of test case 01 as the crack grows from (**b**) 2mm to (**c**) 4mm, (**d**) 7mm, and (**e**) 10mm under 2KN load

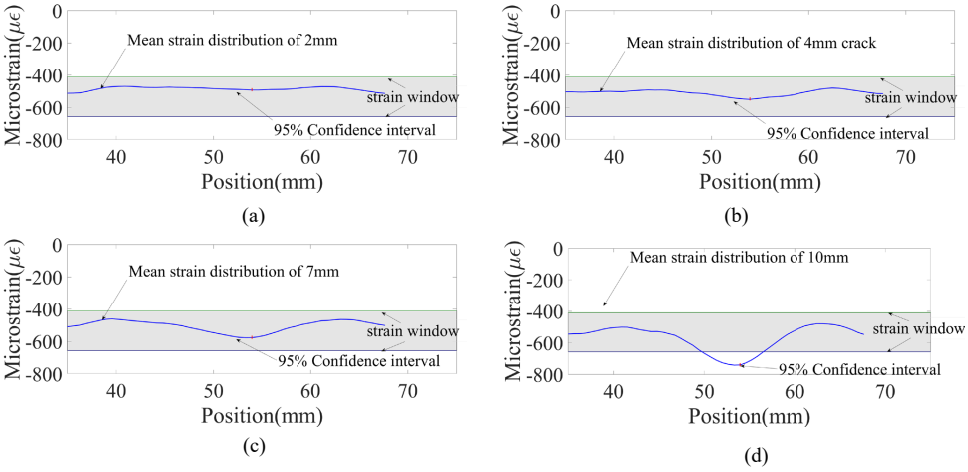

Figure 4.13: Comparison of average strain measurement, 95% confidence interval of the strain near the crack tip, strain window in the traditional specimen of test case 01 as the crack grows from (**a**) 2mm to (**b**) 4mm, (**c**) 7mm, and (**d**) 10mm under 6KN load

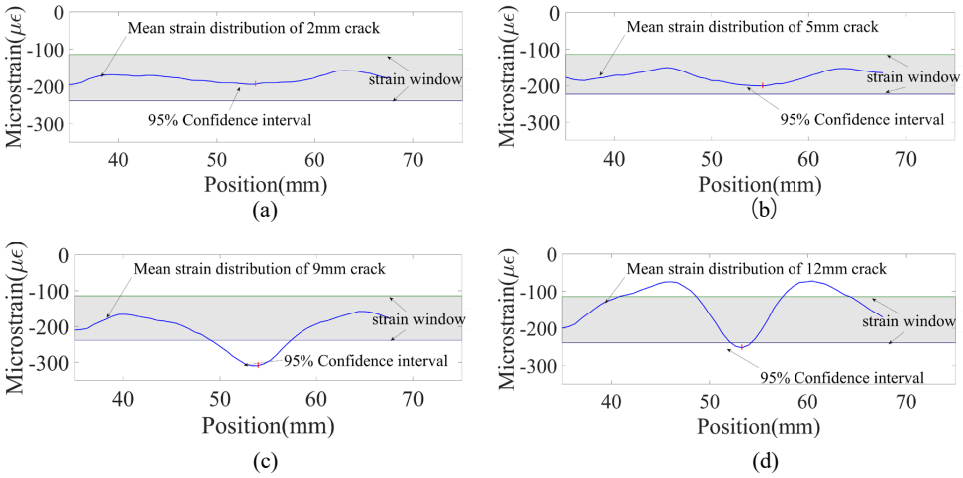

Figure 4.14: Comparison of average strain measurement, 95% confidence interval of the strain near the crack tip, strain window in the SLM specimen of test case 05 as the crack grows from (**a**) 2mm to (**b**) 5mm, (**c**) 9mm, and (**d**) 12mm under 2KN load

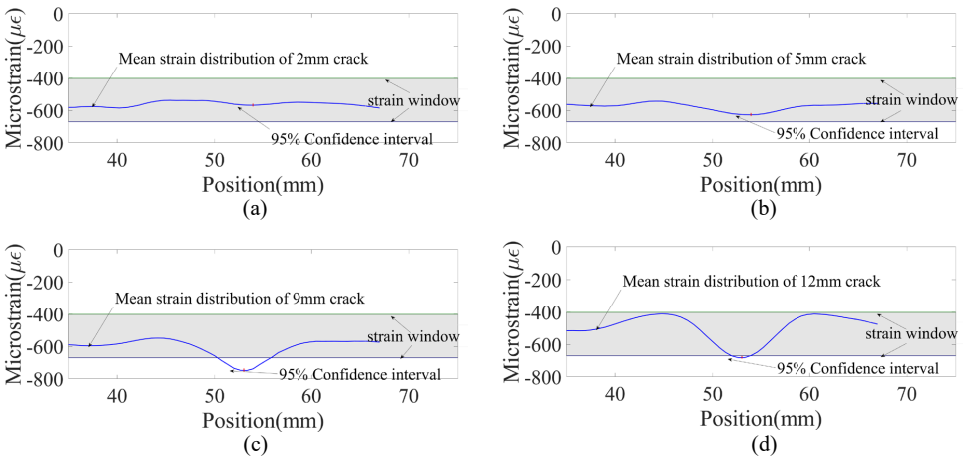

Figure 4.15: Comparison of average strain measurement, 95% confidence interval of the strain near the crack tip, strain window in the SLM specimen of test case 05 as the crack grows from (**a**) 2mm to (**b**) 5mm, (**c**) 9mm, and (**d**) 12mm under 6KN load

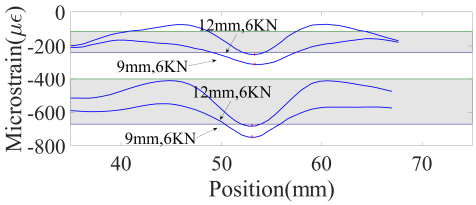

Figure 4.16: Decrease of strain as the crack grows from 9mm to 12mm in the SLM specimen am01 in test case 05

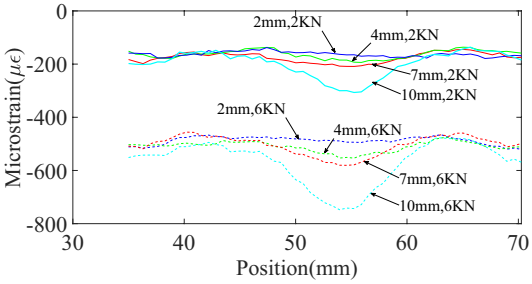

Figure 4.17: Change of the measured strain distribution as the crack grows

strain peak value increases as the crack length increases. First, as the crack grows, the effective cross-section near the crack region, therefore the effective stiffness is reduced and the resulting strain will increase. Second, as the crack grows, the crack tip gets closer to the embedded fiber. The influence of stress concentration also increases. However, as shown in figure 4.16, as the crack grows from 9mm to 12mm, the crack-induced strain peaks value decreases. The propagation of the crack introduces interruption to the structural integrity and the shape of the effective cross-section near the crack changes. The neutral axis may shift upwards, and the distance between the embedded fiber and the neutral axis decreases. As a result, the measured strain also decreases.

4.6.2. VARIATION OF STRAIN DISTRIBUTION SHAPE AS CRACK GROWS

The strain exceedance method for crack detection compares the predicted strain window with the measured strain distribution. Technically, it compares the maximum strain around the crack with the strain value. Therefore, only very limited information is used in the method. However, as can be seen in 4.17, before the crack is detected when the corresponding maximum strain exceeds the strain window, the strain distribution pattern has already changed gradually as the crack grows from 2mm. To be more specific, when the crack length is small relative to the size of the structure, the strain peaks will be highly localized and concentrated near the crack tip. As the crack length increases, the strain peaks will spread over a larger region, leading to a more diffuse strain distribution. This extra information may be further utilized for other crack detection approaches, which will be investigated in the next Chapter.

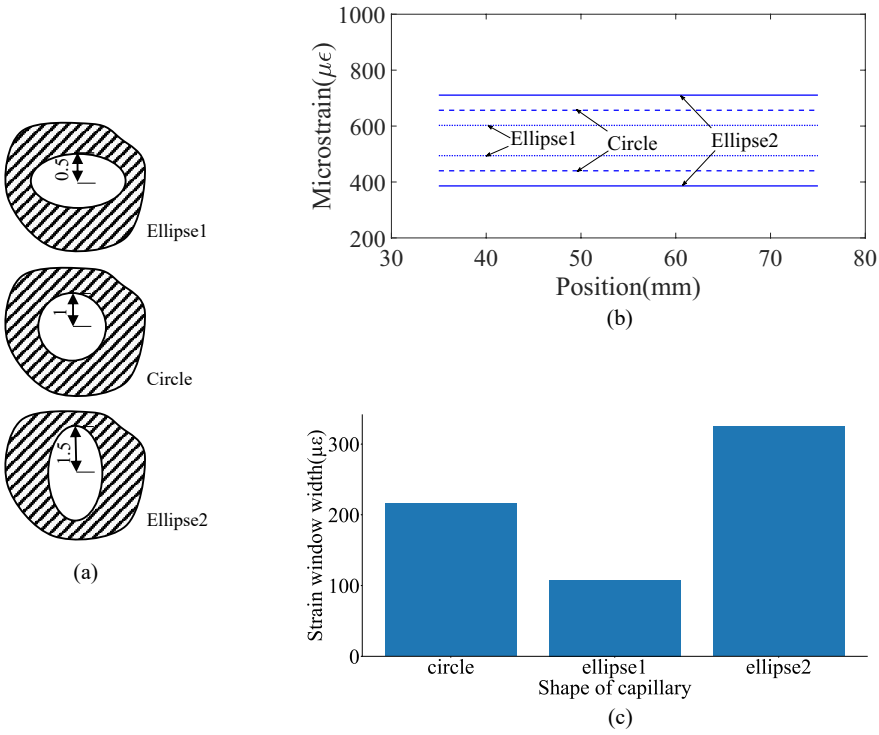

Figure 4.18: (**a**) possible shape of capillary, (**b**) the corresponding strain window and (**c**) strain window width under the loading of 6KN

4.6.3. INFLUENCE OF CAPILLARY SHAPE UNCERTAINTY ON STRAIN WINDOW IN ADDITIVELY MANUFACTURED SPECIMENS

As can be seen in section 4.2.3, although the capillary is designed to be a circle, the actual shape of additively manufactured parts may be different. The shape and dimension inaccuracy associated with additive manufacturing such as laser powder bed fusion and selective laser melting can cause the actual shape of the printed capillary to be different from the designed capillary, and that can create uncertainty associated with the strain window. As can be seen in figure 4.18, the different shapes of capillary, such as circle and ellipse, can lead to different strain window widths, and different strain window widths can create uncertainty for crack detection. Under the loading of 6KN, the strain window increase from around 140$\mu\varepsilon$ to 450$\mu\varepsilon$ from one shape of the capillary to another shape of the capillary. This kind of uncertainty can undermine the effectiveness of the strain exceedance method.

4.7. CONCLUSION

This study proposes a new and simple method to perform crack detection with embedded fiber optic sensors by monitoring when the measured strain distribution exceeds the

strain window based on the possible positional variation of the fiber, and the following conclusions can be reached.

1. Under four-point bending, the simple strain exceedance method can be used to detect cracks in both the traditional specimens and SLM specimens. However, only when the crack grows to a certain length, the crack-induced strain peaks can exceed the pre-defined strain window. It is important to determine the detectable crack length before applying this method.
2. Shape of the strain distribution changes before the strain distribution exceeds the strain window, and therefore information on the strain distribution shape can be extracted and possibly used to detect cracks earlier than the strain exceedance method.

BIBLIOGRAPHY

[1] *What is the minimum bend radius of the fiber?*, Apr. 2020. [Online]. Available: https://fbgs.com/faq/what-is-the-minimum-bend-radius-of-the-fiber/.

[2] M. Strantza, "Additive manufacturing as a tool for structural health monitoring of metallic structures", Ph.D. dissertation, Vrije Universiteit Brussel Brussels, Belgium, 2016.

[3] F. Calignano, M. Lorusso, J. Pakkanen, *et al.*, "Investigation of accuracy and dimensional limits of part produced in aluminum alloy by selective laser melting", *The International Journal of Advanced Manufacturing Technology*, vol. 88, pp. 451–458, 2017.

[4] T. Hesterberg, "Bootstrap", *Wiley Interdisciplinary Reviews: Computational Statistics*, vol. 3, no. 6, pp. 497–526, 2011.

5

INVESTIGATING USING MACHINE LEARNING TO PERFORM CRACK DETECTION WITH THE STRAIN DISTRIBUTION MEASURED BY EMBEDDED FIBER OPTIC SENSOR

5.1. INTRODUCTION

IN the previous chapter, the strain exceedance approach for crack detection is studied. To be more specific, the four-point bending fatigue test was performed on the specimen with embedded fiber optic sensors. The strain distribution was measured in situ with the fiber optic sensor as the crack initiated and propagated, and the measured strain distribution was compared against the pre-defined strain window. When there was not any crack in the specimen, the measured strain distribution lied within the strain window. Any exceedance of the measured strain distribution beyond the pre-defined boundary indicates the existence of the crack. Figure 5.1 represents a change of the measured strain distribution as a crack initiated from the pre-manufactured 2mm-long notch and grew in the SLM specimen am1 of the test. The strain distribution along the capillary boundary in the specimen formed a strain window represented by the gray area in the figure. In the strain exceedance approach for crack detection studied in chapter 4, the measured strain distribution as the crack grows was constantly compared against the strain window to determine if there was any crack. The strain distributions shown in the figure were measured during the four-point bending fatigue test under the loading of 2KN and 6KN, as shown in the section 4.2.4. The strain peak induced by the crack can be clearly seen even when the crack is relatively small, and before the maximum strain of the strain peak exceeds the strain window. Therefore, the strain peak can possibly be used to detect the crack that can not be detected by the strain exceedance method. However, one should be careful when associating the strain peaks with the crack because some other factors such as concentrated load and fiber curvature can also induce strain peaks.

Machine learning has been used in structural health monitoring for crack detection due to its ability to analyze the collected data and identify patterns from data that are associated with cracks. There is limited research on using machine learning to perform crack detection based on the strain measured by distributed fiber optic sensing [1] [2]. Among these examples, fiber optic sensors are bonded straight on the structure surface near the damage hotspot to continuously measure the strain distribution. The existence of a crack can cause strain peaks which can significantly change the strain distribution pattern, and the machine learning model can identify the difference in the strain distributions. The approach has been proven to be successful even when the crack is small and the induced strain peaks are submerged in the measurement noise [1]. The main advantage of the machine learning based method over the simple strain exceedance method in the previous chapter is that the machine learning model can extract more crack-sensitive features from the measured strain distribution for crack detection. The strain exceedance method only compares the maximum strain distribution against the preset baseline for crack detection. That explains why the machine learning based method has great potential to detect cracks that are too small to be detected by the simple strain exceedance approach.

However, unlike the fiber in the previous study, the fiber optic sensors are embedded within a capillary inside an additively manufactured structure and the fiber diameters (195µm,) are much smaller compared to that of the capillary (2mm) in this study. Therefore, the fiber can be at any location within the capillary and any orientations can also

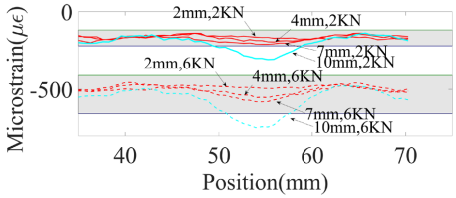

Figure 5.1: Strain distribution measured during test case 05 shown in the table 4.1 under loading of 2KN and 6KN under four-point bending as the crack initiated from the 2mm-long notch and kept growing and the gray area representing the strain window consisting of strain distribution prediction along the capillary boundary

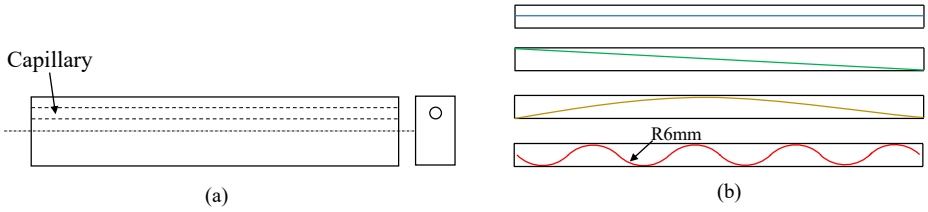

Figure 5.2: (**a**) Schematic representations of beam specimen with capillary; (**b**) Different possible shape of the embedded fibers within the capillary;

be possible as long as it is within the fiber bending limit (bending limit of the fiber used in this study is 6mm [3]), as can be seen in figure 5.2. Possible fiber curvature within the capillary can also cause strain peaks. In addition to the fiber curvature, the concentrated load from the loading pins can also cause strain peaks. When a concentrated load is applied to the specimen during four-point bending, its influence on the strain field is greatest at the point of contact and decreases as the distance from the contact point increases, and that can potentially induce peaks in the strain distributions. The strain peaks induced by crack, fiber curvature, and concentrated load can appear very similar from the human's eye under certain loading such as four-point bending, as shown in figure 5.3.

The curved fiber will take on an arc-like shape, depending on the degree of bending [4]. The arc-like shape of a curved fiber can also be seen in figure 5.4, where a fiber used in this study is bent purposely for observing the bending fiber shape. The arc-like shape of a bending fiber influences shape of the strain peak induced by a bending fiber.

The strain distribution induced by a crack is influenced by different factors such as the loading level and proximity of the crack to the fiber optic sensors or the crack length. When the crack length is small relative to the size of the structure, the strain peaks will be highly localized and concentrated near the crack tip. As the crack length increases, the strain peaks will spread over a larger region, leading to a more diffuse strain distribution. Similarly, the shape of the fiber curvature induced strain distribution depends on how much the fiber is curved.

The possible curvature of fiber might impact the ability of machine learning to detect cracks. In this study, both the crack and curvature of the embedded fiber within the

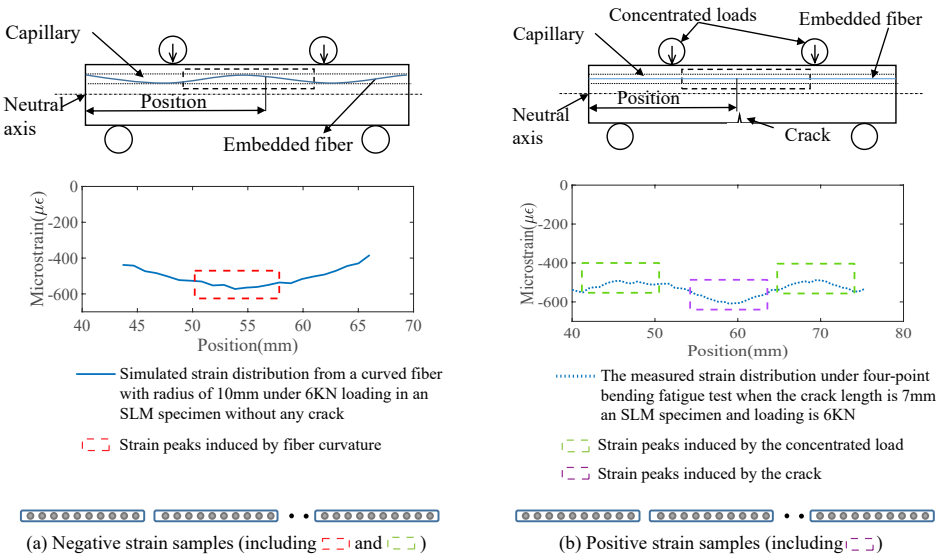

Figure 5.3: (**a**) The negative strain distribution including fiber curvature induced strain peaks from simulation and the concentrated load induced strain peaks from the four-point bending fatigue test; (**b**) The positive strain samples including the crack-induced strain peaks from the four-point bending fatigue test 06 shown in the table 4.1;

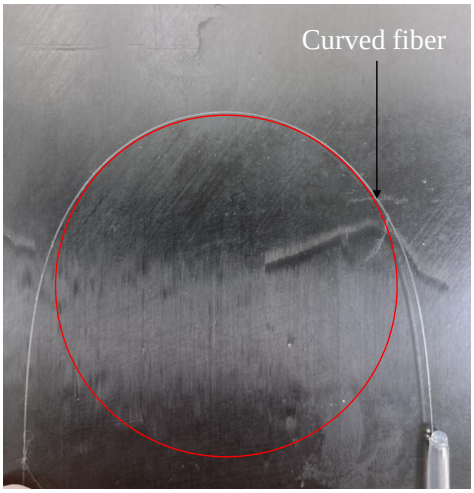

Figure 5.4: Arc-like shape of a curved fiber

capillary can induce similar strain peaks. Measuring strain distribution with embedded fiber might increases the difficulty of using machine learning to detect cracks due to the uncertainty of the shape of the embedded fiber. This difficulty may become particularly pronounced when attempting to detect cracks that are too small to be identified using the strain exceedance based approach. Therefore, in this chapter, the following research question will be answered.

'How can we use machine learning to detect cracks which can not be detected with the simple strain exceedance method, using the fiber optic sensors embedded within the SLM specimen? '

As mentioned above, various studies have used traditional machine learning algorithms to perform damage detection. However, traditional machine learning algorithms require substantial domain knowledge to extract damage-sensitive features from the raw data. Deep learning approaches such as deep neural networks and autoencoders can use the raw data as input, and extract damage-sensitive features during the training process. The deep learning approach has been used in a few structural health monitoring applications. Song et al. trained a five-layer deep neural network (DNN) model with strain distribution measured by Brillouin optical time-domain analysis (BOTDA) technology and detected micro cracks with very high accuracy [5]. Cristiani et al. developed a convolutional neural network to predict delamination in carbon fiber reinforced plastics (CFRP) specimens [2]. Sbarufatti established a three-layer artificial neural networks (ANN) model for the diagnosis of fatigue damage on an aeronautical structure [6].

Due to its successful application in extracting noise-robust features and detecting small cracks with high accuracy, the DNN algorithm is utilized to create a classification model in this study in order to detect those small cracks which can not be detected by the simple strain exceedance method. The strain distribution is measured by fiber optic sensors, and an algorithm is developed to extract all the local strain peaks. The strain peak is a strain subsequence with a certain length, which is a localized region of high strain relative to the surrounding strains. The strain subsequence can basically be classified with the DNN model into two categories. The first category is the crack strain subsequence (CS) when the strain peak is induced by cracks and the second one is the normal strain subsequence (NS) when the strain peak is induced by fiber curvature or other non-crack factors. The middle layers of the DNN model can be used to extract useful crack-sensitive features from the strain peak, and extracted feature representation will be passed into the final layer to decide if the input strain sequence is CS or NS. The CS/NS binary classification result can be used as the crack detection result. Extracted strain peak rather than the whole strain distribution along the embedded fiber is used for crack detection, and that is because the embedded fiber can be at any location within the capillary and any orientations can also be possible as long as it is within the fiber bending limit (bending limit of the fiber used in this study is 6mm [3]). It is easier to collect enough data that represents all the strain peaks induced fiber curvature and crack lengths because there is a limit to the fiber bending curvature and crack length.

As this chapter investigates if machine learning can be used to detect small cracks given the fiber is embedded and can possibly curve, the proposed method will be verified with

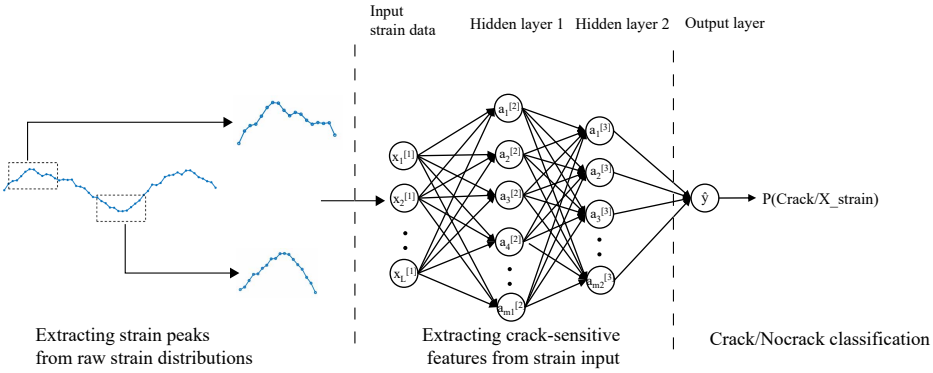

Figure 5.5: An overview of the machine learning based method which includes three stages: extracting the strain peaks from the raw strain distribution, extracting the crack-sensitive features from the strain data input, and Crack/Nocrack classification

data collected from the simulation and the four-point bending fatigue test performed previously, which is shown in the section 4.2. There are possibly numerous shapes of embedded fiber within the capillary, and therefore it is very demanding in terms of time and money to collect enough strain distribution data representing all cases for the fiber with different shapes, which is important to build and train a reliable machine learning model. Therefore the simulation is performed to help collect enough strain distribution data at an acceptable cost.

5.2. METHODOLOGY

The crack detection process involves three stages, as shown in figure 5.5. The first stage is the data extraction step. The purpose of this step is to extract strain peaks possibly induced by crack or fiber curvature along the full strain distribution measured by distributed fiber optic sensors. The second stage is to input the extracted strain peaks into the carefully-designed DNN model for extracting noise-robust and crack-sensitive features. The last stage is the CS/NS classification stage. The feature representation extracted from the second stage is fed into an output layer of the DNN model. The output layer is a sigmoid classifier used for binary classification, and the results of the last stage are two probabilities, $P(Crack \backslash X_{strain})$ and $P(Nocrack \backslash X_{strain})$. The $P(Crack \backslash X_{strain})$ represents the probability that the extracted strain peaks are induced by a crack, and $P(Nocrack \backslash X_{strain})$ is the probability that the extracted strain peaks are induced by a non-crack factor such as fiber curvature. The results of crack detection are based on whichever of the two probabilities has a greater value. There may be a couple of strain peaks extracted from the whole strain distribution, and if any one of the strain peaks is predicted to be induced a crack, it can be concluded that there is a crack in the monitored structure.

5.2.1. DATA PROCESSING

In order to use the designed DNN model to perform binary classification, the model needs to be trained with the strain data. The required dataset for training a machine learning model should be prepared first. As can be seen in figure 5.3, there are the strain distributions peaks induced by the fiber curvature and the concentrated load of the upper loading pins, these strain distributions are assigned into a category known as the negative strain samples. There are strain distribution peaks induced by the crack, and they are assigned a category known as the positive strain samples. All the strain samples have a specified length. The length should not be too big, for example, a strain sample contains two strain peaks. Because it is hard to localize the exact position of each possible crack when crack localization is needed. The length should also not be too small, for example, the strain sample length is much smaller than the length of the crack-induced strain peak. Because it will be difficult to extract enough crack-sensitive features from the strain distribution.

The following steps can be implemented to extract all the strain peaks induced by three factors including cracks, fiber curvature, and concentrated load. First, denoising the raw strain distribution. That is because measured strain distribution contains low-frequency measurement noise, and the existence of noise makes it hard to precisely localize all strain peaks induced by the crack and fiber curvature. The denoising process effectively eliminates high-frequency components that correspond to measurement noise, while preserving low-frequency components that reflect the strain peaks resulting from the crack or fiber bending. Second, calculating the derivatives of strain distribution for all the positions, and determining the location of all the strain peaks where the derivatives are zero or very close to zero. Finally, extracting the strain sequences from the raw strain distribution of a specific length, which is centered on the determined location.

To represent the categorical information in a format that can be easily processed by a machine learning algorithm, each of the two classes of "Positive strain samples" and "Negative strain samples" is labeled with a numeric value. In this case, the "Positive strain samples" and "Negative strain samples" are labeled with 1 and 0 respectively.

5.2.2. THE DEEP NEURAL NETWORK MODEL AND ITS TRAINING PROCESS

The DNN is the main body of the proposed methodology in figure 5.5. The DNN model mainly includes four layers. The first layer is the input layers which receive the extracted strain peaks as input, the second and third layers are the hidden layers used to extract feature representations from the raw input, and the fourth layer is the output layer, a decision layer outputting the probabilities that there is a crack or no crack in the monitored structure. More details and the theoretical foundations of deep neural networks are introduced below.

Deep neural networks consist of three primary constituents: the input layer, hidden layers, and output layer. The input layer is responsible for receiving raw data, which is then subjected to transformation and processing via one or more hidden levels. The output layer produces a prediction or classification outcome using the input data. As shown in figure 5.6, the proposed DNN includes one input layer, two hidden layers, and one output layer. The input layer, first hidden layer, and second hidden layer have L, $m1$, and

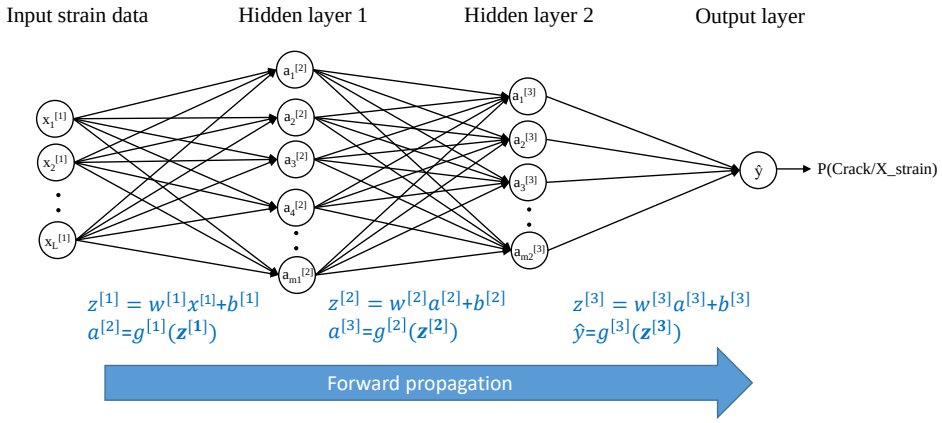

Figure 5.6: The forward propagation of the DNN model, which can map the input strain distributions to the target probability

5

$m2$ neurons respectively.

The DNN generates its output from input data through forward propagation. Calculating the weighted sum and using an activation function are the two main components of forward propagation. Specifically, for each layer, the first step is to compute the weighted sum of the input values and the weights associated with each neuron in the network. This involves multiplying the input vector by its corresponding weight vector w and adding the bias vector b. The weighted sum is then processed via an activation function, introducing nonlinearity into the neuron's output. The Relu function is used as the activation for the input layer and hidden layers. The Relu function is used because it can introduce the non-linearity into the DNN model and avoid the vanishing gradient problem [7]. The sigmoid function $g(z)$ shown in equation 5.1 is chosen as the activation in the output layer. The sigmoid function can be used as an activation function in the output layer because its output can be interpreted as probabilities and it squashes its input into the [0,1] range [8]. That is important for making decisions based on classification probabilities.

$$s(x) = \frac{1}{1+e^{-x}} \tag{5.1}$$

During forward propagation, each neuron in the network receives input from the preceding layer and generates output, which is then transmitted to the next layer. This procedure is repeated until the final output, which is the probability that there is a crack in the monitored structure for the given strain distribution, is produced.

In order to let the DNN learn an accurate mapping or function from the input strain data to a probability, it is necessary to train the neural network. Through training, the weights and biases are updated so the DNN can produce accurate outputs for inputs it has not seen before. In this study, The free weights parameters w and bias parameters b

are updated based on the data set $(x_1, y_1), (x_2, y_2), (x_3, y_3), ..., (x_m, y_m)$ by minimizing the cost function $L(\hat{y}, y)$.

$$L(\hat{y}, y) = -\frac{1}{m}(\sum_{i=1}^{m}(-y_i \log(\hat{y}_i) - (1-y_i)\log(1-\hat{y}_i)) + \frac{\lambda}{2m}\sum_{l=1}^{L-1}\sum_{i=1}^{s_l}\sum_{j=1}^{s_{l+l}}(w_{ji}^{l})^2 \tag{5.2}$$

x_i is the ith strain sample, which is the extracted strain value sequence, y_i is the true target value 1 or 0 for the ith strain sample, and both of them are prepared in section 5.2.1. $\hat{y}_i$ is the output the of DNN model, which is the predicted target value for the ith strain sample. L is the total number of layers, s_l is the total number of neurons in the l layer, and w is the weight coefficient. The optimal value of the weight w and bias b can be estimated by minimizing the cost function $L(\hat{y}, y)$. The optimization process is implemented by the mini-batch gradient descent algorithm when taking the dataset size into consideration.

5.2.3. AN OVERVIEW OF THE DNN MODEL DEVELOPMENT PROCESS

Figure 5.7 shows the process of developing a DNN model to detect any crack within the monitored structure using the strain distribution. There are mainly three stages for developing the model.

Stage 1. Data preparation. After the strain distributions are measured by the distributed fiber optic sensors. The strain peaks induced by various factors including fiber curvature, concentrated load, and crack are extracted. These strain peaks are strain value sequences that fall into two categories of positive strain samples and negative strain samples. The strain peaks belonging to the two categories are assigned a target value of 1 and 0 respectively. The strain peak values and its corresponding target value make up a data sample. All the data samples are divided into a training, validation, and test dataset.

Stage 2. Model building & training. In this stage, a DNN model is initiated with the TensorFlow 2 framework [9]. The number of layers and the number of neurons in the hidden layers are usually small so that the model can be quickly tested and evaluated. The number of neurons in the input layer is the same as the length of the input strain sequence. There is only one neuron in the output layer which represents the probability that extracted strain peak is induced by a crack. After the model is created, it is trained in a supervised way with the training dataset prepared in stage 1. Model training is a repetitive process. After the model is trained, the hyper-parameters are carefully tuned to optimize the model. The training will be performed again. This cyclic process of model training and hyperparameters tuning is repeated until the desired model performance is achieved.

Stage 3. Well-trained model assessing. The well-trained model needs to be evaluated for its performance. Different evaluation metrics can be used to evaluate the classification model's performance, such as accuracy. The testing dataset is used to assess the trained model in order to provide an unbiased evaluation. As mentioned above, if the model performance is not desired, the model hyperparameters will be tuned and the new model will be trained again.

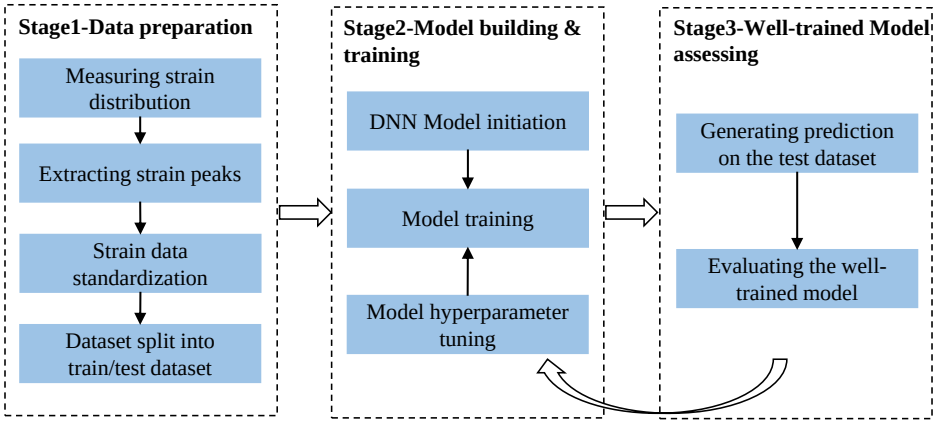

Figure 5.7: The process of developing a DNN model to detect the crack within the monitored structure using the strain distribution

5.3. VERIFICATION OF THE PROPOSED METHODOLOGY WITH FOUR-POINT BENDING FATIGUE TEST AND FEM

5.3.1. STRAIN DATA COLLECTION

In order to validate the proposed methodology, it is necessary to collect strain distributions containing strain peaks induced by various factors such as cracks and fiber curvature. The strain peaks induced by cracks can be collected via the four-point bending fatigue test introduced in section 4.2. In the test, a crack was initiated and propagated in each of the 2 SLM specimens. The distributed fiber optic sensors are embedded within the pre-manufactured capillary within each specimen, providing a real-time and in-situ strain measurement. The results in experiment cases 05 and 06 as shown in table 4.1 will be processed and used for training the model.

In order to collect the strain distribution induced by the fiber of different curvature radius, the same FEM model established in section 3.3 is employed to simulate the strain distributions along the curved fiber. One exception is that an arc-like path rather than the straight path is defined. The strain values along the arc-like path with a curvature radius up to the fiber's curvature radius limit of 6mm, as shown in 5.8, are collected. The strain values at different positions along the path are multiplied with the corresponding coefficients to account for the change in the fiber orientations along a curved fiber. Increasing the curvature radius of the curved region from 6mm to 200 mm with a step size of 0.5 can generate around 388 shapes of fiber optic sensors with decreasing degrees of bending. These strain peaks induced by these different shapes of curved fiber and cracks with lengths ranging from 2mm to 10mm are also collected. In total, there are 3880 simulated strain distributions from FEM. The measured strain distribution when there is not any loading is regarded as the measurement noise. The measurement noise is added to all the simulated strain distributions.

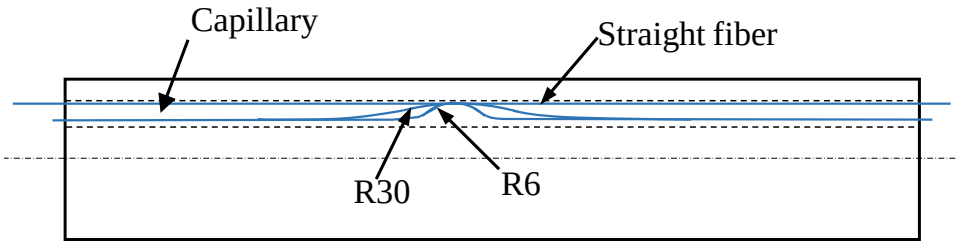

Figure 5.8: Three states of the embedded fiber within the capillary: straight and bending with an arc-like region with a curvature radius of 6mm and 30mm

Table 5.1: Source of strain data used for training and its size

Source of strain data	Number of strain samples
Fatigue test 05 shown in section 4.2	2500
Fatigue test 06 shown in section 4.2	2500
FEM	9700

In fatigue tests 05 and 06 as shown in table 4.1, the strain distributions are measured under the loading of 2KN and 6KN as the crack grows from 2mm till the specimens break. As shown in figure 4.7, there is the pre-manufactured notch on the specimen bottom where the crack will initiate, and crack length is regarded as the total length of the notch and crack initiated around its end. Therefore the initial crack length is 2mm.

For each of the two SLM AlSi10Mg specimens, there are 1000 strain distributions collected under the loading of 2KN and 6KN respectively. Each strain measurement contains 168 sampling points distributed along the embedded fiber and represents a strain sequence. In total, 5000 such strain sequences were collected during fatigue tests for both specimens. The data used for training a classification model can be seen in table 5.1.

5.3.2. STRAIN DATA PROCESSING

In figure 5.9, some of the raw strain distributions collected under the loading of 6KN for an SLM specimen are displayed. To extract the strain peaks induced by various factors such as a crack or concentrated load, the following method is implemented. First, the moving average filter was applied to the raw strain. The moving average filter took the average of a sliding window of data points and substituted the average value for the center point. By employing an appropriate window size, it was possible to remove high-frequency noise from a signal while maintaining its low-frequency components. The window size was mainly determined by the trial-and-error approach until all strain peaks induced by various factors such as crack and fiber curvature can be extracted. Then, the first derivative was computed for the smoothed strain distribution, and the zero value of the first derivative indicated the positions of the local maximum and minimum values of the strain distribution, which was induced by the crack, fiber curvature, and concentrated load. Figure 5.10 shows the strain peaks extraction process of two examples corre-

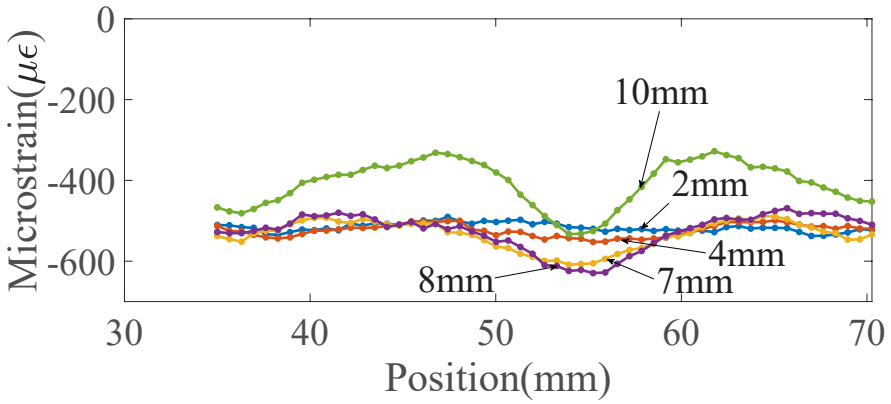

Figure 5.9: The raw strain distribution measured by fiber optic sensor during the fatigue test 06 shown in table 4.1 when the crack lengths increased from 2mm for an SLM specimen under the loading of 6KN

sponding to the 4mm crack and 7mm crack in figure 5.9. The strain peaks position in the figure corresponds to the local maxima and minima of the strain distribution. The strain sequences centered on these local maxima and minima are extracted, which include 16 strain values. These strain sequences are marked by boxes in the figure.

The FEM simulates the strain distributions along a curved fiber with different curvature radius. In addition, When there is any crack near the curved fiber, the strain peaks induced by the crack and curved fiber overlap, which can be seen in figure 5.11. The strain peaks containing 16 strain values along the curved fiber are extracted from the strain distribution and fed into the DNN model.

As introduced in 5.2.1, the strain peak induced by a crack and concentrated load shown in figure 5.10 is categorized into "positive strain samples" and "negative strain samples", and the strain peaks induced by fiber curvature in figure 5.11 are categorized into "negative strain samples". The label value of 1 is allocated to the "positive strain samples," while the label value of 0 is applied to the "negative strain samples.". In total there are 11380 strain samples including 5000 positive strain samples and 6380 negative strain samples, it is divided based on the ratio of 6:2:2 into the training, validation, and testing dataset. The training dataset is used to learn the model weights and biases, the validation dataset is used for model optimization and the testing dataset can provide an unbiased evaluation of the model performance.

5.3.3. MACHINE LEARNING MODEL EVALUATION METRICS

The evaluation metrics can provide a quantitative measure of the performance of a machine learning model, and it is mainly determined by comparing the model-predicted label and the true label of the input strain sequences. FP (False Positives), TP (True Positives), FN (False Negatives), and TN (True Negatives) are commonly used evaluation metrics in machine learning for binary classification problems. These metrics can be used to calculate the accuracy acc of the well-trained machine learning model, as

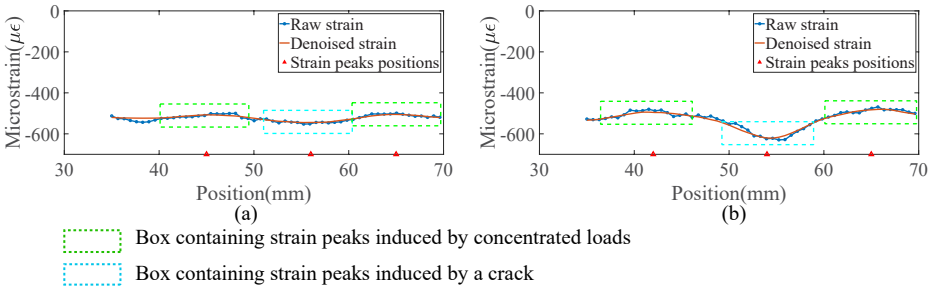

Figure 5.10: The raw strain distribution measured by fiber optic sensor during fatigue test 06 shown in table 4.1 when the crack lengths are 4mm (**a**) and 7mm (**b**) respectively under 6KN loading, the denoised strain distributions with moving average filter, the strain peaks positions where the gradients of denoised strain distributions are zero, the strain peaks contained in a rectangle box, which will be fed into the DNN model.

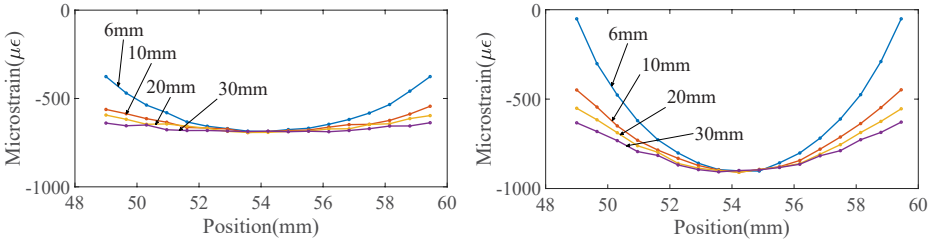

Figure 5.11: (**a**) The simulated strain distribution along a curved fiber with curvature radius ranging from 6mm to 30mm; (**b**) The simulated strain distribution when the strain peaks induced by curved fiber with different curvature radius and a 6mm-long crack

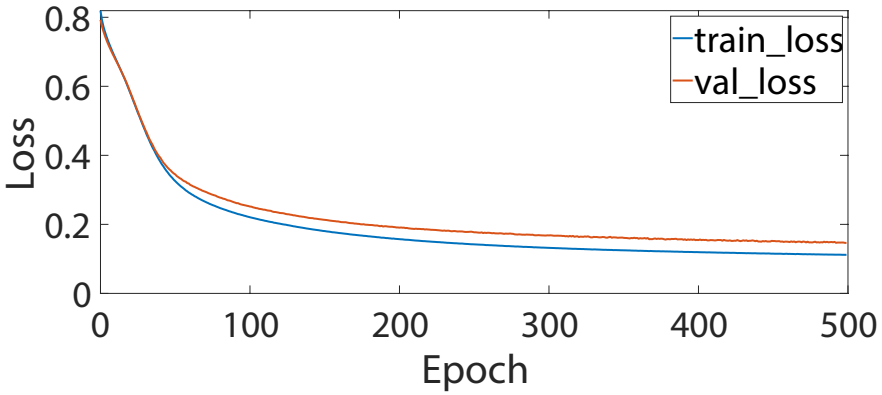

Figure 5.12: The cross-entropy loss as a function of epochs

shown in equation 5.3

$$acc = \frac{TP + TN}{TP + TN + FP + FN} * 100\% \tag{5.3}$$

5.4. RESULTS AND DISCUSSIONS

5.4.1. EVALUATION OF THE PROPOSED METHOD AND COMPARISON WITH TRADITIONAL ALGORITHMS

There are model parameters and model hyperparameters that need to be determined. Model parameters define a model's behavior and can be learned from the training dataset. Model hyperparameters are parameters set prior to training, including the number of layers and neurons in each layer. The structure of the DNN is chosen to be 15-40-20-2, and the structure is determined through the trial-and-error approach. When determining the model structure, different factors including model's ability to generate right outcome for input strain data, model's complexity, and the required computational source etc. need to be considered.

When using the mini-batch gradient descent algorithm to train the DNN model, the maximum epoch is set to be 500. The early stop approach is adopted for the training. As can be seen in figure 5.12, both the training and validation loss decrease abruptly until 100 epochs, and the loss stabilizes after 400 epochs.

There are samples in the testing data, and there are positive strain samples and negative strain samples. The evaluation results of the well-trained model are shown in table 5.2.

As can be seen in table 5.2, the performance of the proposed model is compared with the performance of traditional algorithms including random forest classifier and support vector machine classifier. The support vector machine classifier uses the linear kernel and the random forest classifier uses 200 estimators and a maximum tree depth of 6. Both the random forest and support vector machine classifier are built and optimized

Table 5.2: Evaluation results of the well-trained DNN model

Model	False positives (FP)	False negatives (FN)	Accuracy(%)
Proposed method	**15**	**17**	**98.6**
Random forest classifier	133	86	90.4
Support vector machine classifier	81	162	89.2

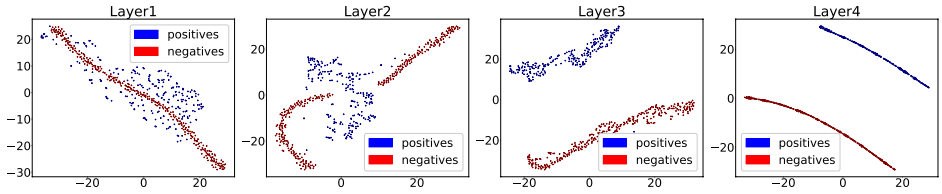

Figure 5.13: Layerwise visualization of the feature representations extracted from different layers of the proposed model

with the sklearn 1.1.2 package [10]. All three models in the table are trained and tested with the same testing dataset. With the proposed model, there are totally 38 prediction errors, including 17 false positives and 21 false negatives, and the classification accuracy calculated with equation 5.3 is 98.6%. The classification accuracy for the random forest and support vector machine classifier are 90.4% and 89.2% respectively. Therefore, the proposed model has been improved compared with the traditional algorithms.

5.4.2. LAYERWISE VISUALIZATION OF EXTRACTED FEATURE REPRESENTATION

In order to more intuitively understand how the input data is transformed and provide a visual representation of the discriminability change of the extracted features, the t-SNE is applied to different layers of the proposed DNN model. The t-SNE algorithm can represent high-dimensional data points as points in a low-dimensional space, such as two or three dimensions while preserving the pairwise similarities between the high-dimensional points as much as possible. The algorithm achieves this by minimizing a cost function called Kullback–Leibler divergence that measures the difference between the pairwise similarity distributions of the high-dimensional and low-dimensional data points. By minimizing the cost function, the data samples within the same class get closer, and data samples from different classes move farther apart.

Figure 5.13 represents the layerwise visualization of the feature representations extracted from different layers of the proposed model. The points are the two-dimensional representations of the multi-dimensional strain sequences, and the two-dimensional features are acquired by performing T-SNE dimension reductions on the multi-dimensional strain sequences. The blue and red patch represents the positive and negative strain samples, the strain peaks induced by a crack, and other factors including fiber curvature. It can be seen in the figure that the discriminability of the features belonging to two different classes is increasing steadily as the data passes through different layers of the proposed DNN model.

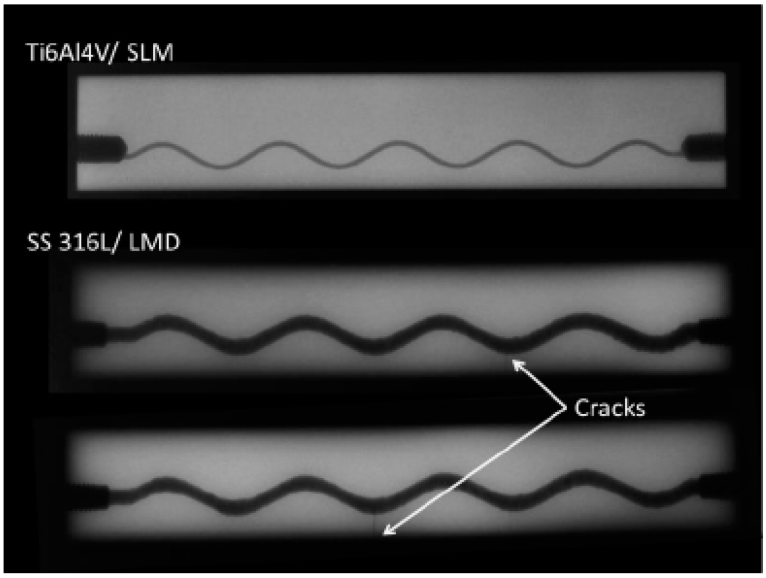

Figure 5.14: Radiographic image of the crack being detected by the vacuum sensors in an SLM specimen during a four-point bending test from the study [11]

5.5. COMPARISON OF THE PROPOSED CRACK DETECTION METHOD WITH THE METHOD IN THE PREVIOUS STUDY

Figure 5.14 shows a radiographic image of the crack being detected by the vacuum sensors in an SLM specimen during a four-point bending test, which is proposed by Strantza [11]. It can be seen that the crack needs to be big enough to break the vacuum state, the pressure change can be detected, and then the crack can also be detected. The crack detection result of the proposed method in this study can be further compared against that of Strantza's study [11]. The comparison result can be seen in figure 5.15. The vacuum sensor based method requires the crack tip to grow to the capillary to be detected, the strain exceedance method requires the crack to be close to the capillary (4-6mm) away to be detected in this study, and the machine learning can even detect a crack when it is much farther away from the capillary compared with the other two methods. Therefore, the machine learning based crack detection method can detect much smaller cracks compared with the method. That makes it applicable to more situations, especially for those cracks which are too small to be detected by other two methods.

5.6. CONCLUSION AND LIMITATION OF THE PROPOSED METHOD

A deep neural network model is proposed to detect the small cracks that can not be detected with the strain exceedance approach. The proposed deep neural network (DNN) is a four-layer neural network model which can take the strain peak in the form of a strain sequence, extract crack-sensitive features, and output a probability that the strain peak is induced by a crack. The dataset for training the model is collected by the four-point

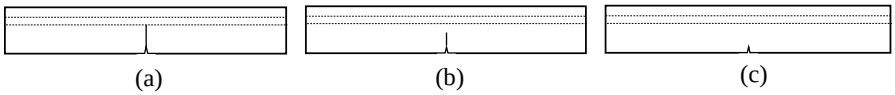

Figure 5.15: Comparison of the detectable crack length of (**a**) the vacuum sensor methodology proposed by Strantza [11], (**b**) the strain exceedance based method in chapter 4, and (**c**) the machine learning based method in this study in chapter 5

bending fatigue test and FEM simulation. The four-point bending fatigue test measures the strain distribution as the crack initiated and propagated in an SLM beam structure. The strain peaks are extracted from the full strain distributions measured along the full fiber. Because it is very difficult if not impossible to collect the strain distribution along curved fiber with various curvature radius when the fiber is embedded within the capillary during four-point bending test, FEM is employed to simulate the strain distributions along curved fiber. The proposed model is verified with strain distributions measured with embedded fiber optic sensors during the four-point bending test. The results showed that 98.6% cracks with lengths over 2mm can be successfully detected. Therefore the proposed model demonstrates the ability to detect cracks which are too small to be detected by the simple strain exceedance method describe in the previous chapter.

It should also be noted that the proposed DNN-based crack detection approach is dependent on the data that is used to train the model. That may cause the proposed model may have insufficient generalizability, especially for new structures or situations that can generate data that is significantly different from the training data. More work can be done to overcome the limitation of the proposed method. One approach is data augmentation, and more data generated from different structures and loading types can be used to augment the training dataset. That can facilitate the established machine learning model to recognize patterns that are more generalizable across various structures and situations. The second way is transfer learning. Transfer learning is a machine learning technique that utilizes a previously trained model as a beginning point for a new machine learning model. A pre-trained model can be fine-tuned on a smaller dataset of strain distribution data from a new structure or loading type so that the new model can be more adaptable to various loading types and structures.

BIBLIOGRAPHY

[1] P. Guo, W. Meng, and Y. Bao, "Automatic identification and quantification of dense microcracks in high-performance fiber-reinforced cementitious composites through deep learning-based computer vision", *Cement and Concrete Research*, vol. 148, p. 106 532, 2021.

[2] D. Cristiani, F. Falcetelli, N. Yue, *et al.*, "Strain-based delamination prediction in fatigue loaded cfrp coupon specimens by deep learning and static loading data", *Composites Part B: Engineering*, vol. 241, p. 110 020, 2022.

[3] *What is the minimum bend radius of the fiber?*, Apr. 2020. [Online]. Available: https://fbgs.com/faq/what-is-the-minimum-bend-radius-of-the-fiber/.

[4] A. J. Y. Tan, S. M. Ng, P. R. Stoddart, and H. S. Chua, "Theoretical model and design considerations of u-shaped fiber optic sensors: A review", *IEEE Sensors Journal*, vol. 20, no. 24, pp. 14 578–14 589, 2020.

[5] Q. Song, Y. Chen, E. Abdoli Oskoui, *et al.*, "Micro-crack detection method of steel beam surface using stacked autoencoders on massive full-scale sensing strains", *Structural Health Monitoring*, vol. 19, no. 4, pp. 1175–1187, 2020.

[6] C. Sbarufatti, "Optimization of an artificial neural network for fatigue damage identification using analysis of variance", *Structural Control and Health Monitoring*, vol. 24, no. 9, e1964, 2017.

[7] J. Schmidt-Hieber, "Nonparametric regression using deep neural networks with relu activation function", 2020.

[8] C. Nwankpa, W. Ijomah, A. Gachagan, and S. Marshall, "Activation functions: Comparison of trends in practice and research for deep learning", *arXiv preprint arXiv:1811.03378*, 2018.

[9] *Create production-grade machine learning models with tensorflow*. [Online]. Available: https://www.tensorflow.org/.

[10] *Sklearn user guide*. [Online]. Available: https://scikit-learn.org/stable/user_guide.html.

[11] M. Strantza, "Additive manufacturing as a tool for structural health monitoring of metallic structures", Ph.D. dissertation, Vrije Universiteit Brussel Brussels, Belgium, 2016.

6

CONCLUSIONS AND RECOMMENDATIONS

6.1. CONCLUSIONS FROM THE RESEARCH QUESTIONS

The study investigated the feasibility of performing crack detection with the embedded fiber in the additively manufactured specimen. Firstly, this study proposed a novel approach to embedding fiber sensors via a predefined capillary in the Selective laser melted (SLM) structure. The strain measurement accuracy of the embedded fiber via a capillary in the additively manufactured specimen was investigated. An analytical model based on the Euler-Bernoulli beam theory and finite element model was established. The static four-point bending test was utilized to verify the model. Then the strain window concept was proposed for crack detection. The strain window based method for crack detection was evaluated with the four-point bending fatigue test. Finally, after examining the limitation of the strain exceedance method, a machine learning model was further developed, which was aimed at detecting smaller cracks. The two crack detection method proposed in this study was compared with the previous vacuum sensor based method for crack detection in the additively manufactured structure. The following are the conclusions from the proposed research questions.

Question 1: *'How do the fiber locations and orientations within the capillary uncertainty influence the measurement accuracy of the fiber optic sensor? '*

Answer When an optical fiber is embedded within a specimen using capillaries, both fiber positions and orientations may vary along the fiber. Variation of fiber orientations has negligible influence on strain measurement accuracy compared with fiber position variations. Therefore, fiber position uncertainty is the main factor influencing strain measurement accuracy. Even the positional uncertainties of the embedded fiber within capillaries can cause strain measurement uncertainties, the measured strain distributions lie within a pre-defined strain window. The strain window is defined by the strain

distribution along the capillary boundary when there is not any crack in the specimen. Therefore it is possible to perform crack detection using the strain window.

Question 2: *'How effective is the strain-exceeding based method for detecting cracks in additively manufactured parts with embedded fiber optic sensors? '*

Answer Under four-point bending, the simple strain exceedance method can be used to detect cracks in both the traditional specimen and the SLM specimens. In this study, the crack can be detected when its length is 9-11mm (its tip is 4-6mm away from the embedded fiber optic sensor) in both specimens. The shape of the strain distribution changes before the strain distribution exceeds the strain window, and therefore the shape of the strain distribution may be used to detect cracks earlier than the strain exceeding method.

Question 2: *'How can we use the machine learning based method to detect any crack within the monitored structure using the measured strain distribution with the embedded fiber optic sensors? '*

The results from the developed deep neural network model showed that 98.6% cracks with lengths equal to or larger than 2mm can be successfully detected. Therefore the proposed model demonstrates an ability to detect cracks that are too small to be detected by the simple strain exceedance method.

Both the strain exceedance based method and machine learning based method for crack detection, as well as the vacuum sensor based method proposed by Strantza [1] exhibit different crack detection capabilities, each with its own detectable crack length range (DCLR). In the study, the machine learning based method can detect the smallest crack compared with the other two and thus has the largest DCLR due to its ability to extract more information from the strain distribution. The strain exceedance based crack detection method ranks second, and the vacuum sensor based method has the smallest DCLR because it requires the crack break the vacuum sensor for crack detection. Therefore, the selection of the crack detection method in different situations should be based on the DCLR requirement.

6.2. RECOMMENDATIONS FOR FUTURE WORK

The proposed deep neural network based crack detection method in this study is dependent on the data that is used to train the model. That may cause the proposed model may have insufficient generalizability, especially for new structures or situations that can generate data that is significantly different from the training data. More work can be done to overcome the limitation of the proposed method. One approach is data augmentation, and more data generated from different structures and loading types can be used to augment the training dataset. That can facilitate the established machine learning model to recognize patterns that are more generalizable across various structures and situations. The second way is transfer learning. Transfer learning is a machine learning technique that utilizes a previously trained model as a beginning point for a new machine learning model. A pre-trained model can be fine-tuned on a smaller dataset of strain distribution data from a new structure or loading type so that the new model can be more adaptable to various loading types and structures.

ACKNOWLEDGEMENTS

I would like to express my deepest gratitude to my promoter Prof. Rinze Benedictus and co-promoter Dr. Calvin Rans for giving me the opportunity to pursue my PhD at TU Delft. I want to thank Dr. Calvin for giving me invaluable feedback during my progress meeting, which can clear up my confusion and help me make progress. I enjoy every meeting and discussion with you. I would like to thank my second supervisor Dr. Dimitrios for giving me guidance on machine learning.

I want to thank our secretary Gemma who gave me a lot of support before and after I came to the Netherlands, which make my journey to the Netherlands a smooth process. I also want to thank you for giving me guidance on my visa extension.

I also want to thank the technicians that help me during my lab work in DASML. Thank you to Gertjian, Berthil, and Dave to help me set up the four-point bending test setup and program the fatigue machine. Thank you to Victor and Fred for helping overcome the challenges when embedding the very fragile fiber within the capillary. Thank you Durga, Roy for teaching me specimen embedding and how to use laser microscopy. Thank you to all technicians in the DEMO for machining my specimens.

Living abroad comes with its own set of unique challenges, especially during the difficult Covid time. I am lucky enough to have some friends here in the Netherlands. I want to thank Pap who is very nice and humorous, and the talk with you during lunchtime makes me happy. Thank you Romina who give me a lot of help when I first came to the Netherlands. The talk with Jesse makes me know more about the Netherlands and its culture. I also want to thank my Chinese friends who I spend a lot of time with. Thank you to Hongwei, and I enjoyed the time we went to various restaurants and tasted delicious food, and had many interesting talks with you at your office. Thank you to Lubin and other buddies with whom I cycled along the coast of the Netherlands. Thank you to Xiang, Nan, Xi, Yuqian, Xiaodong, and Shichen, and I enjoyed the time when we had dinner together. I also want to thank Fabricio, Neils, Wandong, Tian, Bram, Megan, Nakash, Ozan, Davide, Huub, Eva, Cornelis, Camila, Nikos etc. in the SI&C and AMT groups.

I want to thank my parents and younger brother who gave me a lot of support during PHD. I am especially grateful to my wife Lu Zhang, for your unwavering support and understanding during my PHD. Your love and encouragement have been a constant source of strength for me.

CURRICULUM VITÆ

Yuzhe Xiao was born in June 1993 in Henan province of China. He got his bachelor's degree in Mechanical engineering from Henan University of Technology and Master's degree in Mechanical Engineering from Beihang University. From October, 2017, he started his study for the PHD degree in Structural integrity & composite group, under the supervision of Prof. Rinze Benedictus, Dr. Calvin Rans, Dr. Dimitrios Zarouchas.

LIST OF PUBLICATIONS

1. Yuzhe Xiao, Calvin Rans, Dimitrios Zarouchas, and Rinze Benedictus. *A Comprehensive Study on Measurement Accuracy of Distributed Fiber Optic Sensors Embedded within Capillaries of Solid Structures.* Sensors 23.19 (2023): 8083.
2. Yuzhe Xiao, Calvin Rans, Dimitrios Zarouchas, and Rinze Benedictus. *Measurement accuracy of distributed sensing fibers embedded within capillaries of solid structures.* 12th International Workshop on Structural Health Monitoring: Enabling Intelligent Life-Cycle Health Management for Industry Internet of Things (IIOT), IWSHM 2019. DEStech Publications Inc., 2019.
3. Yuzhe Xiao, Calvin Rans, Dimitrios Zarouchas, and Rinze Benedictus. *Examining a strain exceedance approach to crack detection using a distributed sensing fibre embedded in a capillary.* (Submitted)
4. Yuzhe Xiao, Calvin Rans, Dimitrios Zarouchas, and Rinze Benedictus. *Study on using deep neural network to perform crack detection with embedded fiber optic sensors in selectively manufactured structures.* (Submitted)